Demonstration of Two-Photon Quantum Interference with Two Tin-Vacancy Centers in Diamond

Timo Dolné
Hanson lab

Delft University of Technology

TU Delft QuTech FUJITSU

Demonstration of Two-Photon Quantum Interference with Two Tin-Vacancy Centers in Diamond

by

Timo Dolné

to obtain the degree of Master of Science
at the Delft University of Technology,
to be defended publicly on Thursday December 12, 2024 at 10:00 AM.

Daily supervisor:	Ir. Christopher Waas	
Responsible supervisor:	Prof. dr. ir. Ronald Hanson	
Project duration:	March 1, 2024 – December 2, 2024	
Thesis committee:	Prof. dr. ir. R. Hanson	TU Delft
	Dr. ir. M. Veldhorst	TU Delft
	Dr. M. F. Rimbach-Russ	TU Delft
	Ir. C. Waas	TU Delft

TU Delft

Acknowledgments

Looking back on the 9 months that I worked on this thesis, I realize that I owe much of the good memories and experiences to a lot of great people I met along the way! Firstly, I would really like to thank my daily supervisor **Christoper**. I hope it is no secret that I consider myself extremely lucky that I got to work together with you! Your German humor, great sense of physics and extremely pleasant way of collaborating has made me like it so much in the lab that I have decided to stay 4 more years. I will never forget the moments of joy in the lab, from disentangling meters of fiber to measuring the first TPQI dip and all the amazing moments in between! I really want to thank you for giving me the freedom and trust to get such an amazing experience out of this project. I am looking forward to more fun discussions, ice-cream walks and dinners when I come back and wish you the best of luck for the final stage of your journey to become a doctor!

Next, I want to thank my supervisor **Ronald** for his invaluable contribution to my thesis. I must say that I thoroughly enjoyed the close contact that I could have with you and it keeps amazing me how you are able to always make time when somebody needs you. In hindsight, I especially enjoyed the occasions on which you would walk into the command center unexpectedly, ready to discuss measurement results that I had analyzed for hours, but which you could pin-point within seconds. I am looking forward to becoming a PhD student under your supervision!

I also owe a special thank you to someone who has become my second supervisor along the way: **Hans**. I don't think I've ever met anyone quite like you and I don't think I ever will again. Thanks to you, I not only learned a lot of physics in these 9 months, but gained some life lessons too. Rest assured, you have successfully carried over your beliefs about *See one, do one, teach one*, certain Python libraries and pizza recipes to a new generation of PhD students! I really enjoyed collaborating with you and am sure that the future has much more exciting research in store for you! And finally, I also want to give a special thanks to the most recent addition of the lab: **Alexander**. I really enjoyed the little time we already had together in the lab and am looking forward to getting a lot more of it once I come back!

I should also emphasize that there were a lot of people outside of my direct collaborators in the lab that made my thesis a really pleasant time. First of all, I owe a big thank you to the entirety of the Hanson lab: **Julius, Julia, Mariagrazia, Yanick, Daniel, Stijn, Tim, Niv, Christian, Leonardo, Nina, Arian, Kian and Matteo**. From Friday evenings in TPKV to Monday mornings in the green room or Wednesday afternoons on a soccer field, I have thoroughly enjoyed your company and the fun conversations. I am genuinely looking forward to working together with many of you when I come back. I also want to thank **Pepijn, Constantijn, Cees, Joan, Tobi, Hector, Alexandra, Sugeiva & Diego** who have all finished their thesis before me and have shown me the comradery of our shared office. I also want to thank my fellow students who were with me during the final part of the journey and are still working on their thesis: **Charlotte, Sara, Miguel, Alexandre** (whom I owe a special thanks for the cover art)**, Fransisco, Valentino, Elsa, Rana, Naoual, Keyuan, Zizheng, Christiaan and Cas**. I wish you all the best of luck in finishing your own projects!

I would also like to thank a special group of people, without whom this journey would not have been possible: My friends and family. My parents **Michel** and **Sylvia** and my brother **Joep**, thank you for supporting me and listening to me yapping about quantum physics and complaining about experimental challenges. Also a special thank you to my great friend **Bram**, on whom I can always rely in my personal life. And of course my roommates **Rachel**, **Elize** and **Eric** who provided me with good food and company at home!

En als allerlaatste: Een extra speciaal bedankje voor mijn lieve oma **Marloes**. Ik ben super dankbaar voor alle kaasstengels, vergaderingen, pannenkoeken en spelletjesmiddagen waar we samen van genoten hebben en zal deze nooit vergeten!

Abstract

The realization of large-scale Quantum Networks has the potential to enable applications such as distributed and blind quantum computing. In turn, these concepts can drive innovation in many high-impact areas of society such as data encryption, pharmaceutical research and energy-grid optimization. The main technological challenge in the realization of such networks lies in the development of their fundamental building blocks: the Quantum Nodes. Quantum Nodes need to be coherent quantum systems that can (i) generate remote entanglement through photons and (ii) store quantum information on nearby quantum memories. Historically, the Nitrogen-Vacancy center in diamond has been regarded as the most promising early-stage candidate system for the realization of small-scale quantum networks. The large-scale deployment of a Quantum internet with Nitrogen-Vacancy center is currently however unfeasible due to the fundamentally inefficient photonic interface of the Nitrogen-Vacancy center and its incompatibility with integrated photonics.

This study focuses on an emergent quantum system that has the potential to improve on the Nitrogen-Vacancy center in terms of both these fundamental limits: the Tin-Vacancy center. The Tin-Vacancy center consists of a single tin atom at an interstitial position between two missing carbon atoms in the diamond lattice. This configuration leads to a spin-1/2 system with optically addressable local energy states within the diamond bandgap. In state-of-the-art experiments, capabilities such as spin control, optical coherence and single-photon generation have been demonstrated in an isolated fashion. The main goal of this work is to (i) show the integration of all these capabilities for two tin-vacancy centers simultaneously in a single setup and (ii) demonstrate the first reported indistinguishability of photons generated by two distinct tin-vacancy centers. The realization of these goals marks a significant step towards entanglement generation with tin-vacancy centers, which is an essential first hurdle for realizing demonstrating its use-case as a Quantum Node.

One capability that is required for entanglement generation is coherent control of the spin state of a tin-vacancy center. This capability was demonstrated for two emitters in two different strain regimes. The influence of strain on the efficiency of microwave spin control was measured through the π-pulse durations of $(0.378 \pm 0.002)\,\mu s$ and $(0.68 \pm 0.01)\,\mu s$ for the emitters with higher- and lower strain respectively. Crucially for entanglement generation, the π-pulse fidelity of 0.980 ± 0.002 for the higher strain emitter vastly outperforms the 0.871 ± 0.006 fidelity of the lower strain emitter. The lower strain emitter did however show a higher decoherence time of $T_2 = (316 \pm 3)\,\mu s$ compared to the higher strain emitter's decoherence time of $T_2 = (47 \pm 2)\,\mu s$. Both these timescales suffice for entanglement generation and can be extended through dynamical decoupling.

Another key ingredient for entanglement protocols is the generation of single photons through coherent optical π-pulses. In this work, a 1.5ns optical π-pulse was calibrated and demonstrated to produce coherent single photon through a measurement of correlations in a Hanbury-Brown-Twiss interferometer. The measured correlations showed a normalized autocorrelation of $g^{(2)}(0) = 0.06 \pm 0.03$, which is sufficiently low to prove the single-photon nature of the detection events.

Finally, the setup was used to measure detection correlations in an experiment involving simultaneous excitation of two tin-vacancy centers, where the collected coherent single photons of both tin-vacancy centers are directed to a Hanbury-Brown-Twiss interferometer. The measured correlations of the detection events reveal a dip in the number of coincidences with a visibility of $V = 0.55 \pm 0.05$. Correcting this value for known noise sources from the measured correlations of the single photons from both emitters leads to an indistinguishability of $\eta = 0.68 \pm 0.07$. This measurement is the first experimental observation of indistinguishability between photons generated from distinct tin-vacancy centers. The remaining distinguishability is shown to largely originate from spectral diffusion, which is mitigated through time filtering to get a maximum visibility of $V = 0.87 \pm 0.08$. Such a visibility poses a limit on the maximum achievable entanglement fidelity of $F = 0.94 \pm 0.04$, which is far above the required fidelity of 0.5 for demonstrating non-classical behavior. It is thus concluded that the results in this thesis provide evidence for the potential to generate entanglement between two tin-vacancy centers with the current setup configuration. Next steps to realize this potential involve the addition of a second optical pulse source, improvement in fiber-waveguide coupling and reduction of the required magnetic field for frequency tuning.

Contents

1

Quantum Networks with color centers in diamond

1.1. The Quantum Revolution

The foundations of many critical processes in today's society rely on the manipulations of zeros and ones by classical computers. The first digital computers in the 1940s were room-sized machines that required manually supplied "punching cards" to execute simple algorithms. The computer saw a burst of technological revolutions over the following decades, ultimately leading to highly optimized nano-scale chips in pocket-size devices [1]. The rate of innovation in the field of classical computers is however stagnating [2] and is even hypothesized to approach its fundamental limits [3]. Since the demand for computational power is only increasing in today's society [4], a fundamentally different platform is needed to meet the requirements. One candidate for such a revolutionary new computational platform is the Quantum Computer.

Quantum Computers are based on the highly counterintuitive laws of physics at the smallest of scales. Classical computers achieve computation with "bits", which can either represent a "0" or a "1" depending on a physical voltage within an electrical circuit. On the contrary, Quantum Computers consist of "quantum bits" or "qubits", which can be both "0" and "1" at the same time depending on their quantum state. More precisely, a qubit can be in such a state that a measurement of the quantum state always yields "0" or "1", but randomly with some probabilities. This principle of *superposition* is a crucial concept that fundamentally distinguishes Quantum Computers from their classical counterparts.

The second fundamental difference between bits and qubits only reveals itself when a system with more than one qubit is considered. The laws of Quantum Mechanics predict that two qubits can be brought into such a state that their systems are so interdependent on one another that "*one cannot really speak of the state of either particle separately*" [5]. This shared property between the two subsystems is called *entanglement* and is often summarized by the fact that a measurement of one of the qubits has an immediate (non-local) effect on the state of the other system [6]. The extent of such correlations enables logical operations that can not be replicated by classical bits.

Although the concepts of superposition and entanglement might seem like isolated phenomena in theoretical physics, they can actually be leveraged for a wide range of applications. Innovation in areas such as pharmaceutical science [7, 8], material science [9] and optimization [10] can benefit from algorithms that leverage these quantum mechanical concepts to achieve exponential speedups over classical algorithms. Additionally, the search for an application for emerging technologies in general is often most successful after those technologies have matured. Nevertheless, there is one particular field of applications with exciting future prospects that is relevant for motivating the experiments of this work: Quantum Networks.

Figure 1.1: Artistic representation of the long-term vision of a Quantum Internet consisting of Quantum Nodes, connected through Quantum Channels through which entanglement can be generated between nodes. Acquired from [15].

Just like the way in which classical computers are interconnected in a classical network (called the *Internet*), the vision for quantum computers is to also connect them with a Quantum Network (referred to as the *Quantum Internet*) [11]. Connections between Quantum Computers through Quantum Channels could enable a wide range of applications ranging from secure communication [12] to distributed quantum computation [13] and satellite-based quantum information transfer [14]. The vision for a Quantum Internet is illustrated in Figure 1.1, which shows a set of Quantum Nodes, physically connected by Quantum Channels, through which their mutual entanglement is generated.

1.2. What is a Quantum Node?

With a vision of the desired functionality of a Quantum Node, it becomes more clear what physical components such a system needs to be composed of. Firstly, quantum nodes need to be composed of a quantum system that is capable of remotely generating entanglement with other such systems. The envisioned way of achieving remote entanglement between two distant *stationary qubits* is by first creating entanglement between the stationary qubit and a *flying qubit*. Concretely, this means that a Quantum Node has to consist of stationary ("communication") qubits that are capable of generating flying qubits that are entangled with their own state. In order to then realize entanglement between the distant stationary qubits, these flying qubits need to be transported between them and measured. The transportation of flying qubits requires a Quantum Channel that is coupled to the Quantum Node. In many realizations of such systems, the communication qubit has a very short-lived memory, that would not be able to preserve the Quantum Information on the timescales of relevant algorithms. To combat this, it is important that the communication qubit is accompanied by several memory qubits, to which the Quantum Information can be relayed and thereby stored.

The main objective in the current field of research is to find suitable physical systems that can meet these requirements. The landscape of candidate systems for stationary qubits is very wide, but there seems to only be a single candidate for the flying qubit: Photons. Photons are the fundamental units of light, which can be leveraged to encode qubits in several degrees of freedom, each with its advantages and disadvantages. The advantage of using photons as flying qubits for the Quantum Internet is two-sided. Firstly, photons have very weak interactions with the environment, which means that they can preserve the quality of encoded quantum information for sufficiently long timescales [16]. Secondly, the current infrastructure of the classical internet is already based on conveying packets of light, meaning that decades of knowledge and innovation on this infrastructure can directly be leveraged [17].

With the definition of flying qubits as photons, it is to investigate which quantum systems can create entanglement between themselves and these photons. This significantly narrows down the range of quantum systems that can be considered for this specific application. The most prominent systems in state-of-the-art literature can be summarized into categories:

1. **Arrays of single atoms or ions**, frozen in position by a high-precision laser beam. These atoms have a natural way of generating photons that are entangled with their own quantum states [18] and the number of atoms can already be scaled to several tens [19, 20]. Scaling orders of magnitude above the current state-of-the-art is currently seen as the biggest challenge as the field is working towards integration into nanophotonics [21]. Moreover, the lack of a natural memory register poses a fundamental limit on the applications that can be realized on a Quantum Network consisting of these systems. The platforms in this category have recently been used for demonstrations of remote entanglement generation [22–24]

2. **Superconducting electrical circuits**, that can be controlled as qubits with all-electronic techniques. These superconducting qubits currently have a big advantage in terms of scaling, as systems with 400 qubits have been demonstrated [25]. The qubit itself is however not inherently compatible with the creation of optical photons. Conversion between this platform and optical photons is an active area of research, which has thus far not been able to demonstrate remote entanglement generation. Moreover, the technology requires the system to be operated at temperatures of several mK, posing a significant engineering challenge for large-scale deployment.

3. Nanostructures made from semiconductors with fabricated shapes that are designed to trap single electron spins (called **Quantum Dots**). The intrinsic properties of these trapped electrons make them compatible with telecom-band photon entanglement and their long coherence time and scalability from the semiconductor platform make them excellent candidates for Network Nodes [26], as recently demonstrated through experimental realization of remote entanglement [27, 28]. The main limitations of this platform are its instable charge environment, which poses a threat to the maximally achievable entanglement quality [29] and the lack of natural options for memory qubits.

4. **Atomic defects** in large-bandgap solid state materials, which have been the most dominant platform for demonstrations of photon-mediated remote entanglement generation [6, 30–34]. These systems benefit from a stable environment from the isolation in energy due to the bandgap structure of their host material, which can often also be leveraged as a natural source of many memory qubits [35–38]. This abundance of interaction with memory qubits does limit the time in which the communication qubit can stay coherent [39]. Moreover, the efficient collection of the emitted photons from these systems has proven to be a technical challenge, which leads to slow rates of entanglement generation in these systems so far [30, 32].

This work considers a system that falls within the last category. The atomic defect that is studied in this work is an imperfection in a diamond crystal lattice. Diamonds are large-bandgap semiconductors, which means that they are colorless in their pure form. The color of a diamond originates from the presence of imperfections (or defects) in the lattice structure, which cause optical resonances between local energy levels. For this reason, the defects in diamond are also known as *color centers*. These color centers have been widely studied historically [40], which means that a lot was known about them before their use-case as Quantum Nodes was hypothesized. The main initial driving force for the research on the quantum behavior of individual color centers was the evolution of purification techniques for diamond, enabling fabrication of samples with a single type of color center. From a Quantum Network perspective, diamond is an ideal host system for Quantum Nodes. Firstly, it has extremely sturdy mechanical properties, which protect the embedded color centers from mechanically induced noise sources. Secondly, the large bandgap of diamond forms an energetic space in which localized energy states of the single defect can be isolated from the energy levels of the diamond lattice. And lastly, the natural concentration of 1% ^{13}C isotopes can be used as memory qubits due to their intrinsic spin, while the 99% concentrated ^{12}C atoms do not have an interaction with the spin states of the color centers.

1.3. Spin qubits in diamond

Historically, the first type of color center that has been extensively studied in the context of Quantum Networks is the Nitrogen-Vacancy (NV) center. The NV center is a particular impurity in diamond where a Nitrogen atom sits on one of the lattice points in a configuration of two nearest-neighbor missing carbon atoms. So far, the NV center has been the leading candidate for the realization of Quantum Nodes with color centers, as is demonstrated by the first remote entanglement experiment [30], demonstration of a loophole-free non-local Bell test [6], realization of a multi-node network [41], integration with existing commercial fiber infrastructure [42], quality control of the memory register [35, 36] and qubit teleportation [43]. The development of the NV center

as an early-stage candidate for a Quantum Network Node can mostly be attributed to its incredibly flexible and well-tunable properties. There are however two fundamental limits of the NV center, which potentially prohibit its large-scale deployment in a Quantum Internet. Firstly, the inherent properties of the NV center cause it to have a highly inefficient interface for producing useful photons for entanglement generation. Because of this, entanglement generation rates are unreasonably slow for larger-scale applications. Secondly, the sensitivity of the system to local charge fluctuations causes it to be incompatible with integrated photonics, which is thought to be crucial for large-scale deployment.

Because of these reasons, recent developments have shifted to different types of defects in diamond: Group-IV vacancy centers. These types of color centers are theoretically predicted to be able to improve on the NV center, both in terms of the efficiency of their spin-photon interface and their compatibility with nanophotonic integration [44]. For these types of defects, a Group-IV elements (Si, Ge, Sn, Pb) replaces the Nitrogen atom of the NV center and occupies a lattice position between two nearest-neighbor vacancies. The heavier Group-IV elements form a symmetrical configuration, which reduces the sensitivity to charge fluctuations and improves the photon emission efficiency. These enhance properties of Group-IV vacancy centers pave the way towards highly-integrated photonic chips with fast entanglement generation rates as Quantum Network Nodes.

Out of all Group-IV vacancy centers, the silicon-vacancy (SiV) center [33, 45–48] and tin-vacancy (SnV) center [37, 49–58] have been investigated most thoroughly. The silicon-vacancy is the most-developed platform of the two, having demonstrated photon indistinguishability between two defects [45], cavity-based entanglement generation [33], coherent control over memory qubits [48, 59] and long-distance single-click entanglement with Quantum Frequency Conversion [47]. The silicon-vacancy center does however suffer from one fundamental downside. Due to its relatively small ground-state splitting, it requires cryogenic temperatures of ~40 mK, which are much lower than the required temperature of ~1.7 K temperature requirements for the tin-vacancy. This makes their large-scale deployment much more difficult from a technical point of view and motivates research on the tin-vacancy center. State-of-the-art experiments on the tin-vacancy center have shown microwave control of the spin state [49, 52, 56], integration of the defect in nanophotonic waveguides [54, 60, 61], coherent optical transitions [50, 61] and coherent control of a nearby ^{13}C nuclear spin [37]. However, an experimental realization of remote entanglement generation between tin-vacancy centers is still illusive. The goal of this research is to take a significant step towards that goal by (i) demonstrating individual control capabilities that are necessary for such experiments on two independent subsystems with a single setup and (ii) demonstrating photonic indistinguishability between two distinct tin-vacancy centers, which is the key ingredient for remote entanglement generation. Isolated control capabilities with tin-vacancy centers to the level that is required for entanglement generation have been demonstrated in literature, but no attempt has been made yet to combine all of these capabilities into a single setup in which two tin-vacancies can be controlled simultaneously. The achievement of photon indistinguishability between two tin-vacancy centers would thereby be a novelty in the field paving the way towards entanglement generation with integrated nanophotonics.

1.4. Structure of the thesis

This thesis is structured into 8 Chapters, the first of which is this introduction. The thesis will proceed with Chapter 2, which presents the relevant theoretical background that is required to understand the experimental results. Chapter 3 will then give a detailed overview of the experimental setup and will dive into specific experimental capabilities that are used in the following chapters. In Chapter 4, the optical manifold of the tin-vacancy center will be studied in great detail, leading to a complete understanding of the relevant dynamics of all optical transitions. After that, Chapter 5 will demonstrate a key capability of any entanglement generation experiment in the form of coherent spin control. Next, Chapter 6 will demonstrate control over the optical manifold on a single-photon level, which is another necessity for remote entanglement generation. Then, Chapter 7 will present the main experimental results in the form of an experimental demonstration of photon indistinguishability between two distinct tin-vacancy centers. Finally, Chapter 8 will provide a conclusion on the results from this work and an outlook on possible avenues and considerations for future research.

2
Theoretical Background

This chapter will provide the relevant theoretical background for understanding the results presented in Chapters 4-7. More specifically, the chapter will start with a general quantum mechanical description of the tin-vacancy center, which is used in Chapters 4-6 as a base model for interpreting the experimental results. After this, the Two-Photon Quantum Interference effect will be explored, setting the theoretical stage for the experiments in Chapter 7. Finally, the chapter will close with a general description of the double-click entanglement protocol, which is used in Chapters 4-7 as a guideline for estimating required parameters and capabilities to enable an experimental demonstration of entanglement generation.

2.1. The tin-vacancy center

This section explores the quantum mechanical description of the tin-vacancy (SnV) center. The SnV center is a particular impurity in diamond, where a tin atom sits at an interstitial position between two missing carbon atoms (as schematically shown in Figure 2.1c). In a stable state, this configuration has a unit of negative charge and local energy levels that can be described as wavefunctions of a single hole [46, 62]. This section will explore the eigenstates of this system, as derived from the combined Hamiltonians of the tin-vacancy configuration and the surrounding diamond lattice. To this end, the section will start by describing the diamond host material, after which the level-structure of the localized tin-vacancy eigenstates is studied. This knowledge is then used to study driven perturbations of the Hamiltonian, both in the optical and microwave regime separately.

2.1.1. Diamond as a host material

The tin-vacancy centers in this work are studied as defects in a diamond crystal lattice. Using diamond as a host material for quantum controllable atomic defects has several benefits. Firstly, diamond is a semiconductor with a large bandgap of roughly 5.48 eV [63]. The energy states of the defect within this band gap are therefore largely isolated from interactions with the conduction and valance band of the host material. Isolation from these interactions is essential for preserving the coherence of quantum states defined by the occupation of the localized energy levels of the tin-vacancy center. Secondly, the extremely stable mechanical properties of diamond make it an excellent material for hosting defects in minimal strain environments. Materials with less stable mechanical properties are more susceptible to strain fluctuations, which generally hurt optical properties of the defects. Finally, the natural abundance of ^{13}C (spin $1/2$) isotopes in diamond is around 1% [64]. The remaining 99% of carbon atoms are of the ^{12}C isotope, whose nucleus is a spin 0 system. The presence of the nuclear spin-$1/2$ systems in a low concentration can be leveraged as a natural source of long-lived quantum memories.

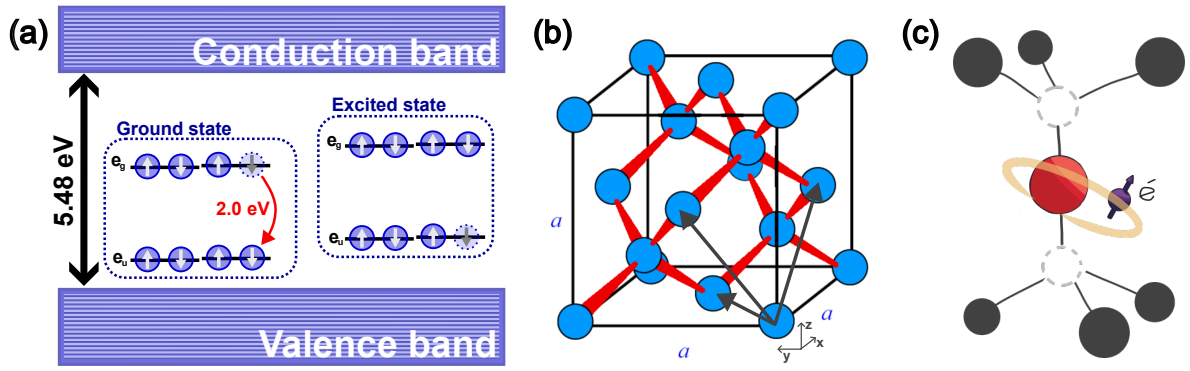

Figure 2.1: Overview of the characteristics of the tin-vacancy center in the diamond lattice structure. (a) A schematic of the diamond semiconductor band structure, combined with the localized energy states of the SnV^- configuration. The two level diagrams represent the ground- and excited state of the SnV^- charge state, which can be described as the occupation of a hole state in one of the energy levels. Inspired by figures in [58, 62]. (b) The diamond unit cell, depicted with blue balls representing the carbon atoms and red interconnects representing the sp^3 covalent bonds between them. The three gray arrows represent the lattice vectors of the conventional unit cell. Adapted from [68] (c) Schematic representation of the configuration of a tin-vacancy center in diamond, as a single tin atom (red) that resides at an interstitial position between two missing carbon atoms.

To properly define the energy levels of the tin-vacancy center, it is crucial to understand the energy structure of the diamond lattice. Figure 2.1b shows the unit cell of the lattice structure. The lattice constant of a pure diamond crystal is known to be $a = 0.3567$ nm [65]. The large band gap of diamond makes it colorless in the optical regime. The introduction of local imperfections in the diamond lattice has historically been found to lead to the emergence of localized energy states within the diamond band gap. These localized energy levels introduce energy transitions in the optical domain, giving the diamond a specific color depending on the type of imperfections it contains. Because of this, the impurities in diamond are also known as *color centers*. Many different color center species have been discovered, each with different and interesting properties [40].

The absolute energy levels of color centers can be studied through Density Functional Theory (DFT) [66]. DFT calculations for the tin-vacancy configuration reveal localized energy states within the diamond band gap [67]. Throughout this thesis, we investigate the negative charge state of the tin-vacancy center (labeled as SnV), which can be described as a 4-level system with 2-fold degeneracy in the spin state (assuming zero magnetic field). In the SnV^- ground state, all lower energy levels and all-but-one of the higher energy levels are occupied by an electron (see Figure 2.1a). Instead of describing the system with the occupation of the electronic levels, it is more intuitive to describe the states as a single hole occupation in the hole ground state (e_g). The energy difference between the ground and excited state of the hole are separated by a 2.0 eV transition [67]. Both ground- and excited states consist of an upper- and lower branch, which are non-degenerate even at zero magnetic field.

A crucial consequence of the symmetric spatial configuration of the tin-vacancy center (Figure 2.1) is that its orbital eigenstates exhibit a D_{3d}-symmetry [67]. This symmetry leads to a first-order insensitivity of the eigenenergies to the local electric field. Effectively, this means that the transition frequencies of a tin-vacancy center are much less sensitive to fluctuations in the local charge environment than for example the Nitrogen-Vacancy center. This characteristic enables the integration of tin-vacancy centers in nanophotonic structures, where the defects are relatively close to the fluctuating charge environment of surface charge traps.

Lastly, the large bandgap of diamond allows the localized tin-vacancy energy levels to often be regarded as an isolated 4-level system. It should however be noted that the charge dynamics between the tin-vacancy center and the diamond host become crucial when describing describing dark decay channels in Section 2.1.3 and charge dynamics of repumping in Section 3.4.

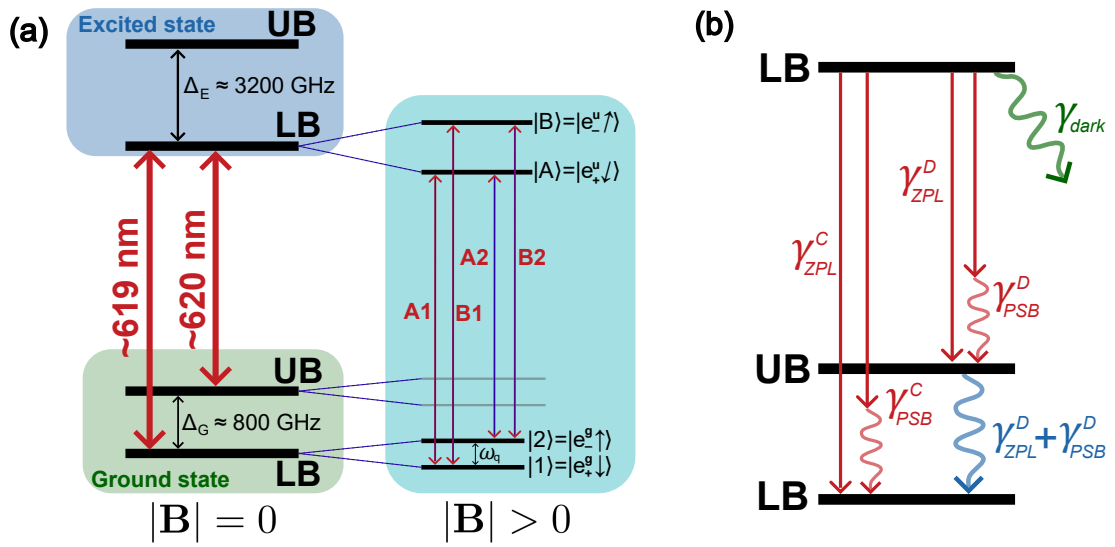

Figure 2.2: Overview of the electronic level structure of the tin-vacancy center. (a) The eigenenergies and eigenstates of the Hamiltonian, both with zero and non-zero magnetic field. The relevant transitions are highlighted by red arrows. (b) Schematic overview of the decay channels from the lower branch of the excited state. The relative magnitudes of these decay channels are captured in the combination of the Quantum Efficiency (QE), Debye-Weller (DW) factor and the Branching Ratio (BR).

2.1.2. Electronic level structure & Hamiltonian

The schematic in Figure 2.1a depicts the ground- and excited state of the tin-vacancy center as occupations of 8 eigenstates. This section will focus on deriving the Hamiltonian describing those localized energy levels. The derivation of the system Hamiltonian will be done without incorporating the diamond bandgap energy levels. Instead, the influence of the valance and conduction band will be described qualitatively for processes where this is necessary.

To lay the groundwork, it is important to know the different physical processes that affect the unperturbed Hamiltonian of the SnV system. For defects in solid-state materials, the quantitative descriptions of the most significant components are quite well-known. Following convention in literature [49, 50, 69], the Hamiltonian is separated into two distinct Hilbert spaces for the ground (g) and excited (u) states. For each of them, the contributions to the total Hamiltonian can be written as

$$\begin{aligned} \hat{H}^{g,u} &= \hat{H}^{g,u}_0 + \hat{H}^{g,u}_{\text{fine}} \\ &= \hat{H}^{g,u}_0 + \hat{H}^{g,u}_{SO} + \hat{H}^{g,u}_{\text{strain}} + \hat{H}^{g,u}_Z + \hat{H}^{g,u}_L. \end{aligned} \tag{2.1}$$

Equation 2.1 denotes the total Hamiltonian as a combination of the atomic Hamiltonian $\hat{H}^{g,u}_0$ and a (hyper)fine correction Hamiltonian $\hat{H}^{g,u}_{\text{fine}}$. The atomic Hamiltonian $\hat{H}^{g,u}_0$ can be derived from group theory [46] and has a diagonalization with an eigenbasis represented by: $\{|e^{g,u}_x\uparrow\rangle, |e^{g,u}_x\downarrow\rangle, |e^{g,u}_y\uparrow\rangle, |e^{g,u}_y\downarrow\rangle\}$. The eigenenergies of $H^{g,u}_0$ reveal that these states are four-fold degenerate, both in the ground- and excited state [46]. The degeneracy of the eigenstates gets lifted as we consider the (hyper)fine interaction terms in $\hat{H}^{g,u}_{\text{fine}}$. These terms are explicitly shown in Equation 2.1 and correspond to: The spin-orbit coupling $\hat{H}^{g,u}_{SO}$, the effect of strain $\hat{H}^{g,u}_{\text{strain}}$, the spin Zeeman effect $\hat{H}^{g,u}_Z$ and the orbital Zeeman effect $\hat{H}^{g,u}_L$. The last two components are the result of an external magnetic field. As a first step, the combined contributions of $\hat{H}^{g,u}_{SO}$ and $\hat{H}^{g,u}_{\text{strain}}$ will be analyzed to obtain a diagonalization of the system Hamiltonian at zero magnetic field. After this, the effect of an external magnetic field will be described by incorporating $\hat{H}^{g,u}_Z$ and $\hat{H}^{g,u}_L$.

Spin-orbit coupling

The spin-orbit effect describes the coupling between the orbital angular momentum and spin state of an electron (or hole) in an atomic system. Intuitively, the orbital angular momentum corresponds to a certain dynamic charge displacement, which creates a magnetic field. The spin-orbit interaction arises from the effect of this magnetic field on the spin eigenstates. This influence effectively creates an interaction between the orbital angular momentum and intrinsic spin, which can be quantified by an interaction Hamiltonian of the form

$$\hat{H}_{SO}^{g,u} = -\frac{\hbar\lambda_{g,u}}{2}\hat{\mathbf{L}}^{g,u}\cdot\hat{\mathbf{S}}^{g,u}. \tag{2.2}$$

The $\hat{\mathbf{L}}$ and $\hat{\mathbf{S}}$ operators in Equation 2.2 represent the orbital and spin operators respectively. Expressing these operators in the eigenbasis of $\hat{H}_0^{g,u}$ transforms Equation 2.2 into

$$\hat{H}_{SO}^{g,u} = -\frac{\hbar\lambda_{g,u}}{2}\begin{bmatrix}0 & i\\ -i & 0\end{bmatrix}\otimes\begin{bmatrix}1 & 0\\ 0 & -1\end{bmatrix}. \tag{2.3}$$

The orbital operator in the chosen basis only has contributions in the z-direction [46], which is why $\hat{H}_{SO}^{g,u}$ is the matrix product of the $\hat{L_z}^{g,u}$ and $\hat{S_z}^{g,u}$ operators. Diagonalizing the spin-orbit Hamiltonian reveals the set of eigenstates and eigenenergies, which can be written in terms of the eigenstates of $\hat{H}_{SO}^{g,u}$ as

$$\begin{aligned}
\hat{H}_{SO}^{g,u}|\Psi\rangle = +\frac{\lambda}{2}|\Psi\rangle \Rightarrow \begin{cases} |\Psi\rangle = \frac{-1}{\sqrt{2}}\left(|e_x^{g,u}\uparrow\rangle + i\,|e_y^{g,u}\uparrow\rangle\right) \equiv |e_+^{g,u}\uparrow\rangle \\ |\Psi\rangle = \frac{1}{\sqrt{2}}\left(|e_x^{g,u}\downarrow\rangle - i\,|e_y^{g,u}\downarrow\rangle\right) \equiv |e_-^{g,u}\downarrow\rangle \end{cases} \\
\hat{H}_{SO}^{g,u}|\Psi\rangle = -\frac{\lambda}{2}|\Psi\rangle \Rightarrow \begin{cases} |\Psi\rangle = \frac{-1}{\sqrt{2}}\left(|e_x^{g,u}\downarrow\rangle + i\,|e_y^{g,u}\downarrow\rangle\right) \equiv |e_+^{g,u}\downarrow\rangle \\ |\Psi\rangle = \frac{1}{\sqrt{2}}\left(|e_x^{g,u}\uparrow\rangle - i\,|e_y^{g,u}\uparrow\rangle\right) \equiv |e_-^{g,u}\uparrow\rangle\,. \end{cases}
\end{aligned} \tag{2.4}$$

From the diagonalization it becomes clear that the spin-orbit coupling causes the ground- and excited state to both split into two twofold degenerate states, which are split by $\lambda^{g,u}$.

Strain

The lattice strain is a measure for the mechanically-induced distribution of lattice constants within an otherwise uniform lattice. A smeared distribution of lattice constants can originate from local lattice imperfections and deformations or from externally applied forces. Effectively, non-uniformity in the lattice around a tin-vacancy center causes the symmetry of the environment to be broken, which has consequences for the orbital wavefunctions. More precisely, the effect of symmetry breaking to atomic Hamiltonians has been studied extensively for spontaneous symmetry breaking processes in the form of the Jahn-Teller effect [70]. The effect of strain-induced symmetry breaking can be described in the same way as the Jahn-Teller effect with a purely orbital correction Hamiltonian as [46, 50]

$$\hat{H}_{\text{strain}}^{g,u} = \hbar\begin{bmatrix}\Upsilon_x^{g,u} & \Upsilon_y^{g,u}\\ \Upsilon_y^{g,u} & -\Upsilon_x^{g,u}\end{bmatrix}\otimes\hat{I}^{g,u}. \tag{2.5}$$

It should be noted that there is no way of distinguishing between the contributions of spontaneous symmetry breaking (the Jahn-Teller effect) and the strain-induced static asymmetry. In this work, both will be attributed to the effect of lattice strain. Combining Equations 2.5 and 2.3 gives the total (hyper)fine interaction Hamiltonian in the absence of an external magnetic field. Diagonalizing this Hamiltonian leads to slight corrections for the set of spin-orbit eigenstates in Equation 2.4, whose eigenenergies are schematically depicted on the left side of Figure 2.2a. The splitting between the two-fold degenerate eigenenergies in both the ground and excited state can analytically be calculated as

$$\Delta^{g,u} = \sqrt{(\lambda^{g,u})^2 + 4(\Upsilon^{g,u})^2}, \tag{2.6}$$

where $\Upsilon^{g,u} = \sqrt{(\Upsilon_x^{g,u})^2 + (\Upsilon_y^{g,u})^2}$ is referred to as the *strain magnitude*. It is often one or two orders of magnitude lower than the spin-orbit coupling strength $\lambda^{g,u}$, but still has a crucial role in the dynamics of oscillating magnetic field perturbations (as investigated in Section 2.1.4). The Hamiltonian of the combined effect of spin-orbit coupling and strain leads to two spin-degenerate states in both the ground- and excited state, which will be referred to as the Lower Branch (LB) and Upper Branch (UB).

Orbital and Spin Zeeman effects

The spin-degeneracy in the combined effects of spin-orbit coupling and strain can be lifted by the introduction of an external magnetic field. The effect of an external magnetic field has the most prominent influence on the spin eigenfunctions, but also influences the orbital components of the eigenfunctions. These effects will be analyzed separately. The spin Zeeman effect describes the coupling between the spin operator and an external magnetic field through

$$\hat{H}_Z^{g,u} = \frac{\hbar\gamma_S}{2}\hat{I}^{g,u} \otimes \hat{\mathbf{S}}^{g,u} \cdot \boldsymbol{B}, \tag{2.7}$$

where $\boldsymbol{B} = (B_x, B_y, B_z)$ is defined in a Cartesian coordinate system with the z-axis aligned to the symmetry axis of the tin-vacancy center. The interaction strength γ_S in Equation 2.7 is the electron gyromagnetic ratio $\left(\gamma_S = 28.025\,\frac{\mathrm{GHz}}{\mathrm{T}}\ [71]\right)$, which is responsible for lifting the degeneracy of the spin states. There is an additional effect of the external magnetic field on the orbital components of the eigenfunctions. This effect can be calculated through the orbital Zeeman interaction Hamiltonian

$$\hat{H}_L^{g,u} = \frac{\hbar\gamma_L}{2}B_z\hat{L}_z \otimes \hat{I}, \tag{2.8}$$

where γ_L is the strength of the orbital Zeeman splitting. Combining these Zeeman contributions and diagonalizing the Hamiltonian is an analytically extensive exercise, which will not be done explicitly here (see [46] for more detailed derivations). Instead, the results from this diagonalization can qualitatively be described and are schematically shown in Figure 2.2a. Effectively, the degeneracy in the levels is split linearly with the magnetic field strength. The splitting rate is different for the ground- and excited state, leading to four spectrally separated optical transitions between the Lower Branch of the Excited State and the Lower Branch of the ground state (conveniently defined as A1, A2, B1 and B2 in Figure 2.2a).

2.1.3. Optical transitions and driving dynamics

The unperturbed Hamiltonian as presented in the previous section features four non-degenerate transitions between each combination of Branches of the ground- and excited state at non-zero external magnetic fields. Due to the extremely short lifetime of the upper branch of the excited state, any population in the upper branch relaxes to the lower branch of the excited state much faster than the radiative lifetime [46, 72]. This section will therefore focus on a description of the optical transitions between the ground states and the lower branch of the excited state. Firstly, an analysis of the different decay channels from the lower branch of the excited state will be done to derive the percentage of photons that get emitted into a useful decay channel for entanglement generation. After this, the dynamics of optical excitation from the ground state to the excited state will first be explored in a semi-classical description. This semi-classical treatment will then be translated qualitatively to the quantum mechanical description of the tin-vacancy center for a few relevant parameters.

Decay channels of the excited state

It is possible to derive all allowed decay channels from the lower branch of the excited state through Fermi's golden rule [73]. For the level-structure of the tin-vacancy center, the infinitely large set of possible decay channels can get categorized into five different types of decays, as is done schematically in Figure 2.2b. Firstly, there are two decay channels into the upper branch of the ground state (the D-transitions) and two decay channels into the lower branch of the ground state (the C-transitions). Both the C- and D-transition can have two types of relaxation events. The most intuitive relaxation event is the emission of a single photon with the exact wavelength corresponding to the energy difference between the two transitions. This type of single-photon emission event is categorized as the Zero-Phonon Line (ZPL). Next to relaxation through the emission of a single photon, it is also possible to have relaxation events consisting of the emission of a single photon and a single phonon. Such decay events are categorized as the Phonon Sideband (PSB). The existence of such decay events is enabled by an overlap between the vibronic ground state in the SnV excited state and the vibronic excited states in both branches of the SnV ground state [46, 74]. Effectively, this overlap can be summarized by the ratio of relaxation events in the ZPL compared to the PSB. This ratio is called the *Debye-Waller factor* (DW) and is predicted from experiments for the tin-vacancy center to be given by [75]

$$DW = \frac{\gamma_{ZPL}^C + \gamma_{ZPL}^D}{\gamma_{ZPL}^C + \gamma_{ZPL}^D + \gamma_{PSB}^C + \gamma_{PSB}^D} \approx 0.57. \tag{2.9}$$

It should be noted that photons emitted in the ZPL of the D-transition can not be used for entanglement protocols. The reason for this is that the relaxation events in the ZPL of the D-transition features a two-step process, starting with the emission of a photon on resonance with the D-transition, followed by the emission of a phonon on resonance with the ground state splitting (see Figure 2.2b) [72]. The quantum state of this phonon is immediately lost in the vibrational mode of the diamond lattice, thereby collapsing the entangled state between the emitter, photon and phonon into a mixed state and thus crucially losing the electron-photon entanglement. Given that the D-transition can not be used for entanglement purposes, it is useful to quantify the ratio of decay events in the ZPL of the D-transition compared to those of the C-transition. This ratio is called the *Branching Ratio* (BR) and is estimated for the tin-vacancy to be

$$BR = \frac{\gamma^C_{ZPL}}{\gamma^C_{ZPL} + \gamma^D_{ZPL}} \approx 0.8 \tag{2.10}$$

from recent experiments [53, 76]. Lastly, there is one decay channel in Figure 2.2b that has not yet been accounted for: γ_{dark}. The origin of this decay channel lies in the absolute energy of the tin-vacancy eigenenergies with respect to the diamond bandgap. More specifically, the energy gap between the lowest energy levels and the valence band can be bridged by the 2.0 eV excitation photons that are used to bridge the energy gap of the C-transition. In this way, the hole in the excited state can be transferred to the valence band instead of relaxing back into the ground state. The absorption of the tin-vacancy hole in the valance band effectively creates a SnV^{2-} configuration, which is well-known to not be optically active [62]. The *Quantum Efficiency* (QE) describes the ratio of the rates of these decay events into the "dark" SnV^{2-} state compared to all other decay events that lead to emission of a photon. For the tin-vacancy center, this factor is found from initial experiments [51, 53] to be

$$QE = \frac{\gamma^C_{PSB} + \gamma^C_{ZPL} + \gamma^D_{PSB} + \gamma^D_{ZPL}}{\gamma_{dark} + \gamma^C_{PSB} + \gamma^C_{ZPL} + \gamma^D_{PSB} + \gamma^D_{ZPL}} \approx 0.8. \tag{2.11}$$

The combination of these three factors determines the probability of a decay event in the ZPL of the C-transition upon excitation to the lower branch of the excited state. Combining them leads a probability of ~ 36% for the tin-vacancy center. This relatively high percentage is one of the main advantages of the tin-vacancy center over both the Nitrogen-Vacancy (NV) center (~ 3%) [77] and other Group-IV color centers (10-25%) [46, 78, 79]. A high rate of emission into "entanglement-compatible" decay channels is crucial for the rate at which entanglement generation can be achieved.

Dynamics of optical excitation

So far, the analysis has focused on the physics of relaxation events starting from the excited state, but has disregarded the way in which the system can get manipulated into this excited state. For the tin-vacancy center, driving between the ground- and excited state can be achieved through a perturbation introduced by an oscillating electric field. The interaction between an external electric field $\hat{\mathbf{E}}$ and the dipole moment $\hat{\mathbf{p}}$ of the orbital state of the tin-vacancy center leads to an interaction Hamiltonian

$$\hat{H}'_{opt} = -\hat{\mathbf{p}} \cdot \hat{\mathbf{E}} = -q\hat{\mathbf{r}} \cdot \hat{\mathbf{E}}, \tag{2.12}$$

where the definition $\hat{\mathbf{p}} \equiv q\hat{\mathbf{r}}$ is used to rewrite the equation in terms of the positional operator $\hat{\mathbf{r}}$ and charge q. Crucially, the dipole operator in Equation 2.12 obeys the following properties:

$$\begin{cases} \langle e_{g,+/-} | \hat{\mathbf{p}} | e_{g,+/-} \rangle = 0 \\ \langle e_{u,+/-} | \hat{\mathbf{p}} | e_{u,+/-} \rangle = 0 \\ \langle e_{g,+/-} | \hat{\mathbf{p}} | e_{u,+/-} \rangle \neq 0, \end{cases} \tag{2.13}$$

which are independent of the spin states (whose notation is therefore omitted). These relations can be derived by a proper treatment of the eigenstates and dipole operator in group theory [46], but can intuitively be understood from the asymmetry of the position operator, which only leads to connections between states with different parity. The wavefunctions of the ground- and excited state have opposing parities, which means that an oscillating electric field on resonance with the transition can lead to population transfer between those states [80]. Given that the transitions of the tin-vacancy center have a wavelength aroud 619 nm, the oscillating electric field can experimentally be realized through coherent electromagnetic waves in the optical regime. Instead of a full quantum mechanical treatment of absorption and radiation of photons in a two-level system

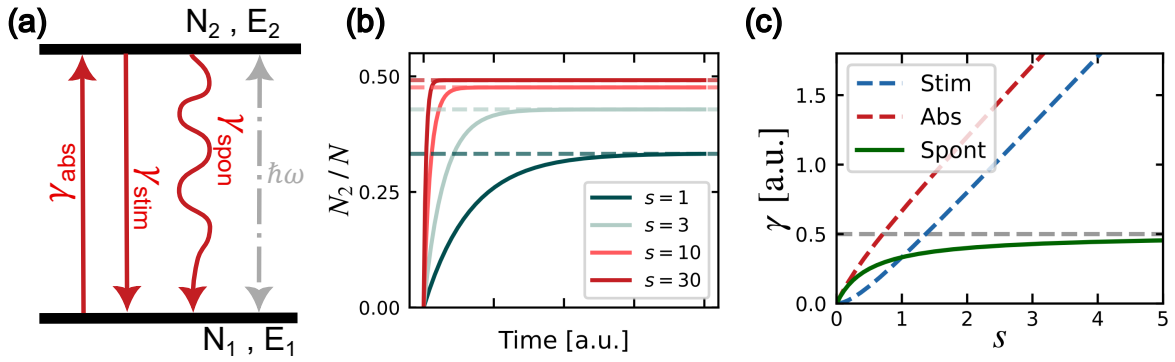

Figure 2.3: Overview of the balance between absorption, stimulated emission and spontaneous emission in a semi-classical description of the optically driven C-transition of a tin-vacancy center. (a) Schematic drawing of the two-level system, indicating the three types of population transfer that are considered: Absorption (γ_{abs}), stimulated emission (γ_{stim}) and spontaneous emission (γ_{spon}). The latter is indicated with a jittering line indicating the creation of a photon during this process. (b) The evolution of the excited state population N_2 over time for four different driving powers (as represented by the saturation parameter). Color-coded dashed lines indicate the steady-state population. (c) The relation between the steady-state transition rates of all three processes in (a) for a range of saturation parameters s. The saturation of the spontaneous emission rate is a crucial observation, which will be used in Section 4.3.

(which can be found in [80]), this work will present a more intuitive description of the absorption and emission processes based on Einstein coefficients [81]. This semi-classical description suffices for predicting the population dynamics under a set of conditions, such as negligible non-radiative decay processes between the ground- and excited state, weak coupling of the states to the radiation field and a smoothly varying energetic density of states of the radiation field [80]. These conditions are satisfied for all experiments in Chapter 4 & 5, where optical excitation is done in a continuous fashion. The approximation breaks down only for experiments involving coherent optical Rabi dynamics, such as in Chapters 6 & 7. For now the focus will be on modeling the experiments where these approximations are valid. In that case, the population transfer in the two-level system can be described by three processes: Absorption, stimulated emission and spontaneous emission.

Instead of a quantum mechanical treatment of a coherent superposition state of a single two-level system, this approach describes average population sizes of the two levels for an ensemble of $N \gg 1$ identical independent two-level systems, with the underlying assumption that each system can only be in one of the two levels. The occupation of the ground state (N_1) and excited state (N_2) then satisfies

$$\frac{N_1}{N} + \frac{N_2}{N} = 1. \tag{2.14}$$

The radiative processes of absorption, stimulated emission and spontaneous emission are schematically shown Figure 2.3a. The main assumption in the Einstein description of the processes is that these three can all be described as rates, defined by the Einstein coefficients. Each Einstein coefficient is again defined as the probability of emission/absorption per unit time. For spontaneous emission, this probability is simply equal to the Einstein coefficient A. For both absorption and stimulated emission, the probabilities are assumed to be proportional to the strength of the driving field $\overline{P(\omega)}$, defined as the radiative energy density at frequency ω. The rates of absorption and emission are then given by $B_{12}\overline{P(\omega)}$ and $B_{21}\overline{P(\omega)}$ respectively. The rate of change in populations of the two states can then be described by a differential equation as

$$\frac{dN_1}{dt} = -\frac{dN_2}{dt} = AN_2 + (B_{21} - B_{12})\overline{P(\omega)}N_1. \tag{2.15}$$

If all systems are in the ground state at time $t = 0$ and the *saturation power* (whose naming convention will become more clear later) is defined as $P_{sat} = \frac{A}{B_{21}}$, then Equation 2.15 can be solved to find the evolution of the excited state population as

$$\frac{N_2(t)}{N} = \frac{\overline{P(\omega)}}{P_{sat} + 2\overline{P(\omega)}}\left[1 - e^{-\left(A+2B\overline{P(\omega)}\right)t}\right]. \tag{2.16}$$

This time-evolution of the excited state occupation is plotted for several values of the *saturation parameter* $s = \frac{\overline{P(\omega)}}{P_{sat}}$ in Figure 2.3b. The saturation parameter is a normalized measure for the driving strength of the radiation

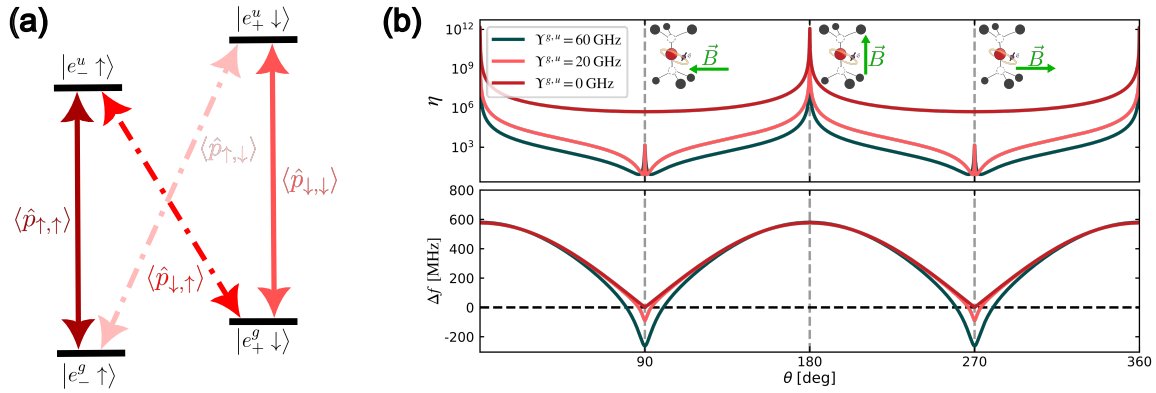

Figure 2.4: Optical driving of the tin-vacancy level-structure in the non-zero external magnetic field regime. (a) Schematic overview of the 4-level system between the lower branches of the ground- and excited state, including their coupling strengths. The arrows between states with an opposing spin direction are dashed to reflect their low interaction term in the perturbation Hamiltonian of an oscillating electric field. (b) The influence of the orientation of a 100 mT external magnetic field on both the cyclicity η (upper panel) and frequency splitting between the spin-conserving transitions Δf (lower panel) for three different strain regimes (colour coded). The dipole orientation of the SnV center is taken as the z-axis and the polar angle θ of the magnetic field is swept for a slice at an azimuthal angle of $\phi = 0$. Vertically dashed gray lines are used to indicate angles where the external magnetic field is exactly perpendicular or parallel to the dipole moment (as indicated by the accompanying schematic drawings). The figure shows how higher strain magnitudes lead to lower cyclicities at all magnetic field orientations. Meanwhile, both the cyclicity and frequency splitting between spin-conserving transitions are maximized for aligned magnetic field orientations.

field. Figure 2.3b reveals the influence of this parameter on two characteristics. Firstly, one can observe that the initial rate of population transfer is highly dependent on the saturation parameter. The characteristic timescale of the population transfer is found to be inversely proportional to the driving power. Secondly, the steady-state population size ($N_2(t \to \infty)$) seems related to the saturation parameter. This relation can be explored analytically by setting the left side of Equation 2.15 to zero. This yields a steady-state excited state population of

$$\frac{N_2}{N} = \frac{\overline{P(\omega)}}{P_{sat} + 2\overline{P(\omega)}}, \tag{2.17}$$

which approaches $N/2$ at infinite driving power. This behavior can also be seen in the saturating population sizes of Figure 2.3b. From a quantum mechanical point of view, this limiting behavior also makes sense. In the Schrödinger picture, population transfer between the two states happens coherently as Rabi oscillations. The frequency of these oscillations is directly proportional to the driving power, implying that as the driving power approaches infinity, the Rabi frequency also diverges to infinity. In that limit, the rate of spontaneous emission is negligible compared to the Rabi rate and the average occupation of the excited state is thus exactly $1/2$. Experimentally however, only photons emitted through spontaneous emission are measured. Figure 2.3c shows the contributions of all three absorption/emission processes to the population sizes in terms of steady-state rates. The steady-state spontaneous emission rate is always equal to the difference between the absorption and stimulated emission rates (as required by Equation 2.14). The shape of the spontaneous emission rate curve saturates after a characteristic power of $s = 1$, which reveals the motivation for the naming convention. Moreover, at this saturation power the rate of spontaneous emission is exactly equal to the rate of stimulated emission, which can be interpreted as the Rabi rate from a proper quantum mechanical description [80]. This property will become crucial in estimations of the collection efficiency in Section 4.3.

Driving the optical manifold of the tin-vacancy center

It should still be noted that the tin-vacancy level structure is not an ensemble of classical two-level systems as assumed in the previous derivation. To translate the semi-classical analysis to a proper description of the tin-vacancy level structure, it can be noted that the Einstein coefficients are directly linked to the quantum mechanical description by

$$B \sim \left|\langle 1|\hat{\mathbf{p}}|2\rangle\right|^2, \tag{2.18}$$

where $|1\rangle$ and $|2\rangle$ are the wavefunctions of the ground- and excited state [80]. Utilizing the same eigenbasis as in Section 2.1.2 at non-zero external magnetic field, each transition can be described in the Einstein picture separately through a translation with Equation 2.18. This principle is schematically drawn for the four C-transitions from the lower branch of the ground state to the lower branch of the excited state in Figure 2.4a. The spin-flipping transitions are marked with dotted lines, which indicate the fact that those matrix elements are much smaller than the spin-conserving matrix elements of the dipole moment [46].

The fact that the off-diagonal (spin-flipping) matrix elements of the dipole operator are non-zero indicates that there is a finite probability of excitation or decay through such a transition. The probability of spin-flipping decay events is captured by the cyclicity η, which is defined as the expectation value of the number of cycles of a spin-conserving transition that can be done before a spin-flipping relaxation event occurs. The cyclicity is a crucial parameter for optimizing the readout and initialization dynamics (which will be explored in Section 5.1). Generally, a spin-flipping decay event erases the quantum information in a coherent superposition state of the two spin levels. Because of this, optimizing the cyclicity is crucial for experimental use-cases of the tin-vacancy center. Since the cyclicity is determined by the spatial distribution of the wavefunctions, it makes sense that there is a relation between the cyclicity and parameters such as the strain and magnetic field. The top panel of Figure 2.4b shows the relation between the cyclicity and the polar angle of the magnetic field (for an azimuthal angle that is aligned with the dipole orientation of the emitter). The figure shows a clear decrease in cyclicity for higher strain regimes regardless of the magnetic field orientation. This can be explained by the fact that strain components in the Hamiltonian tend to overlap the spin eigenstates that would be orthogonal in its absence. Moreover, the cyclicity is always optimized for magnetic fields that are aligned to the symmetry axis of the dipole moment. This can intuitively be understood from the fact that such a magnetic field maximizes the energy difference between the spin eigenstates of the spin-orbit coupling and thereby minimizes their overlap.

Next to the cyclicity, the orientation of the magnetic field also influences the splitting between the two spin-conserving transitions, as shown in the lower panel of Figure 2.4b. The theoretical predictions in Figure 2.4 are essential for three reasons. Firstly, the experimental results are always obtained through excitation of the two spin-conserving transitions. The ability to predict their splitting at different magnetic field configurations is important for experimental design reasons. For example, the setup of the optical paths (Section 3.1.1) does not allow for arbitrarily large frequency differences between the two resonant laser paths. Secondly, the splitting rate is an essential parameter for the experimental ability to get the transitions of two different emitters on resonance by tuning the magnetic field strength. This concept will be further explored in Section 4.4. Finally, the splitting profile can experimentally be used as a probe for the strain magnitude of a given tin-vacancy center. Formally, this can be done by a fit of the Hamiltonian (as later demonstrated in Section 4.4), but visually the strain level can be roughly estimated through the characteristic strain-induced splitting at perpendicular magnetic fields. The observation of non-zero splitting at magnetic fields perpendicular to the dipole moment can be understood by realizing that strain effectively tilts the spin quantization axis away from the dipole moment as it competes with the spin-orbit coupling [69]. As a consequence, a magnetic field perpendicular to the dipole moment still exhibits Zeeman splitting, since it is not orthogonal to the spin quantization axis.

In summary, the combination of magnetic field dependent effects on the transition frequencies and cyclicities lead to a complex trade-off in the choice of ideal experimental parameters such as magnetic field strength, magnetic field orientation, optical driving powers, etc. The complexity only increases when one considers parameters outside this model such as the excitation polarization, non-radiative decay channels and fluctuating charge environments. It is not immediately clear what the perfect set of parameters for an entanglement experiment is, but such a set of parameters can be found through simulation given physical parameters of the specific tin-vacancy center such as dipole orientation and strain parameters. The thorough understanding that is developed for the tin-vacancy center in this section can be used as a baseline for estimating effects of experimental parameters on the optical manifold.

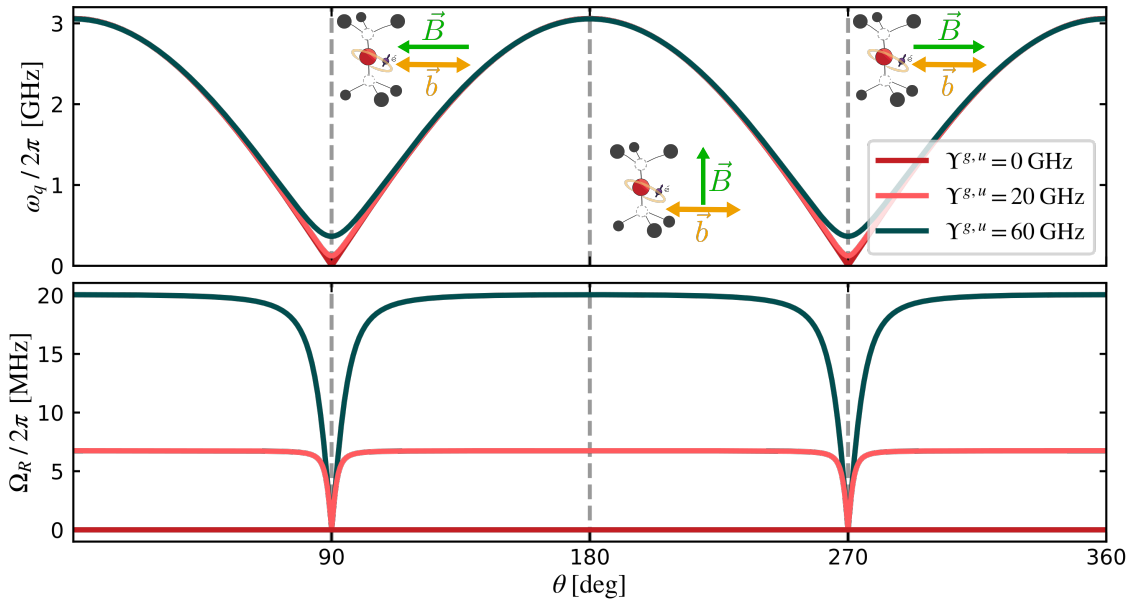

Figure 2.5: The influence of a 100 mT external magnetic field on the qubit transition, both in terms of the transition frequency (top panel) and Rabi rate (bottom panel) under driving of a resonant oscillating field in the x-direction ($\phi = 0°$, $\theta = 90°$). The θ-axis is the same as in Figure 2.4b and the same strain values are shown as in that Figure. The schematic near the vertically dotted gray lines indicate the relative directions between the dipole moment (drawing), external magnetic field (green) and oscillating driving field (orange). The figure highlights the importance of both strain and external magnetic field components perpendicular to the driving field.

2.1.4. The qubit transition and microwave spin control

To make the tin-vacancy center a useful quantum node, it needs to have a well-defined computational basis with sufficiently long coherence times [82, 83]. For the tin-vacancy center, the most natural choice of such computational basis states are the spin states of the lower branch of the ground state: $|0\rangle \equiv |e^g_- \uparrow\rangle$ and $|1\rangle \equiv |e^g_+ \downarrow\rangle$. These states will be referred to as the *electron spin states*. To perform meaningful algorithms, the control over the states in the computational basis should extend over the full Bloch sphere. Optically driving the qubit transition (analogous to Section 2.1.3) would be impossible, because the dipole operator matrix elements between the computational basis states is zero (since they have the same parity) [46]. Therefore, a different type of perturbation is needed to control the transition between the computational basis states. Given that they are defined as spin states, one such perturbation is an oscillating magnetic field $\boldsymbol{b}$. The interaction Hamiltonian of the perturbation caused by such an oscillating magnetic field is given through the Zeeman effect as

$$\hat{H}'_{MW} = \frac{\hbar\gamma_S}{2}\hat{I}\otimes\hat{\mathbf{S}}^{g,u}\cdot\boldsymbol{b} + \frac{\hbar\gamma_L}{2}b_z L_z\otimes\hat{I}, \tag{2.19}$$

when written in the diagonalized spin-orbit Hamiltonian basis. Calculating the effect of such a perturbation on the eigenstates of the full Hamiltonian is a non-trivial task and results will be heavily dependent on many parameters. One quantity of particular interest is the Rabi oscillation frequency, which can be expressed as

$$\Omega_R = \frac{1}{\hbar}\langle 1|\hat{H}'_{MW}|0\rangle\,. \tag{2.20}$$

By simulating the Hamiltonian, the Rabi rate can be calculated through the determination of this matrix element of the perturbation Hamiltonian under varying conditions. Figure 2.5 gives an overview of the simulated qubit-transition and Rabi frequencies for the same strain regimes and magnetic field angles as Figure 2.4b. As indicated by the orange lines in the schematics, the driving field is here taken in the x-direction, while sweeping the polar angle θ of the external magnetic field at a fixed azimuthal angle of $\phi = 0°$. The lower panel of the figure demonstrates how the efficiency of microwave driving (as measured by the Rabi rate) is highly dependent on the strain magnitude. Intuitively (and similarly to the optical transitions), strain creates an overlap between the orthogonal eigenstates of the SnV Hamiltonian with respect to the perturbation Hamiltonian of the magnetic driving field. Moreover, the figure also clearly shows how the efficiency of the MW driving depends on

the orientation of the magnetic field. The dips in the lower panel indicate orientations of the magnetic field that are perfectly parallel to the oscillating driving field and thereby perpendicular to the dipole moment (as indicated by the arrows in the schematics). The interaction terms for these magnetic field orientations are only non-zero due to the orbital Zeeman effect, which is orders of magnitude weaker than the spin Zeeman effect. From this, it can be concluded that a perpendicular component of the driving field $\boldsymbol{b}$ with respect to the external magnetic field $\boldsymbol{B}$ is desirable for efficient microwave spin-control.

The effect of the magnetic field orientation on the driving dynamics of the spin in the computational basis adds another layer of complexity to the choice of an operating point for the magnetic field orientation. Next to the orientation of the magnetic field, its magnitude also has an influence on the spin dynamics. The Rabi rate of the spin dynamics is unaffected by a change of the magnitude of the external magnetic field, but this is not the case for the qubit transition frequency, whose magnitude can be calculated analytically from the Zeeman Hamiltonian. An analytical derivation similar to [49] leads to a first-order approximation of the qubit frequency at aligned magnetic field of

$$\omega_q \approx \frac{2\gamma_S |\mathbf{B}| \Upsilon^g}{\Delta^g}. \tag{2.21}$$

The relation shows how an increase in the magnetic field strength results in a linear increase of the size of the splitting between the two computational basis states. This fact is highly relevant given the fact that the oscillating magnetic field has to be on resonance with ω_q. The creation of short MW pulses at frequencies above 6 GHz is not possible with the setup (as will be explained in Section 3.1.3), leading to a hard cut-off in the magnetic field strength that can be used in experiments involving coherent spin-control. Even more so, transmission of high-frequency MW pulses is technologically challenging, leading to higher losses in the delivery. This leads to a natural trade-off between worse MW driving efficiencies at higher magnetic field strengths, but more separated spin-conserving transitions. Higher separation of the spin-conserving transitions can be advantageous for selectivity of short optical pulses and for the tuning range of resonances.

2.2. Two-Photon Quantum Interference

This section develops the relevant theoretical background for a particular mechanism in Quantum Optics: Two-Photon Quantum Interference. The effect plays a central role in most remote entanglement schemes for erasing "which-path information" of photons [84] and is often one of the limiting technical challenges for experimental realizations of such schemes [85]. This section will start by describing the general theoretical framework, starting from the basic principle of the Hong-Ou Mandel effect and working towards a time-resolved treatment of photon interference between photonic wavepackets generated by sources that experience spectral diffusion. The section will conclude with a theoretical model for interpreting values from measurements in Chapter 7 into theoretical parameters such as *indistinguishability* and *visibility*.

2.2.1. Time-resolved photon interference

This section will present the theoretical framework that can be used to study interference of indistinguishable photons at a beam splitter. The theoretical description is heavily inspired by a combination of the approaches in [86, 87]. The general setup for the theoretical model is presented in Figure 2.6a. We consider two instances of an optically active two-level system. Both systems are simultaneously excited, leading to the emission of a single photon at both systems. which is directed to an input port of a central beam splitter. Quantum mechanically, the photon occupying input port $i \in \{1,2\}$ can be described as a continuous superposition of single-frequency photon states, which can mathematically be represented by

$$|1_i\rangle = \left(\int_{-\infty}^{\infty} \Phi_i(\omega) \hat{a}_i^\dagger(\omega)\, d\omega \right) |vac\rangle\,, \tag{2.22}$$

where $\hat{a}_i^\dagger(\omega)$ is the creation operator of a photon state with a single angular frequency ω, $\Phi_i(\omega)$ represents the normalized spectral amplitude of the photon in that arm and $|vac\rangle$ denotes the quantum mechanical vacuum state in the modes of the input ports. The spectral amplitude can be related to the temporal shape $\zeta_i(t)$ of the photons through the Fourier transform

$$\zeta(t) = \frac{1}{\sqrt{2\pi}} \int_{-\infty}^{\infty} \Phi_i(\omega) e^{-i\omega t}\, d\omega. \tag{2.23}$$

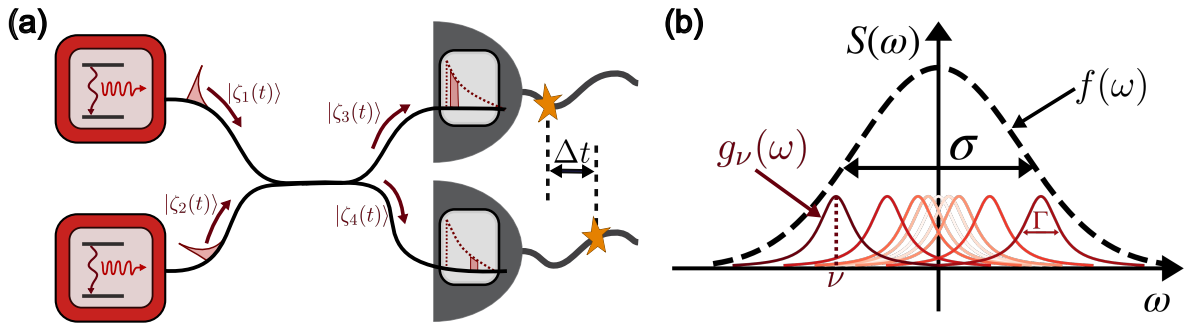

Figure 2.6: Schematic representations for the theoretical framework describing Two-Photon Quantum Interference. (a) A schematic showing the idealized experimental setup that is modeled by the theoretical framework. The single photon sources are assumed to be two-level systems, generating single photons through spontaneous emission. The emitted photons are directed to the input ports of a central beam splitter with ideal non-photon resolving detectors at both output ports. The detection events are indicated by electrical signals (orange sparks), separated by a time Δt, which is the time difference between the detection events. (b) Schematic showing the effect of spectral diffusion as a Gaussian envelope of Lorentzian spectral profiles of the single photons with lifetime-limited linewidths $\left(\Gamma = \frac{1}{2\pi\tau_{\text{life}}}\right)$. Heavily inspired by [87].

Similarly, the electric field operators in each of the beam splitter ports can be defined as inverse Fourier transforms of the single-frequency photon operators through

$$\hat{E}_i^\dagger(t) = \frac{1}{\sqrt{2\pi}} \int_{-\infty}^{\infty} \hat{a}_i^\dagger(\omega) e^{i\omega t}\, d\omega. \tag{2.24}$$

From this, the effect of the electric field operators can directly be derived as

$$\hat{E}_i^\dagger(t)\,|0_i\rangle = \zeta_i(t)\,|1_i\rangle\,. \tag{2.25}$$

To analyze the effect of interference between two incoming photons at the output ports, we first need to describe the quantum state of two such incoming photons in the input modes $i = 1$ and $i = 2$. This state can be defined as a product state between individual instances of Equation 2.22, leading to

$$|1_1\,1_2\rangle = \left(\int_{-\infty}^{\infty} \Phi_1(\omega_1)\hat{a}_1^\dagger(\omega_1)\, d\omega_1\right)\left(\int_{-\infty}^{\infty} \Phi_2(\omega_2)\hat{a}_2^\dagger(\omega_2)\, d\omega_2\right)|vac\rangle\,. \tag{2.26}$$

Crucially however, the detection can only be described in the basis that is defined by the eigenstates in the output port modes $i = 3$ and $i = 4$. To transform the state in Equation 2.26 to that basis, we need to know the relation between the single-frequency photon operators of the input- and output ports of the beam splitter. These relations can be derived from first principles given the ratio of reflection and transmission of the beam splitter [80]. Here, the relations are simply stated directly for a perfectly balanced beam splitter:

$$\begin{cases} \hat{a}_3^\dagger = \frac{1}{\sqrt{2}}\left(\hat{a}_1^\dagger + \hat{a}_2^\dagger\right) \\ \hat{a}_4^\dagger = \frac{1}{\sqrt{2}}\left(\hat{a}_1^\dagger - \hat{a}_2^\dagger\right) \end{cases}. \tag{2.27}$$

From these relations, Equation 2.26 can be rewritten in terms of the $\hat{a}_3^\dagger$ and $\hat{a}_4^\dagger$ operators as

$$|1_1\,1_2\rangle = \frac{1}{2}\left[\int_{-\infty}^{\infty}\int_{-\infty}^{\infty} \Phi_1(\omega_1)\Phi_2(\omega_2)\left(\hat{a}_3^\dagger(\omega_1) + \hat{a}_4^\dagger(\omega_1)\right)\left(\hat{a}_3^\dagger(\omega_2) - \hat{a}_4^\dagger(\omega_2)\right) d\omega_1\, d\omega_2\right]|vac\rangle\,. \tag{2.28}$$

Writing the incoming state in terms of the $\hat{a}_3^\dagger(\omega)$ and $\hat{a}_4^\dagger(\omega)$ operators allows us to calculate the detection probabilities using the field operators of the two output arms $\left(\hat{E}_3^\dagger \text{ and } \hat{E}_4^\dagger\right)$. More specifically, the particular quantitiy of interest is the probability that the two photons get detected at the two different output ports of the beam-splitter, with a time τ between the detection events (as indicated in Figure 2.6a). The time-evolution of this probability can be expressed in terms of the field operators and the incoming state as:

$$P_{coinc}(t,\Delta t) = \left|\hat{E}_4(t+\Delta t)\hat{E}_3(t)\,|1_1\,1_2\rangle\right|^2 = \left\langle 1_1\,1_2\left|\hat{E}_3^\dagger(t)\hat{E}_4^\dagger(t+\Delta t)\hat{E}_4(t+\Delta t)\hat{E}_3(t)\right|1_1\,1_2\right\rangle, \tag{2.29}$$

where t denotes the absolute time (for example with respect to the excitation events). Substituting the definitions of the field operators in Equation 2.24 into the definition of the $|1_1\,1_2\rangle$ state in Equation 2.28 gives an expression for the probability of detection events at the two detectors separated by a time Δt, which can be written in terms of the temporal wavefunctions of the incoming photons as

$$P_{coinc}(t,\Delta) = \frac{1}{4}\,|\zeta_1(t+\Delta t)\zeta_2(t) - \zeta_1(t)\zeta_2(t+\Delta t)\,|^2\,. \tag{2.30}$$

Equation 2.30 reveals an interesting effect, which can be highlighted by considering two identical photons with $\zeta_1(t) = \zeta_2(t) = \zeta(t)$. A quick evaluation of Equation 2.30 reveals that the probability of measuring coincidences between these two photons is exactly 0. This direct consequence of the beam splitter relations is called the Hong-Ou Mandel effect (after Chung Ki Hong, Zheyu Ou and Leonard Mandel) [88]. Concretely, the effect predicts that two indistinguishable photons arriving at two different input arms of a beam splitter will always be detected on the same output. This means that all information about the source of the photons is lost after their interference at the beam splitter. This erasure of the so-called "which-path information" is an essential ingredient for remote entanglement schemes [84]. Equation 2.30 gives a concrete way of converting knowledge about the wavefunctions of the individual photons to their predicted interference pattern. This relation will be leveraged in the following sections to predict interference patterns for photons generated by tin-vacancy centers.

2.2.2. Spectral diffusion

The previous section showed a theoretical framework for analyzing Two-Photon Quantum Interference effects between photons with arbitrary wavefunctions, highlighting the Hong-Ou Mandel effect for photons with completely equal wavefunctions (i.e. photons that are *indistinguishable*). The theoretical framework will be leveraged in this section to develop a more realistic model including spectral diffusion. This model will be used to predict the relation between spectral diffusion and the indistinguishability. A more in-depth analysis of spectral diffusion on the autocorrelation function of the detection events can be found in Appendix B.2.

In the case of photons originating from spontaneous emission, the temporal wavefunction follows an exponential distribution. An exponential temporal wavefunction can be translated to a Lorentzian shape in frequency domain through a Fourier transformation

$$\zeta(t) \sim e^{-\frac{t}{2\tau}} e^{-i\omega t}\Theta(t) \overset{\text{Fourier}}{\Longleftrightarrow} \Phi_\nu(\omega) \sim \frac{\sqrt{\Gamma/2}}{(\nu-\omega) + i\frac{\Gamma}{2}} \equiv g_\nu(\omega), \tag{2.31}$$

in which $\Theta(t)$ is the Heaviside function, τ is the decay time of the spontaneous emission process (i.e. the lifetime), ν is the central frequency of the photon and Γ is the transform-limited linewidth. The relation between the lifetime τ and Lorentzian linewidth Γ can directly be derived from the Fourier transform in Equation 2.31 as $\Gamma = \frac{1}{2\pi\tau}$. For the realization of perfect interference between two photons described by Equation 2.31, both should have the same central frequency ν and decay rate Γ. Unfortunately though, the experimental generation of such single photons is extremely difficult and is often regarded as one of the main limitations for the fidelity of remote entanglement generation with solid-state defects [85]. The most dominant influence on the distinguishability of photons created by solid-state defects is spectral diffusion. The effect of spectral diffusion is schematically demonstrated in Figure 2.6b. Spectral diffusion originates from a fluctuating charge distribution in the space around the defect, which directly causes shifts in the energy levels of the Hamiltonian, effectively causing a fluctuating transition frequency for the spontaneous emission of the single photons. Typically, spectral diffusion is best modeled in the frequency domain, as its effect can be expressed as a Gaussian convolution of lifetime-limited Lorentzian distributions. Given that spectral diffusion is a non-coherent process, the full state of a photon generated by a spectrally diffusing source is best described as a density matrix with diagonal elements determined by the Gaussian profile of the spectral diffusion. Assuming different spectral diffusion profiles $f_{1,2}(\nu)$ on both photon sources, the density matrices of the two incoming photons before the beam splitter can be written as

$$\rho_i = \int_{-\infty}^{\infty} f_i(\nu)\,|\nu_i\rangle\,\langle\nu_i|\;d\nu. \tag{2.32}$$

The $|\nu_i\rangle$ states in Equation 2.32 are defined as lifetime-limited Lorentzian-shaped photons through Equations 2.22 and 2.31. Knowing the density matrices of both incoming photons, their indistinguishability can be quantified by the sum of all possible frequency combinations, weighted by the overlap of the wavefunctions for those combinations and the probabilities of their occurrences as determined by the spectral diffusion profiles. Without assuming anything about the spectral diffusion distributions on both sides or the temporal shapes of the photons, the indistinguishability can be written as

$$\eta = \mathrm{Tr}\left[\rho_1 \otimes \rho_2\right] = \int_{-\infty}^{\infty}\int_{-\infty}^{\infty} f_1(\omega_1) f_2(\omega_2) \left|\langle\omega_1|\omega_2\rangle\right|^2 \, d\omega_1 \, d\omega_2. \tag{2.33}$$

Considering $|\omega_1\rangle$ and $|\omega_2\rangle$ to have Lorentzian spectral profiles, their overlap can be derived analytically as

$$\langle\omega_1|\omega_2\rangle = \int_{-\infty}^{\infty} g^*_{\omega_1}(\nu) g_{\omega_2}(\nu) d\nu = \cdots = i\frac{\sqrt{\Gamma_1\Gamma_2}}{(\omega_1-\omega_2)+i(\Gamma_1+\Gamma_2)}. \tag{2.34}$$

The presence of Γ_1 and Γ_2 in Equation 2.22 indicates that no assumption of equal lifetimes of the photon sources was made. By assuming the spectral diffusion on both sources to be Gaussian (with standard deviations of $\sigma_{1,2}$), an expression for the indistinguishability can be found by combining Equations 2.33 and 2.34

$$\eta = \frac{\Gamma_1\Gamma_2}{2\pi\sigma_1\sigma_2(\Gamma_1+\Gamma_2)^2} \int_{-\infty}^{\infty}\int_{-\infty}^{\infty} \frac{\exp\left[-\frac{(\omega_1-\omega)^2}{2\sigma_1^2} - \frac{(\omega_2-\omega)^2}{2\sigma_2^2}\right]}{1+\left(\frac{\omega_1-\omega_2}{\Gamma_1+\Gamma_2}\right)^2} \, d\omega_1 \, d\omega_2. \tag{2.35}$$

This integral is solved numerically and the result is shown in Figure 2.7a, in which the spectral diffusion is assumed equal on both single-photon sources. The lifetime of both single photon sources is also assumed equal and is taken at 7ns, which translates to $\Gamma = 22.7$ MHz. The horizontal axis in this figure shows the Full-Width at Half Maximum (FWHM) of the spectral convolution of the Gaussian profile with the corresponding lifetime-limited Lorentzian profiles. This measure is directly related to the magnitude of the spectral diffusion σ, but chosen instead because it can be measured experimentally (see Section 4.2). The figure clearly shows the detrimental effect of spectral diffusion on the maximally achievable indistinguishability.

Seeing as spectral diffusion causes distinguishability, it is fair to say that there is some correlation between the amount of spectral diffusion and the probability of simultaneous detection events on the two different output ports. More specifically, it turns out that the spectral diffusion causes a predictable pattern in the time differences between detection events. The exact probability distribution of coincident detection events[1] can be calculated analytically. This derivation is done in Appendix B.2. The resulting function is found through numerical integration and is depicted in Figure 2.7b. As expected, without spectral diffusion there are no coincidences at any time difference since the photons are completely indistinguishable. However, as the distinguishability increases with an increasing amount of spectral diffusion, the coincidence probability starts showing a dip, connected to two "blobs" of coincidences. The size of the dip decreases with an increasing amount of spectral diffusion, which means that the effect of spectral diffusion on the indistinguishability can be mitigated through temporal filtering of detection events, where the strictness of the temporal filtering is determined by the level of spectral diffusion in the single photons sources. The limiting case of infinitely large spectral diffusion ($\sigma \to \infty$) represents the same autocorrelation function as for two distinguishable photons (as derived in Appendix B.1)

2.2.3. Model of experimental measurements

In an ideal experiment, the indistinguishability can be measured by repeatedly sending simultaneously generated photons to a beam splitter and observing the number of simultaneous detection events at the two output ports. However, due to experimental imperfections (dark counts, laser leakage, etc.), the number of measured coincidences contain many noise factors, which are not related to the actual photonic indistinguishability at all. To differentiate between measured coincidence probabilities and actual photon properties, we define

[1] The terms *coincident detection events*, *coincident detections* and *coincidences* are all used to refer to instances where a photon is detected at detector 1 at some time t and another photon is detected at detector 2 at time $t+\Delta t$. Here, Δt can be both negative and positive, but is always defined with respect to a detection event on detector 1 (as also reflected in Equation 2.29

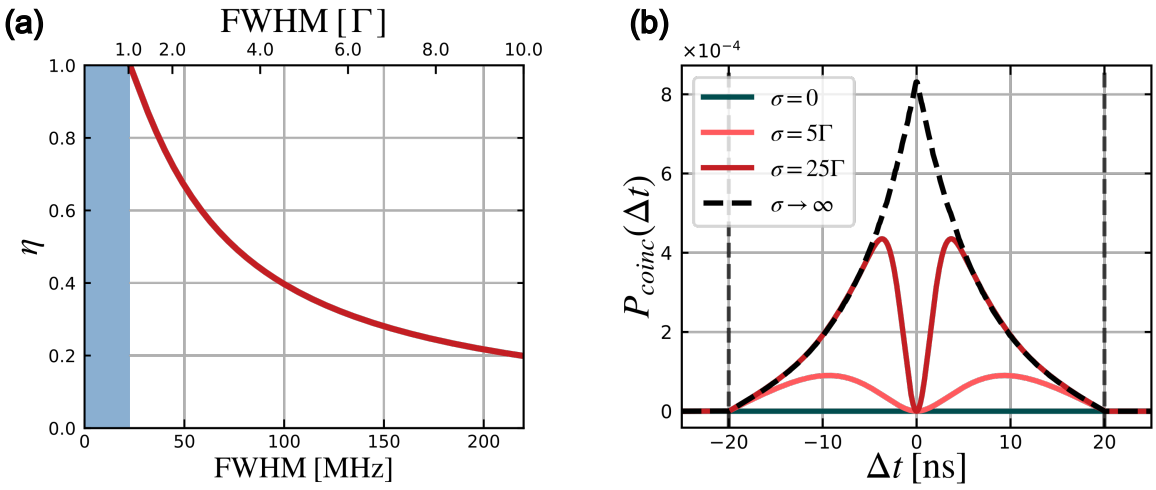

Figure 2.7: The influence of spectral diffusion on coincidences in detection events. (a) The relation between the indistinguishability of photons and the level of spectral diffusion at both of the photon sources (which are assumed to be equal). The horizontal axis shows the Full Width at Half Maximum (FWHM) of the convolution of the Gaussian spectral diffusion with the lifetime-limited Lorentzian spectral profiles. The lifetime of both nodes is taken as 7 ns, which translates into a lifetime-limited linewidth of $\Gamma = 22.7$ MHz (as illustrated by the blue shaded region). (b) The shape of the distribution of coincident detection events for four different spectral diffusion magnitudes in a 20ns measurement window (indicated by gray vertical dotted lines). The magnitude of the spectral diffusion is expressed here as the value of the standard deviation σ of its Gaussian distribution. The overall probability of a coincident detection event clearly increases with an increasing amount of spectral diffusion, while the width of the dip around $\Delta t = 0$ decreases. This means that the requirements in terms of temporal filtering become more stringent in situations with higher spectral diffusion. Without any spectral diffusion, the photons are perfectly indistinguishable, which leads to zero coincidence probability for all Δt. The limit of $\sigma \to \infty$ shows same profile as two distinguishable photons (see Appendix B.1).

different quantities for both. The *visibility* (V) is defined as the total number of measured coincidences, normalized as a ratio of the expected coincidences for fully distinguishable photons. The visibility is directly calculated from the measured coincidences and thereby contains all noise sources causing the coincidences (one of which is distinguishability of the photons). The *indistinguishability* (η) is then defined as a corrected version of the visibility, where measured coincidences from known noise sources are subtracted to isolate a measure of the erasure of "which-path information". This section will develop the model that is used to extract both the indistinguishability and visibility from measurements of coincidences in experiments.

We consider an experiment with N excitations of the single-photon sources in Figure 2.6a. For notation, the sources are defined with subscripts "A" and "B" and the detectors with "1" and "2". Due to photon losses in the experimental optical paths, not each photon emission event at the sources will lead to a detection event. Moreover, each detection event can either originate from a photon that was emitted by the single-photon source (denoted as SnV), or from some source of noise (dark counts of the detectors, laser leakage in the measurement window, fiber fluorescence, etc; denoted as DC). Both of these fundamental observations are reflected in the following definitions of the detection probabilities:

$$\begin{cases} p_{A\to1} = p^{SnV}_{A\to1} + p^{DC}_{A\to1} \\ p_{A\to2} = p^{SnV}_{A\to2} + p^{DC}_{A\to2} \\ p_{B\to1} = p^{SnV}_{B\to1} + p^{DC}_{B\to1} \\ p_{B\to2} = p^{SnV}_{B\to2} + p^{DC}_{B\to2}, \end{cases} \tag{2.36}$$

where $p^{SnV}_{S\to i}$ is defined as the probability of detecting a photon that was emitted by the single-photon source $S \in \{A,B\}$ at detector $i \in \{1,2\}$. $p^{DC}_{S\to i}$ is defined in the same way, but for noise counts. With these definitions, the probability of coincident detections for two fully distinguishable photons can simply be written as

$$P^{dist}_{coinc}(\tau = 0) = p_{A\to1} \cdot p_{B\to2} + p_{A\to2} \cdot p_{B\to1}. \tag{2.37}$$

So, a measurement with N_{coinc} coincident detection events leads to a visibility of

$$V = 1 - \frac{N_{coinc}}{N \cdot P^{dist}_{coinc}(\tau = 0)}. \tag{2.38}$$

Contrary to the relatively straight-forward extraction of the visibility from the measurement, the estimation of the indistinguishability is a bit more complex. To obtain the indistinguishability of the photons, the coincidences that were caused by known noise sources should be subtracted from N_{coinc} in Equation 2.38. To estimate this contribution, it is assumed that there is zero interference between the spontaneously emitted single-photons and noise counts. The coincidences caused by noise sources can then be expressed as the probability of measuring coincidences in which at least 1 of the detections is a dark count

$$\begin{aligned} P^{DC}_{coinc}(\tau = 0) = &\left(p^{SnV}_{A\to 1} + p^{SnV}_{B\to 1}\right)\left(p^{DC}_{A\to 2} + p^{DC}_{B\to 2}\right) + \\ &\left(p^{DC}_{A\to 1} + p^{DC}_{B\to 1}\right)\left(p^{SnV}_{A\to 2} + p^{SnV}_{B\to 2}\right) + \\ &\left(p^{DC}_{A\to 1} + p^{DC}_{B\to 1}\right)\left(p^{DC}_{A\to 2} + p^{DC}_{B\to 2}\right). \end{aligned} \tag{2.39}$$

The measured indistinguishability is then defined by subtracting these known noise contributions from the measured coincidences in Equation 2.38

$$\eta = \frac{\frac{N_{coinc}}{N} - P^{DC}_{coinc}}{p^{SnV}_{A\to 1} \cdot p^{SnV}_{B\to 2} + p^{SnV}_{A\to 2} \cdot p^{SnV}_{B\to 1}}. \tag{2.40}$$

The main difficulty in obtaining this measure is the estimation of $p^{SnV}_{(A,B)\to(1,2)}$ and $p^{DC}_{(A,B)\to(1,2)}$. By only considering data obtained from detection events that can originate from both sources, it is impossible to do this. Instead, data from additional experiments is needed. These additional experiments should discriminate between photons originating from the two sources, which can most easily be done by only exciting one of the two photon sources. When doing this, only a single photon arrives at the beam splitter after each excitation, meaning that all coincidences are caused by sources of noise. The relation between the measured coincidence probabilities in these experiments $P^{A,B}_{coinc}$ and the individual detection probabilities can be derived from the fact that coincidences always arise from noise sources

$$P^{(A,B)}_{coinc} = p^{SnV}_{(A,B)\to 1}\, p^{DC}_{(A,B)\to 2} + p^{DC}_{(A,B)\to 1}\, p^{SnV}_{(A,B)\to 2} + p^{DC}_{(A,B)\to 1}\, p^{DC}_{(A,B)\to 2}. \tag{2.41}$$

Next to the coincidence probability, the probability of detection events in consecutive repetitions of the experiment is also needed. This probability can be expressed as

$$P^{(A,B)}_{consecutive} = p_{(A,B)\to 1} \cdot p_{(A,B)\to 2} = (p^{SnV}_{(A,B)\to 1} + p^{DC}_{(A,B)\to 1}) \cdot (p^{SnV}_{(A,B)\to 2} + p^{DC}_{(A,B)\to 2}). \tag{2.42}$$

The four equations described by 2.41 and 2.42 can be used to extract the values of the 8 variables of interest by assuming that the ratio between dark counts and emitted photons is much smaller than 1 for both detectors and both subsetups (as is verified in Section 6.1), such that

$$\alpha_{A,B} = \frac{p_{(A,B)\to 1}}{p_{(A,B)\to 2}} \approx \frac{p^{SnV}_{(A,B)\to 1}}{p^{SnV}_{(A,B)\to 2}}. \tag{2.43}$$

Under this assumption, the values of the eight variables of interest can be obtained from the measured values of $p_{(A,B)\to(1,2)}$, $P^{(A,B)}_{coinc}$ and $P^{(A,B)}_{consecutive}$ through the following expressions:

$$\begin{cases} p^{SnV}_{(A,B)\to 1} = \sqrt{\alpha_A \left(P^{(A,B)}_{consecutive} - P^{(A,B)}_{coinc}\right)} \\ p^{SnV}_{(A,B)\to 2} = \sqrt{\frac{1}{\alpha_A} \left(P^{(A,B)}_{consecutive} - P^{(A,B)}_{coinc}\right)} \\ p^{DC}_{(A,B)\to 1} = p_{(A,B)\to 1} - \sqrt{\alpha_A \left(P^{(A,B)}_{consecutive} - P^{(A,B)}_{coinc}\right)} \\ p^{DC}_{(A,B)\to 2} = p_{(A,B)\to 2} - \sqrt{\frac{1}{\alpha_A} \left(P^{(A,B)}_{consecutive} - P^{(A,B)}_{coinc}\right)}. \end{cases} \tag{2.44}$$

Finally, the estimates of the values of $p^{(SnV,DC)}_{(A,B)\to(1,2)}$ from the two additional single-emitter experiments (calculated from Equation 2.44) can be combined with the number of measured coincidences in the original two-emitter experiment through Equation 2.40 to get an estimate for the actual indistinguishability of the photons generated by excitation of the two single-photon sources. The theoretical framework in this section can also be extended to estimate the probability distribution of the indistinguishability for a given measurement outcome with a finite number of events. The model for this error propagation analysis is presented in Appendix B.3.

2.3. Remote Entanglement Generation

The research in this work is motivated by the overarching goal of creating remote entanglement between two tin-vacancy centers. To get a better understanding of the exact system requirements for such an achievement, it is important to understand the envisioned protocol for creating entanglement. More specifically, this chapter will focus on a particular algorithm for remote entanglement generation: The double-click protocol. This protocol was first proposed by Sean Barett and Pieter Kok in 2005 [89] and has been used experimentally on multiple different platforms [22–24, 27, 30, 32]. The section will start with a breakdown of the steps involved in the algorithm, showcasing all the experimental capabilities that are needed for the experimental realization of it. After this, the section will proceed with a derivation of the influence of non-perfect visibility in Two-Photon Quantum Interference on the fidelity of the final state between the two entangled parties.

2.3.1. The double-click algorithm

An idealized representation of the setup and steps in the double-click entanglement scheme are presented in Figure 2.8. The setup contains two remote nodes, each of which is described as a three-level system with two non-degenerate spin states in the ground state and a single excited state. The nodes are both connected to a quantum channel which is assumed to have perfect transmission of photons towards the central beam splitter. The two output ports of this beam splitter are connected to ideal detectors, which are non photon-number resolving.

Step (1) of the protocol is the initialization of both spin states into a pure eigenstate of the Hamiltonian (in this case $|\uparrow\rangle$). The initialization is done through spinpumping (see Section 2.1.3), after which the total state of the system can be written as

$$|\Psi_1\rangle = |\uparrow\rangle_A |vac\rangle_A \otimes |\uparrow\rangle_B |vac\rangle_B . \tag{2.45}$$

The subscripts A and B refer to the node on the left and right side in Figure 2.8 respectively. The $|\uparrow / \downarrow\rangle_{A,B}$ states are eigenstates of the respective Hamiltonians of the nodes and the $|vac\rangle_{A,B}$ states denote the vacuum states in the quantum channels connecting the nodes to the input ports of the central beam splitter. After initialization, the algorithm proceeds to generate equal superpositions of the spin states on both nodes through a $\pi/2$-rotation, leaving the system in a superposition state

$$|\Psi_2\rangle = \frac{1}{\sqrt{2}} (|\uparrow\rangle_A + |\downarrow\rangle_A) |vac\rangle_A \otimes \frac{1}{\sqrt{2}} (|\uparrow\rangle_B + |\downarrow\rangle_B) |vac\rangle_B . \tag{2.46}$$

Following this, a selective π-pulse is applied at both nodes to the $|\uparrow\rangle - |e\rangle$ transition. The selectiveness of this π-pulse leads to entanglement between the photonic state in the quantum channels and the spin states of the notes, which can mathematically be presented as

$$|\Psi_3\rangle = \frac{1}{2} (|\uparrow\rangle_A |E\rangle_A + |\downarrow\rangle_A |vac\rangle_A) \otimes (|\uparrow\rangle_B |E\rangle_B + |\downarrow\rangle_B |vac\rangle_B) . \tag{2.47}$$

The notation $|E\rangle_{A,B}$ in Equation 2.46 is used to denote the occupation of a photon in an "early" time bin (already hinting at the next steps of the protocol). In principle, a measurement of only a single photon after the interference at the beam splitter between $|E\rangle_A$ and $|E\rangle_B$ would collapse the total state of the system into a mixed state with some degree of entanglement. To actually generate a maximally entangled state between the spins at both nodes, the double-click protocol proposes a second round of excitation, but now selective on the other term in the superposition. To achieve this, the spin state population is first inverted by a π-rotation in the spin basis, putting the system in a state

$$|\Psi_4\rangle = \frac{1}{2} (|\uparrow\rangle_A |vac\rangle_A + |\downarrow\rangle_A |E\rangle_A) \otimes (|\uparrow\rangle_B |vac\rangle_B + |\downarrow\rangle_B |E\rangle_B) . \tag{2.48}$$

Then, another spin-selective optical π-pulse resonant with the $|\uparrow\rangle$ - $|e\rangle$ transition introduces the emission of a spin-dependent photon in the "late" time bin, putting the total system in a superposition state described by

$$|\Psi_5\rangle = \frac{1}{2} (|\uparrow\rangle_A |L\rangle_A + |\downarrow\rangle_A |E\rangle_A) \otimes (|\uparrow\rangle_B |L\rangle_B + |\downarrow\rangle_B |E\rangle_B) . \tag{2.49}$$

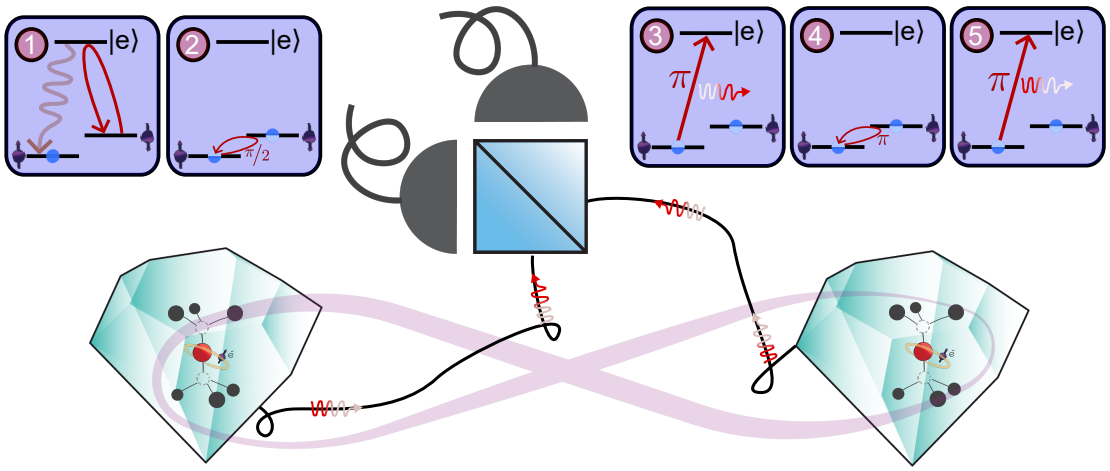

Figure 2.8: Schematic representation of the Barett & Kok "double-click" entanglement generation protocol [89]. Two color centers in diamond are connected to the input ports of a central 50:50 beam splitter through a quantum channel. The output ports of the beam splitter are directed to non photon-number resolving detectors. The protocol assumes a three-level system at each of the nodes. The steps of the protocol are schematically drawn and labeled in the numbered insets.

Finally, if the pairs of photons in each time bin are completely indistinguishable then there is no information at the detectors about their origin. This means that a single detection event in both the early- and late time bin collapses the state into a maximally entangled Bell state between the spin states at the two nodes

$$|\Psi\rangle = \frac{1}{\sqrt{2}}\left(|\uparrow\rangle_A|\downarrow\rangle_B \pm |\downarrow\rangle_A|\uparrow\rangle_B\right), \tag{2.50}$$

where $\pm$ sign reflects whether the clicks in the two time bins were on the same $(+)$ or different $(-)$ detectors.

2.3.2. Infidelity from non-perfect TPQI visibility

The central objective of this work is to demonstrate indistinguishability between photons emitted by two different tin-vacancy centers. The relevance of this achievement is motivated by the central part that this photonic indistinguishability plays in the double-click entanglement protocol, where it is responsible for the erasure of which-path information. To analyze the influence of non-perfect visibility, a model describing the quantum state of the system at each point during the experiment is required. This model can be achieved through the Quantum Jump Formalism, which takes conditional Hamiltonians into account. The derivation of the relation between the TPQI visibility and entanglement fidelity using this formalism that is presented here is based on previous work in [30].

In Section 2.3.1, the two nodes were assumed to have the same resonance frequencies, making phase-tracking during the protocol unnecessary. To observe the effect of non-perfect visibility (induced by shifted resonances), this can however no longer be done. When tracking the phases of all terms, the state of the system after the first excitation (step 3 in Section 2.3.1) can be written as [30]

$$\begin{aligned}|\Psi_3\rangle(t) = \frac{1}{2}\Big[&e^{-i(\omega_\uparrow t - k_A x_A + \omega_A t)}|\uparrow\rangle_A|E\rangle_A + e^{-i\omega_\downarrow t}|\downarrow\rangle_A|vac\rangle_A\Big]\otimes \\ &\Big[e^{-i(\omega_\uparrow t - k_B x_B + \omega_B t)}|\uparrow\rangle_B|E\rangle_B + e^{-i\omega_\downarrow t}|\downarrow\rangle_B|vac\rangle_B\Big],\end{aligned} \tag{2.51}$$

where $\omega_{\uparrow/\downarrow}$ denote the precession frequencies of both spin energy levels, $\omega_{A,B}$ denote the frequencies of the $|\uparrow\rangle_{A,B} - |e\rangle_{A,B}$ transitions and $x_{A,B}$ denote the optical path lengths of the photons from the two nodes. A single detection event on one of the detectors now projects the state into a mixed state, where the two terms reflect the probabilities of the detection being caused by one or two photons:

$$\rho = |\alpha|^2|\Phi_\pm\rangle\langle\Phi_\pm| + |\beta|^2|\uparrow\rangle_A|\uparrow\rangle_B\langle\uparrow|_A\langle\uparrow|_B. \tag{2.52}$$

The exact values of α and β in Equation 2.52 depend on the ratio of detected photons from both emitters and are not necessarily interesting for this derivation. The $+$ and $-$ signs indicate whether the detection event

happened in detector "1" or "2". The $|\Phi_{\pm}\rangle$ state in Equation 2.52 can be written as [30]

$$|\Phi_{\pm}\rangle(t,\tau_1) = \frac{1}{\sqrt{2}}\left[|\downarrow\rangle_A|\uparrow\rangle_B \pm e^{i(k_A x_A - k_B x_B) - i(\omega_A - \omega_B)\tau_1}|\uparrow\rangle_A|\downarrow\rangle_B\right], \tag{2.53}$$

where τ_1 is the time of the first detection event and the time t is taken relative to the time of the first $\pi/2$ MW pulse (step 2 in Section 2.3.1). After the application of the π-pulse on the spins, all spin states in Equation 2.52 get flipped. The second detection induces another collapse of the combined wavefunctions of the spin states, in which the $|\uparrow\rangle_A|\uparrow\rangle_B\langle\uparrow|_A\langle\uparrow|_B$ term in Equation 2.52 is removed. The phase of the final state depends on the detection times τ_1 and τ_2 through

$$|\Psi_{final}\rangle(\tau_1,\tau_2) = \frac{1}{\sqrt{2}}\left[|\downarrow\rangle_A|\uparrow\rangle_B \pm e^{i\phi(\tau_1,\tau_2)}|\uparrow\rangle_A|\downarrow\rangle_B\right], \tag{2.54}$$

where the $\pm$ sign now indicates if the detection events at τ_1 and τ_2 were on the same detector (+) or on different detectors (−) and where

$$\phi(\tau_1,\tau_2) = (\tau_2 - \tau_1)(\omega_A - \omega_B). \tag{2.55}$$

The ideal final entangled state is the Bell state $|\Phi_{\pm}\rangle = \frac{1}{\sqrt{2}}(|\downarrow\rangle_A|\uparrow\rangle_B \pm |\uparrow\rangle_A|\downarrow\rangle_B)$, which means that the actual state that the algorithm generates has a fidelity of

$$F(\phi) = \frac{1}{2} + \frac{1}{2}\cos(\phi). \tag{2.56}$$

In the case of an idealized system, the two nodes would have the same resonances ($\omega_A = \omega_B$) and the fidelity would be 1. However, for defects in solid-state materials this idealization is often not realistic because of the significance of spectral diffusion, causing stochastic shifts of both frequencies. Such stochastic frequency shifts induce random (untracked) phases on the entangled state, which reduce its fidelity. Section 2.2.2 has presented the influence of spectral diffusion on the indistinguishability between the photons. It is interesting to relate the fidelity in Equation 2.56 to the measured indistinguishability, providing an upper bound on the achievable entanglement fidelity from a measured indistinguishability. To this end, we consider both photons to originate from spontaneous emission, making their temporal evolution of the form $\zeta_{A,B}(t) = \epsilon_{A,B}(t)e^{-i\phi_{A,B}(t)}$. Using Equation 2.30, this leads to a probability of measuring a coincidence with events at $t = \tau_1$ and $t = \tau_2$ of

$$\begin{aligned} P_{coinc}(\tau_1,\tau_2) = &\frac{\epsilon_A(\tau_1)^2\epsilon_B(\tau_2)^2 + \epsilon_A(\tau_2)^2\epsilon_B(\tau_1)^2}{4} - \\ &\frac{\epsilon_A(\tau_1)\epsilon_A(\tau_2)\epsilon_B(\tau_1)\epsilon_B(\tau_2)}{8}\cos\left[(\phi_A(\tau_1) - \phi_A(\tau_2)) + (\phi_B(\tau_2) - \phi_B(\tau_1))\right]. \end{aligned} \tag{2.57}$$

The visibility is then defined through Equation 2.38. It should be noted that the first term in Equation 2.57 is exactly the coincidence probability for distinguishable photons. Leveraging this fact and substituting Equation 2.57 into 2.38 gives the relation for the visibility in terms of $\epsilon_{A,B}(\tau_{1,2})$ and $\phi_{A,B}(\tau_{1,2})$. Since the photons originate from spontaneous emission in the two nodes, we know what these functions look like:

$$\begin{cases} \epsilon_{A,B}(t) = \Gamma e^{\Gamma\left((t-t_0) - \frac{x_{A,B}}{c}\right)} \\ \phi(t) = (t - t_0)\omega_{A,B} - k_{A,B}\,x_{A,B}. \end{cases} \tag{2.58}$$

Combining Equations 2.38, 2.57 and 2.58 finally gives a relation between the measured visibility, transition frequencies and detection times:

$$V = \cos((\tau_2 - \tau_1)(\omega_B - \omega_A)). \tag{2.59}$$

Both Equations 2.59 and 2.56 feature the same cosine term. By substituting these two Equations, we finally arrive at a relation between the maximally achievable entanglement fidelity and the visibility in the TPQI experiment given by

$$F(V,\tau_1,\tau_2) = \frac{1}{2} + \frac{V}{2}. \tag{2.60}$$

Concretely, Equation 2.60 shows that a high visibility in Two-Photon Quantum Interference is crucial for the demonstration of high-fidelity remote entanglement between the two photon sources.

3
Experimental setup and methods

This chapter will provide a detailed description of the experimental setup that was used to conduct the experiments in Chapters 4-7. The chapter starts with a description of the hardware configuration of the setup. After this, the fabrication details of the sample will be discussed. The final sections of the chapter will present general capabilities, which are commonly used in the experiments of Chapters 4-7.

3.1. The experimental setup

Figure 3.1 shows a schematic representation of the optics and control electronics that make up the experimental setup. The setup consists of a cryostat (Section 3.1.2) containing a tin-implanted diamond chip with nanophotonic waveguides (Section 3.2). A tapered fiber couples to the optical mode in these waveguides for collection and excitation (Section 3.3). The excitations and collected photons are manipulated and routed with an optical setup (Section 3.1.1). All electronic components are controlled by a combination of a microcontroller, Arbitrary Waveform Generator and Timetagger (Section 3.1.3). The setup is (almost) completely symmetric with respect to the two "subsetups", which are conveniently named "Alice" and "Bob" (the left and right sides in Figure 3.1 respectfully). This section will focus on providing detailed descriptions of the hardware components in Figure 3.1. The description is split up into the optics, cryogenics and control electronics.

3.1.1. Optics

Motivated by the required experimental capabilities for entanglement generation (see Section 2.3), the optics in the setup should be designed in such a way that the following capabilities are possible:

1. The excitation optics can send pulses of $>10\,\mu s$ into the waveguide. For the control of the spin-conserving transitions of a tin-vacancy at non-zero magnetic fields, the optical setup should enable pulses of three wavelengths: The repump wavelength and the wavelengths of the two spin-conserving C-transitions (see Section 2.1.2). The powers and timings of these pulses should be independently controllable on both subsetups.

2. The excitation optics can create pulses of $\sim$1ns on resonance with one of the spin-conserving transitions. This capability can be shared between the subsetups (see Section 7.1).

3. The collection optics should be able to collect single photons emitted in the waveguide mode and efficiently route them to the detectors.

4. The collection optics should be able to separate photons originating from all PSB transitions and those originating from the ZPL of (only) the C-transition (see Section 2.1.3). The collection of the PSB photons has to be independent for both subsetups, while the C-transition ZPL photons have to be directed to a 50:50 beam splitter connecting the two subsetups with two non photon-number resolving detectors at the output ports (see Section 2.2).

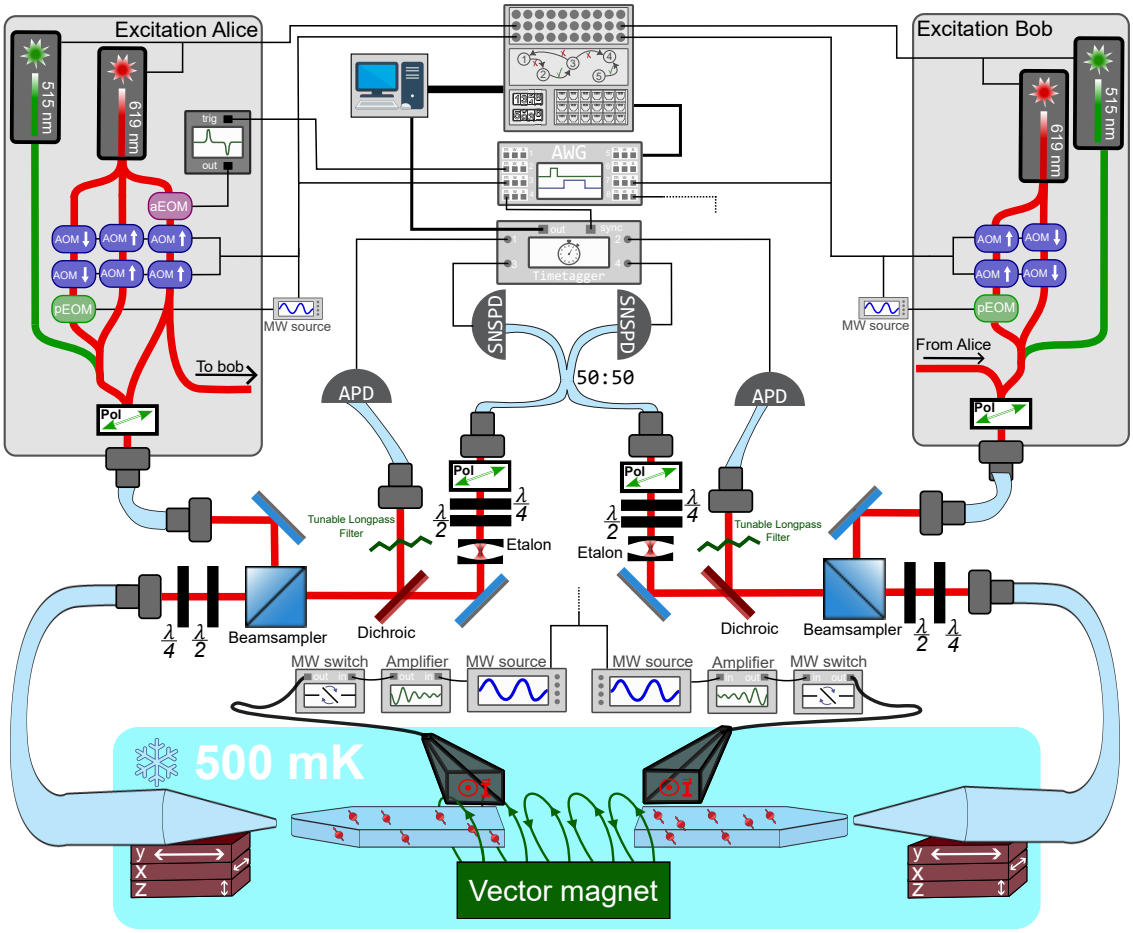

Figure 3.1: Schematic representation of the optical and electronic hardware components that are present in the setup. Black lines are used to indicate electrical cables, while red and green thick lines represent optical paths. All optical paths are free-space, except for the AOMs and EOMs, which are in-fiber (except for the two AOMs in the shared pulse path).

Excitation optics

For meeting the requirements in terms of the excitation optics, the setup features 4 lasers. Two of these are Cobolt 06-01 [90] diode lasers at a the repump wavelength of 515 nm. The rise time of these lasers (<2.5 ns) is much smaller than the required temporal resolution for repumping (~10 µs), meaning that they can directly be turned on and off by the control electronics. The other two lasers are TOPTICA SHG-TA620 tunable frequency-doubled diode lasers [91]. Each of these lasers is roughly tuned to a wavelength of 619 nm, from where the frequency can be fine-tuned with a piezo-controller of one of its cavity mirrors with a spectral stability of 100-300 kHz. As previously stated though, the experimental realization of entanglement schemes requires multiple resonant excitation paths at different wavelengths for each subsetup: two for >10 µs excitation pulses on resonance with both spin-conserving transitions and one for ~1 ns excitation pulses on resonance with one of these transitions. The schematics in Figure 3.1 labeled as "Excitation Alice" and "Excitation Bob" show the hardware components that are used to experimentally achieve this.

Firstly, the path for the short (~1 ns) optical pulses is the only asymmetric optical path of the entire setup. Due to hardware availability restrictions, the setup features a single path for the creation of such pulses (located on Alice's side). This path is split up among both subsetups after the control electronics that create the optical pulses (see Section 3.5). A single shared pulse source suffices for entanglement generation experiments, in which the emitters in both subsetups are tuned to share a wavelength of one of their spin-conserving transitions (see Section 7.1). The exact way in which the hardware is used to create short optical pulses is described in Section 3.5.

Generally, each resonant laser path passes through two Acousto-Optical Modulators (AOM) [92], which use acoustic waves to create a Bragg refraction pattern in space. Only the first order (either +1 or -1) of the spatially separated Bragg refraction pattern is transmitted. The modes in this Bragg refraction have a frequency shift of 200 MHz between them, meaning that such an AOM can either shift the incoming frequency 200 MHz upwards (if it selects the +1 mode) or downwards (if it selects the -1 mode). Figure 3.1 depicts both types of AOMS with arrows indicating either an up- or downshift. Combining the strategic use of these different AOM species combined with an Electro-Optical phase Modulator (pEOM) [93] in one of the paths on both subsetups gives the setup the capability of resonantly exciting four separate transitions independently. In experiments, the laser powers are calibrated by measuring the optical power in free-space (right before the collimator of the fiber going into the cryostat) for different amplitudes of the RF voltage that is supplied to the AOMs. From this, the relation between the AOM opening voltage and optical power in the fiber going into the cryostat is known, which is leveraged to establish fully independent control over the laser power in each of the optical paths.

After modulation and shaping of the optical pulses with the combinations of AOMs and EOMs, it is important to effectively deliver them to the waveguide. Figure 3.1 shows the way in which the paths are first combined in each subsetup separately. After this, the optical path is directed to the pure-silica fibers [94] that go into the cryostat on both subsetups through a Beamsampler [95]. The half- and quarter-waveplate before the collimation into the fiber going into the cryostat are used to optimize the polarization of the excitation pulses with respect to the dipole moment of the targeted emitter (see Appendix A.2). Simultaneously, these waveplates also function to inverse the polarization of collected photons, thereby optimizing the transmission of the beamsampler for collection. Finally, by correctly coupling the tip of the tapered fiber to a waveguide (see Section 3.3), the excitation light from all optical paths can reach the location of tin-vacancy centers within waveguides.

Collection optics

Next to the ability to excite the defects in the waveguide, it is crucial to collect the emitted photons from these defects. In this setup, the collection and excitation is done through the same fiber in the cryostat, meaning that about 50% of the emitted photons is always lost from the directionality. Crucially, the collected photons are filtered into two optical paths by a dichroic mirror, which has a cut-off wavelength at 625 nm [96], roughly corresponding to the start of the PSB spectrum [75]. In the PSB path, a Tunable Longpass Filter [97] is used to completely filter out all laser reflections. After this, the photons are collimated into a multi-mode fiber, which routes them to an Avalanche PhotoDetector (APD), providing accurate photon detection at the 1 ns timescale with an estimated efficiency of ~ 70 % [98].

In the ZPL collection path, it is crucial to filter out the D-transition, since the photons from that transition can not be used for entanglement generation (see Section 2.1.3). This filtering is achieved by a custom-made etalon cavity [99] with a bandwidth of ~40 GHz, which yield a ~30 dB suppression of the D-transition. After this filtering, a combination of a half-waveplate, quarter-waveplate and polarizer are used for the cross-polarization filtering of laser reflections, as described in Section 3.6. Finally, the ZPL photons on both subsetups are collimated into the two single-mode (polarization maintaining) fibers that form the input ports of a 50:50 in-fiber beam splitter [100]. The output ports of this beam splitter are connected to two identical Superconducting Nanowire Photon-Detectors (SNSPDs) [101] through ~20 m of optical fiber. The SNSPD detectors are able to give accurate photon counts on a timescale of several tens of picoseconds with estimated efficiencies of ~95 %.

3.1.2. Cryogenics

As presented in Section 2.3, it is crucial for entanglement experiments that the quantum state of the defect is preserved during the entanglement generation attempt. To achieve this, phonon-induced transitions have to be mitigated, for which low-temperatures are required. For the tin-vacancy center, the required temperature to preserve the spin state is about 1.7 K [46, 102]. In the setup of this work, a ^{3}He/^{4}He cooled Bluefors LD250HE cryostat [103] is used to reach cryogenic temperatures. This system can either be operated at 4K with ^{4}He cooling only, or at 500 mK when the ^{4}He cooling is combined with ^{3}He circulation. Moreover, the high cooling power (2 W at 4 K, 20 mW at 0.7 K) enables the transmission of relatively high-power microwave pulses without significant heating effects. The axis of the cold plates contain a 4f lens system, through which imaging of the sample and tapered fiber is realized (see Appendix C.1).

As illustrated in Figure 3.1, the setup is equipped with a superconducting coil vector magnet [104], which is attached to the bottom of the coldest stage. The vector magnet gives complete control of the static magnetic field orientation at the sample for magnetic field strengths below 1 T. This static magnetic field is required for experiments involving MW driving of the spin-split transition. This MW driving is realized with fluctuating currents through a metallic bond-wire, which is positioned 50 − 100 µm above the waveguide and connected to electronics outside of the cryostat (see Section 3.2). The external electronics that are used for the experiments consist of a combination of a microwave source, fast switch and amplifier. The MW sources of both subsetups [105] produce low-power high-fidelity square pulses, which are actively amplified by 46 dB (36 dB) on Alice's (Bob's) side by a MW amplifier [106] ([107]). A MW switch is used to prevent leakage of currents into the cryostat during experiments at times where no spin-control is needed in order to minimize unwanted heating effects. Finally, for both of the subsetups the tapered fiber is supported by a stack of three nanopositioners [108, 109], which are used to optimize the coupling between the fiber and waveguide with a µm resolution in all three cartesian coordinates (see Section 3.3).

3.1.3. Control electronics

It is crucial in experiments to have precise control over components such as AOMs, motorized waveplates, EOMs, laser frequencies, etc. Because of this, a well-designed control electronic infrastructure is key for execution and repeatability of experiments. The central component for electronic control during experiments is an ADwin-Pro II microcontroller unit [110]. This unit features programmable state machines running on a 1 µs clock cycle, Digital-to-Analog Conversion modules, Count modules and an ethernet interface. All electronically controllable components in the setup are either controlled by the ADwin or by the Arbitrary Waveform Generator (HDAWG) [111], which in turn is triggered by the ADwin. The HDAWG has a 416 ps clock cycle, making it useful in experiments with operations at a higher resolution that the 1 µs ADwin clock cycle. The detection events are recorded by the count modules on the ADwin and by a timetagger [112]. This timetagger is utilized in a histogram mode, in which it bins the arrival times of incoming electrical signals originating from detection events with an 80 ps resolution. Communication to the ADwin is done through a python-based measurement environment, which runs locally on a Linux PC.

3.2. The diamond sample

The most critical component of the setup is the diamond sample that contains the tin-vacancy centers. All of the results presented in this work are obtained from the same sample. The sample is made from a 4mm x 4mm x 0.5mm Chemical Vapour Deposition grown ⟨100⟩ non-purified diamond. This diamond sample is implanted with ^{120}Sn ions, at an implantation dose of $1 \cdot 10^{11}$ ions/cm^2. The implantation is done by accelarating the tin-ions into the diamond with a kinetic energy of 350 keV, from which it is expected that the ions are located within a 32nm vertical straggle centered around 88nm below the top surface [54].

After implantation, the diamonds are cleaned and annealed at high temperatures. The annealing of implanted samples simultaneously heals the damage in the lattice structure from the implantation and mobilizes lattice vacancies, ultimately allowing them to pair up with implanted tin ions to form a tin-vacancy configuration. After the annealing step, the sample holds many optically active defects. For better optical adressability, the diamond containing the defects can be removed in a specific pattern to improve collection of emitted photons. In this work, that specific pattern consists of suspended waveguides. These waveguides are fabricated in a 14-step process, involving several masking and etching steps (the details of which can be found in [54]). The waveguides have a tapered design on the end facing the collection fiber to optimize coupling of the waveguide mode to the collection fiber. The rectangular waveguides have widths of 240-280 nm and heights around 150 nm and are oriented along the ⟨110⟩ crystallographic axis of the diamond lattice.

The sample is mounted into the setup by gluing it to a Printed Circuit Board (PCB), on which four SMA input-output ports are fabricated. After gluing, two metal wires are drawn ~50-100 µm above the waveguides and attached to two of these input-output ports each. In this way, the input-output ports of the PCB form two separate transmission lines, enabling electrical currents to flow close to the sample, which are used for generating fluctuating magnetic driving fields.

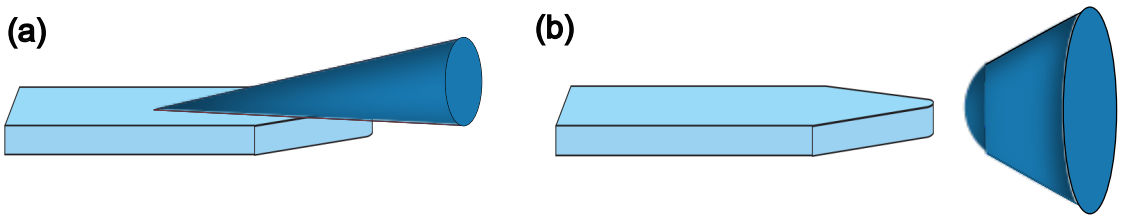

Figure 3.2: Schematic overview of two types of fiber-waveguide coupling mechanisms. (a) The "contact-coupled"-scheme, in which a tapered fiber is put in contact with a tapered waveguide, which allows the evanescent field from the waveguide to couple into the mode of the tapered fiber adiabatically. (b) The "lensed-coupled"-scheme, in which the tip of a single-mode fiber is fabricated in the shape of a lensed semisphere, which leads to a cone-like field density in the air between the waveguide and fiber.

3.3. Fiber-waveguide coupling mechanisms

Both for the photon collection and the excitation of the tin-vacancy centers in waveguides, it is crucial to have high coupling between the optical mode in the waveguide and the mode in the tapered fiber. Two categories of coupling mechanisms can generally be distinguished in literature: Those that require physical contact between the fiber and waveguide and those that don't [55, 113–116].

Generally speaking, methods that involve a form of *contact-coupling* have proven efficiencies above 90 %, making them highly efficient for photon collection [113]. The general configuration for these schemes is depicted in Figure 3.2a. The figure shows the configuration of a diamond waveguide, which has a tapered width on one end. On this end, a tapered cone-like fiber is mounted on top of the waveguide. The combination of the specific taper parameters of both these components are instrumental for good coupling efficiencies [55]. Without going into the details of simulating the Maxwell equations for such a configuration (see [55]), the working principle can be described through the evanescent field of the waveguide. The combination of tapers is maximized for the overlap between this evanescent radiation field and the mode in the fiber.

The second approach (illustrated in Figure 3.2b) is realized through a different configuration, referred to as *lensed-coupling*. In this configuration the tapered fiber is replaced by a fiber whose tip has been fabricated (often using a Focused Ion Beam) to be a semi-sphere. This lens-like structure of the fiber tip has leads to overlap between its cone-like emission field and the evanescent waveguide field [115, 116]. The collection efficiencies that have been achieved with this methodology are however much lower than the contact-coupled scheme.

Having illustrated the two main approaches in literature, it becomes clear that the contact-coupled configuration would be more suitable for stable entanglement experiments. Because of this, the setup is equipped with two tapered fibers (as schematically drawn in Figure 3.1). In experimental attempts to achieve coupling, the positioner stacks below the fibers are used together with the imaging optics from the top to land the fiber on a waveguide. When the fiber tip gets into close vicinity of the waveguide, the van der Waals forces "snap" it in contact. This expected behavior could be replicated, but unfortunately the coherence of the optical transitions of the emitters was lost because of it. The effect of a loss in coherences was measured as an extreme broadening of the linewidths during photoluminescence experiments, which is attributed to the fluctuating strain environment that is induced by vibrations of the (dangling) fiber, or heating induced by a possible temperature difference between the fiber and waveguide. These issues could not be resolved with the current setup, which is why a third coupling scheme was used. Instead of a properly designed lensed fiber tip, the experiments in this work are done with the a tapered fiber, which is positioned in the lensed configuration. Without having simulations on this configuration, it can already be concluded that the coupling of the waveguide mode to the fiber is therefore not optimized. Figuring out the isolated efficiency of the fiber-waveguide interface is however impossible in the current configuration of the setup, since transmission experiments are not possible. Instead, Section 4.3 will present an estimate on the combined losses throughout the entire optical collection path. It should also be noted that efficient fiber-waveguide coupling is an active area of research. One method that can lead to an improvement in the coupling is to realize the contact-coupled configuration by gluing the fiber to a surface close to the tip [117]. This approach might reduce mechanical vibrations of the fiber tip and can in general improve the stability of the configuration.

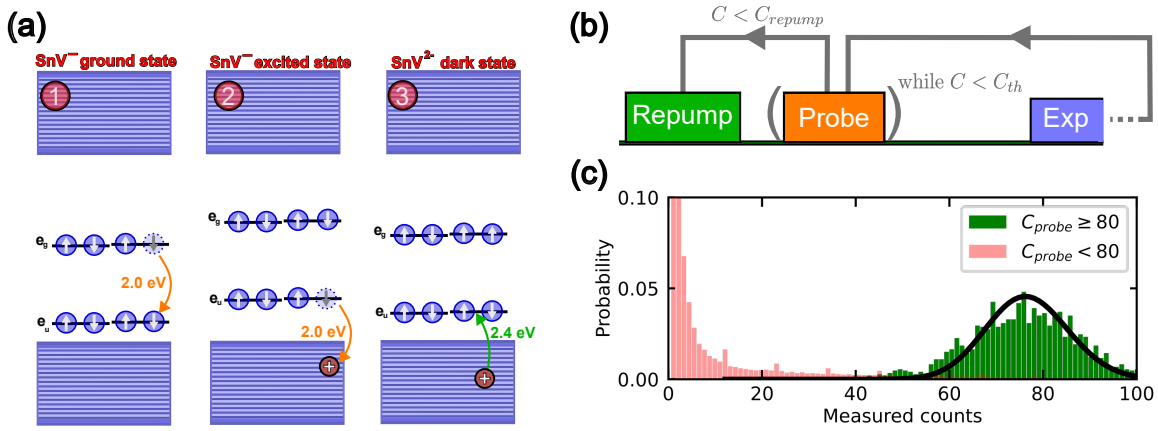

Figure 3.3: Charge dynamics of the tin-vacancy center during resonant and off-resonant excitation. (a) A schematic representation of the tin-vacancy energy levels in the diamond band gap for three situations: (i) The tin-vacancy center is in the ground state and is excited by a 2.0 eV resonant optical excitation, (ii) The tin-vacancy center has a hole in the excited state, which gets excited into the valance band due to a persisting 2.0 eV excitation and (iii) the tin-vacancy is in the dark SnV^{2-} state and an off-resonant excitation is used to excite a hole from the valence band into the tin-vacancy hole excited state levels. These charge dynamics are based on experimental work in [62] (b) A circuit diagram for the Charge-Resonance check (CR-check) that is used in most experiments of Chapters 4-7. The circuit diagram is derived from methodology presented in [57]. (c) A histogram of the counts measured during the second probe pulse of a CR-check experiment with two probe pulses. The histogram is separated into occurrences of measured counts from the second pulse when the number of measured counts in the first pulse were either above or below a threshold of 80. The histogram of the counts where this threshold was passed in the first pulse is fitted with a Poissonian distribution with a mean photon number of $\bar{n} = 76.7 \pm 0.3$.

3.4. (Semi-)deterministic Charge Resonance Control

An essential capability in the setup is the control of the charge-induced resonance of the measured tin-vacancy centers. This capability was first demonstrated for the tin-vacancy center in [57] and the methodology here is derived from that work. In general, we consider two ways of getting tin-vacancy centers in a bright charge state: *repumping* and *Charge-Resonance checks* (or *CR-checks*). This section will explore both methodologies and highlight crucial differences between the two. The differences between these methodologies is mainly discussed in the consequences for the design of experimental sequences for the realization of TPQI or entanglement experiments.

Figure 3.3a shows the energy diagram of the localized tin-vacancy energy states within the diamond bandgap for three different situations. Panel 1 shows how a 2.0 eV (~619 nm) photon can excite the tin-vacancy ground state to the excited state. Panel 2 then shows how another excitation event with a similar photon can excite the hole from the excited state into the valance band, thereby putting the tin-vacancy center in the dark SnV^{2-} configuration and generating a hole in the valence band. Concretely this means that when a tin-vacancy center is continuously excited with a resonant laser, the emitter will go "dark" after some time [62]. The exact time after which this happens is highly dependent on many parameters such as the availability of electron charges in the local valance band, the exact absolute position of the emitter's energy levels within the bandgap, the excited state lifetime and many more. Experimentally, it has been shown that this time is often on the scale of a few µs for the tin-vacancy center, making it highly relevant for many-photon experiments (as presented in Chapters 4 & 5). To overcome this limiting behavior, a manipulation of the system needs to be introduced that can allow the tin-vacancy to capture a hole in one of its energy states, thereby relaxing back into the bright SnV^{-} state. To achieve this, an optical excitation needs to be used with a sufficiently low wavelength to bridge the gap between the valence band and hole excited states of the tin-vacancy (as illustrated in Panel 3 of Figure 3.3). This optical excitation is done in this work through a 2.4 eV (515 nm; green) laser and is referred to as *repumping*.

The repumping mechanism is quite effective for regaining a bright charge state of the tin-vacancy center, but does come at a cost. The high-energy pulse also excites energy levels of charge traps near the defect. Because of this, it is quite likely that the charge environment of the tin-vacancy is completely different after such a repump pulse. A change in the charge environment translates directly into a change of the transition frequency of the tin-vacancy center through the Stark effect [118]. Because of this, the repump pulse is often seen as a quasi-random reset pulse of the charge-induced resonance frequency of the emitter, thereby adding to the amount of spectral diffusion in the system. However, as theoretically shown in Section 2.2.2, this spectral diffusion is detrimental for the indistinguishability of the photons produced by the tin-vacancy center. Because of this, it is essential to establish a method of deterministically resetting the charge-induced resonance of the tin-vacancy center to a fixed value.

The technique that is used to this end is presented as a circuit diagram in Figure 3.3b. The main idea is to include a real-time probe of the charge-induced resonance after each repump pulse. Repetitions of an experiment are then only started if the probing measurement determines that the charge resonance of the emitter is within the accepted range. The probing measurement simply consists of a single resonant pulse (of $\sim 50-100$ μs), during which the number of photons (as detected by the APD in the PSB collection path) is counted. If the number of measured photons surpasses some configurable threshold value (C_{th}), then a single repetition of an experiment is performed. If the measured number of photons is however below the threshold value, then it is concluded that the resonance of the tin-vacancy center is not sufficiently close to the resonance frequency of the probing signal. If that is the case, then the probing pulse is repeated in an effort to sufficiently alter the charge environment to get the emitter back on resonance. If however the counts during the probing pulse fall below some second (lower) threshold (C_{repump}), then it is concluded that the tin-vacancy has gone into a dark state, which means that the sequence has to start over again with the repumping step. In typical experiments, each CR-check sequence takes $\sim 100-300$ μs.

The effectiveness of the threshold can be characterized by a measurement of the number of detected photons during a second repetition of the probe pulse (thereby making a second "probe" the "experiment" of Figure 3.3b). A correlation of the measured counts in the first pulse and second pulse would indicate the effectiveness of a threshold. This correlation is explored in the histogram of the number of measured counts during the second probe pulse as shown in Figure 3.3c. The histogram of the number of measured photons in the second pulse is separated here into instances where the number of measured counts during the first probe pulse is either greater or smaller than a threshold of 80 counts. The figure clearly shows the consequence of the charge state of the emitter when setting such a threshold. The instances where the threshold was surpassed are always measured in a bright state (as concluded from the fact that the green zero bin is non-existent), with a high mean-photon number ($\bar{n}_{\text{bright}} = 76.7 \pm 0.3$) as measured from the Poissonian fit. If the threshold is not met in the first pulse, then the emitter is most-often found in a dark state ($\bar{n}_{\text{dark}} = 1.01 \pm 0.07$).

It should be noted that the relation between the CR-threshold and spectral diffusion magnitude is not known. Efforts have been made to explore this relation both theoretically and experimentally [119], but it is not immediately obvious how to translate these efforts to the configuration in this work. Because of this, the CR-check method is considered here as a quasi-deterministic reset of the charge environment of the tin-vacancy center.

3.5. Short optical pulses

A central capability for the entanglement scheme as presented in Section 2.3 is the optical π-pulse. The goal of such a pulse is to achieve a complete π-rotation on the Bloch sphere between one of the ground states and one of the excited states. Given the difficulty of driving spin-flipping transitions (as derived in Section 2.1.3), the combinations of ground- and excited states that are considered here each have a spin-conserving transition between them. The selectiveness in terms of the spin-conserving transitions is obtained through the wavelength of the excitation laser.

The excited state lifetime of the tin-vacancy center has been experimentally measured to be around $5-7$ ns, depending on the photonic environment around the defect [50, 51, 54, 75]. In order to achieve fully coherent population transfer from the ground to the excited state, it is thus important to minimize the probability of spontaneous decay events during the excitation pulse. Concretely, this means that the excitation should be done within a fraction of the lifetime to obtain double excitation probabilities on the few percent level [120].

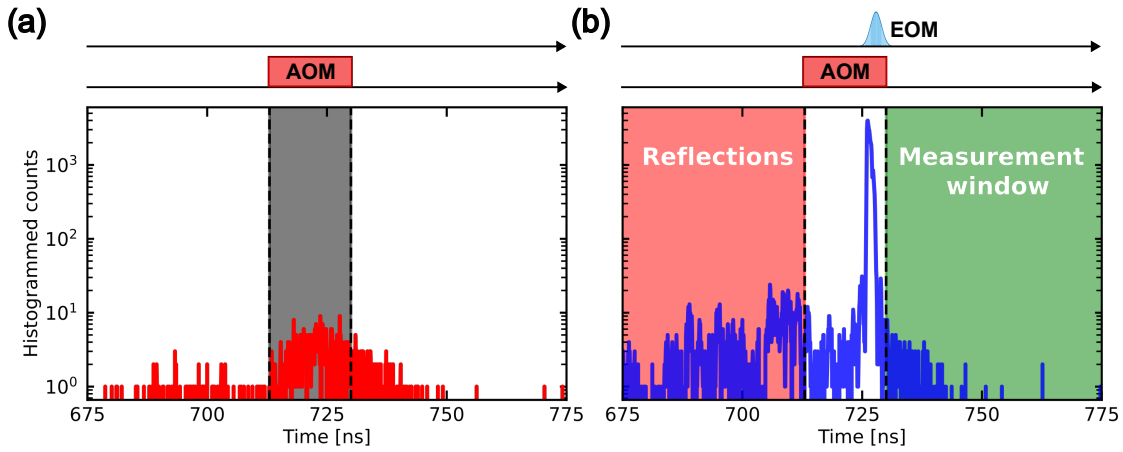

Figure 3.4: Measurements of pulse-shape calibrations. (a) The measured reflections of the fiber-tip in the ZPL collection path, histogrammed in 80 ps time-bins. The low "blob" indicates the opening of the AOM in the pulse path. (b) The same measurement as in (a), but now with a calibrated 1.5 ns opening of the EOM during the AOM opening. The figure shows increased counts before the AOM opening from (a), which are attributed to reflections (red shaded area). The measured detection events after the drop-off of the pulse (green shaded area) are the only ones considered during experiments.

The experimental realization of short, high-power Gaussian optical pulses is quite challenging. The required hardware components for creating the pulses in this setup can be found in Figure 3.1. The optical path where the pulse is created features two critical components: An Amplitude Electro-Optic Modulator (aEOM) and an Acousto-Optic Modulator (AOM; which is double-passed and hence drawn twice in the optical path). The AOM can be opened and closed with risetimes in the order of tens of nanoseconds. It has the advantage however that no optical power is transmitted once it is switched off (because it physically alters the beam path). The AOM is used to create a relatively long flat opening, during which the EOM is used to create a very short pulse. The opening of the AOM is calibrated to be 50ns (supplied by the HDAWG) and is measured in Figure 3.4a, where a histogram of the resonant reflections as measured in the ZPL collection path is shown. Next, the EOM is triggered with a short Gaussian electrical signal (as created by an in-house fabricated "pulse box"), which changes the phase difference between the arms of a Mach-Zehnder interferometer (inside the EOM) to create a short period of local constructive interference, causing a high optical intensity pulse. The measurement of this pulse (in the same way as for the AOM opening) can be found in Figure 3.4b. Next to the clear peak in observed detection events at the pulse location, the detection also features many bins with increased counts before the pulse. This noisy pattern is attributed to reflections, most-likely originating from components in the optical excitation path before the fiber that goes into the cryostat.

The configuration of a long AOM and short EOM pulse allows for a complete calibration of an optical π-pulse. The supplied peak voltage to the EOM can be calibrated to maximize its opening. Then, the RF driving power of the AOM is used to calibrate the fraction of the power that is transmitted through it. In this way, the exact optical power that is required for a π-rotation can be supplied, as will experimentally be demonstrated in Section 6.1. In this work, optical π-pulses are 1.5 ns long. The timing of this pulse with respect to the AOM opening is always calibrated to minimize the opening of the AOM/EOM combination in the measurement window. Typically, this is best done by placing the EOM pulse on the slope during which the AOM closes.

3.6. Resonant laser filtering

In experiments involving resonant excitation of tin-vacancy centers, the photons emitted into the ZPL have exactly the same frequency as the excitation laser. This effectively means that reflected laser photons will follow the exact same optical path as the collected ZPL photons from the emitter. Typically, the amount of reflected photons from the high-intensity laser pulses completely overshadow the few ZPL photons from the emitter, making their detection impossible without additional filtering. Since the reflected laser photons and ZPL photons from the emitter are indistinguishable in frequency, there is no way to do this filtering spectrally. Instead, the other two degrees of freedom of the emitted photons are used: time and polarization.

Firstly, the polarization degree of freedom can be utilized for distinguishing between laser reflections and photons emitted from a defect by a combination of a half-waveplate, quarter-waveplate and polarizer in the ZPL collection path (as presented in Figure 3.1). The main idea is to fully suppress the reflections from the laser by always aligning the polarizer to be perfectly perpendicular to the polarization of the reflections. Then, the polarization of the excitation laser is aligned to be exactly linear with an angle α compared to the dipole moment of the tin-vacancy center (within the polarization basis defined by the waveguide modes). The ZPL photons emitted by the tin-vacancy center will have the polarization belonging to the dipole orientation of their source, meaning that there is an angle α between the polarizations of the emitted photons and the laser reflections. By this logic, a polarizer that is perfectly perpendicular to the polarization of the laser reflections should have a transmission factor of $\cos^2\left(\frac{\pi}{2}-\alpha\right)$ for the ZPL photons. In this work, an angle of $\alpha = \frac{\pi}{4}$ is always used, leading to a transmission of 50 % of the photons. Increasing the angle would improve the collection efficiency, but would increase the required power for excitation. In a scenario with enough excitation power in the setup, higher angles α are generally favored. More details on the validation of this scheme with comparisons between experimental data and theoretical modeling can be found in Appendix A.2.

It should still be noted that perfect extinction of laser reflections with this scheme is experimentally not achievable. Despite careful calibration of the cross-polarization filtering, laser reflections still prove to be the main source of noise in the measurement results of Chapters 6 & 7. The imperfect extinction of reflected laser light with cross-polarization is attributed to fast polarization fluctuations in the setup. The influence of this noise source can still be further mitigated by filtering on the second degree of freedom: time. Figure 3.4b showed a time-binned histogram of detection events on the ZPL detectors. The large peak in events corresponds to the shape of the excitation pulse that is used. Time-filtering can be done by only considering detection events after the extinction of this pulse (as indicated by the green region). Careful selection of the boundaries of the measurement window allows for another suppression of noise sources and will be explored in further detail in Chapters 6 & 7.

4

Characterization of the optical manifold of the tin-vacancy center

The optical manifold of a tin-vacancy center consists of many transitions, as highlighted in Section 2.1. This chapter will focus on experimental results that can be used to support the theoretical framework described there, while also yielding quantitative estimates of the quality of the tin-vacancy centers in the fabricated sample and the setup. These results are crucial for developing an understanding of the characteristics of the optical transitions, tailored towards the specifics of the experimental setup. The chapter will start by discussing measurements on ensembles of tin-vacancy centers in a single waveguide and will work towards a full characterization of the optical manifold of a single tin-vacancy center at non-zero magnetic fields.

4.1. Spectrally measured tin-vacancy centers in waveguides

As discussed in Section 2.1.2, the optical transitions of the tin-vacancy centers are heavily dependent on (among others) their strain environment. Given the complicated nature and relative novelty of the fabrication process of tin-implanted diamond waveguides [52, 54, 121], the exact wavelength of the C and D transitions of these emitters is not known a priori. Moreover, the implantation of these defects is an inherently non-deterministic process, which means that exact statistics on the number and spectral density of bright emitters (i.e. emitters with sufficient coupling to the optical mode of the waveguide) within a fabricated waveguide are unknown. Since the setup does not feature a tuning mechanism for the resonances of emitters, an entanglement experiment can only be done with two emitters that happen to have spectrally close resonances. For estimating the probability of finding two such emitters, it is essential to gather statistics on the amount of usable tin-vacancy centers per waveguide.

To experimentally observe the presence of bright emitters in a single waveguide, it is advantageous to excite as many emitters simultaneously as possible and analyze the spectral decomposition of the collected emission light. Exciting multiple emitters, each with a slightly different resonance can most effectively be done through optical excitation at a wavelength far-detuned from the resonance. More specifically, a 515 nm (green) "repump" laser is used here to this end. As presented in Section 3.4, a laser at this wavelength has the ability to bring a tin-vacancy center into its bright state, regardless of parameters such as strain. Upon excitation to the excited state, the tin-vacancy decays through spontaneous decay channels, causing emission of photons from all decay channels of all tin-vacancies in a single waveguide. A spectral measurement of the collected light from the waveguide averaged over the 100 s duration of continuous off-resonant excitation can be found in Figure 4.1a. Most notably, the spectrum features prominent peaks near $\lambda_C = 619\,\text{nm}$ and $\lambda_D = 620\,\text{nm}$, which are believed to correspond to the C- and D-transitions of an ensemble of tin-vacancy centers.

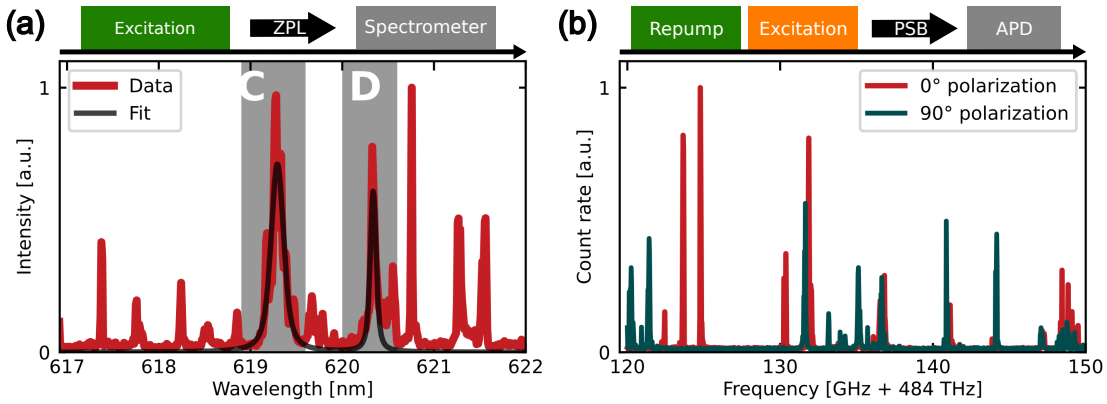

Figure 4.1: Spectral measurements of tin-vacancy centers in a diamond waveguide. (a) A spectrum of the response of a waveguide to 100 s of off-resonant (515 nm) excitation, as observed through the ZPL collection path. The spectrum shows two clearly peaks near the expected C and D transition of the tin-vacancy center. The center of the inhomogeneous distribution of the C-transition is found at (619.293 ± 0.003) nm, which corresponds to a frequency of ~484.101 THz (both reported in vacuum). (b) A Photoluminescence Excitation (PLE) measurement, where a resonant laser is swept over a 30 GHz range of frequencies near the center of the inhomogeneous distribution of the C-transition (as estimated from (a)). The excitation is alternated by periods of green repumping to minimize dark state population. The two differently colored datasets correspond to two orientations of the half-wave plate in the excitation path, which correspond to two orthogonal polarizations of the excitation light in the tapered fiber.

It should be noted that Figure 4.1a features more significant peaks outside of the expected wavelengths of tin-vacancy defects, which are believed to possibly originate from several causes. Fabrication irregularities might cause high fluctuations in the strain environment within the waveguide, causing certain regions to experience different strain then others. A region of very high strain could also explain the emergence of these peaks. Recent work has also shown that a High Pressure High Temperature (HPHT) annealing step in the fabrication process can prevent noisy peaks originating from damage in the lattice near the defect [75, 102]. Lastly, the peaks could also be caused by noise within the detection path. For example, it could be the case that these peaks correspond to optical resonances within the path or fluorescence within the fibers. Additionally, irregularities in the spectral sensitivity or calibration of the spectrometer can cause noisy spectra.

Most importantly for the scope of this work though, the fit of the C-transition in Figure 4.1a gives a clear indication of the center of the inhomogeneous distribution (as estimated from this single waveguide). This center is found to be at $\lambda_C = 619.293 \pm 0.003$ nm, which corresponds to a frequency of ~ 484.101 THz. The knowledge about the central frequency of the inhomogeneous distribution enables experiments involving resonant excitation of the C-transition of individual defects. As a result of the varying charge and strain environments within a waveguide, different emitters will have slightly different optical transitions, which are not distinguishable in the spectral measurement of Figure 4.1a (as they only contribute to the width of the transition peaks). It should be noted that resonant excitation of individual tin-vacancy centers is especially crucial in the fiber-coupled scheme of this setup. The fiber-coupled configuration removes the positional degree of freedom in excitation, which is most often leveraged in other works [37, 50, 122]. Because of this, the tin-vacancy centers in a single waveguide can only be selectively addressed through their spectral distinguishability. To detect and separate the optical transitions of the defects, a PhotoLuminescence Experiment (PLE) is performed. In such a measurement, the frequency of a laser is swept over a range of a few tens of GHz near the center of the inhomogeneous distribution. When the excitation of the laser is on resonance with the transition of a defect in the waveguide, an increase in the optical intensity in the collection path is expected. Since continuous resonant excitation can lead to ionization, a 200 µs period of repumping is alternated with each 150 µs period of resonant excitation (see Section 3.4).

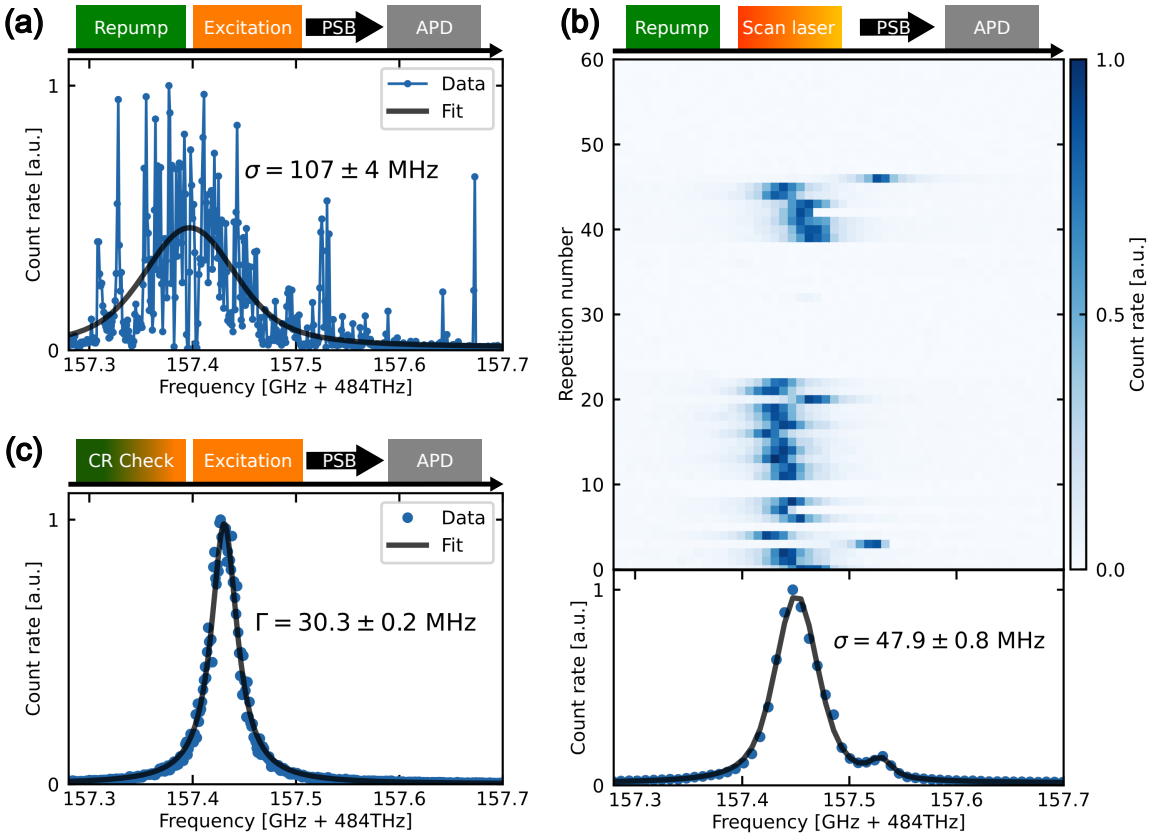

Figure 4.2: Towards a measurement of transform-limited photons from an individual tin-vacancy center. (a) A PLE measurement, centered around the C-transition of a single emitter. The fit is a convolution of a Lorentzian with a Gaussian (also known as a Voigt function), which describes the effect of spectral diffusion. The fit reveals a Full-Width at Half Maximum (FWHM) of $\Gamma = (107 \pm 4)$ MHz. (b) A PLE linescan measurement, where the frequency of a laser is swept over a frequency range of 0.4 GHz within several seconds. The intensity in the PSB collection path is monitored during the scan and plotted for 60 consecutive repetitions of the scan, taking a total of roughly 10 minutes. The data in the lower graph represents the normalized average count rate over all repetitions. The data is fitted to a sum of two Voigt functions, where the most prominent peak has a linewidth of $\Gamma = (47.9 \pm 0.8)$ MHz. (c) A CR-checked PLE measurement, for which each repetition of resonant excitation is executed conditional on the emitter being in a bright state (as probed by a short resonant excitation; see Section 3.4). The data is fitted to a Lorentzian with a linewidth of $\Gamma = (30.3 \pm 0.2)$ MHz.

The result of such a measurement can be seen in Figure 4.1b. Here, the normalized optical intensity in the PSB collection path is plotted against the frequency of the excitation laser. It is common practice to use the collection of the PSB decay channel in such measurements, as this offers a natural way of filtering out overshadowing reflections of the resonant laser. Figure 4.1b shows two measurements, which are taken at two angles of the excitation polarization that differ by exactly 90°. By changing the orientation of the half-wave plate in the excitation path, the polarization of the resonant laser within the waveguide changes. The efficiency of optical excitation depends on the overlap of the electric field of the excitation light and the dipole moment of the emitter (see Appendix A.2). The emitters in the waveguide can have different physical orientations and the polarization of the excitation light is not stable over the length of the waveguide. Therefore, the optimal wave-plate angles are different for each emitter. In order to maximize the visibility of all emitters, the measurement is repeated for two orthogonal polarizations.

Finally, the spatial position of the defect within the waveguide also plays a big role in its relative brightness. The coupling of an emitter to the spatial mode of the waveguide determines the percentage of photons that it emits into the waveguide mode. It has been shown that this percentage is highly dependent on the spatial position of the defect within the waveguide [54]. Ultimately, measurement results such as Figure 4.1b are used as an initial characterization of the number and relative brightness of emitters within a waveguide. To further study their exact properties, more detailed emitter-selective measurements are required.

4.2. Towards transform-limited photons

One of the key ingredients for both entanglement and Two-Photon Quantum Interference (TPQI) is that the optical transitions of the emitters have linewidths that are close to the lifetime limit (see Sections 2.2.2 and 2.3.2). To probe this characteristic for an emitter, it is crucial to have the ability to excite and collect from a single SnV center within a crowded waveguide. An initial attempt to do this is by simply repeating the measurement from Figure 4.1b for a narrow range of resonant frequencies around the optical transition of the specific emitter. Such a measurement can be found in Figure 4.2a, which clearly demonstrates the effect of spectral diffusion as a Gaussian convolution of many (narrower) Lorentzian profiles. The fit in Figure 4.2a reveals that this spectral diffusion causes the optical transition to have a linewidth of $\Gamma = (107 \pm 4)$ MHz, which is far above the expected lifetime-limited linewidth. It is essential to figure out the sources of this broadening and to mitigate their effects to use these emitters for entanglement or TPQI measurements. The most important factor for mitigation of these noise sources is the timescale on which they influence the resonance of the emitter.

Each datapoint in Figure 4.2a is an average over 1000 repetitions, recorded over a few hundred milliseconds. Because of this, the actual time between measurements that are a few MHz apart in frequency can be in the order of seconds to minutes. This means that the variance in the data of Figure 4.2a can have noise contributions which effect the system on similar timescales. Since these timescales are not relevant for any entanglement or TPQI experiment, it would be interesting to probe the spectral diffusion with a smaller temporal resolution. An initial attempt at increasing the temporal resolution of noise scales is to increase the rate at which the laser frequency is scanned. Instead of collecting photons during a long period of excitation at each frequency, we can also continuously sweep the frequency of the laser and measure the resulting time-dependent intensity during this scan. The time-profile can then be linked to the laser frequencies through the scanning rate. Figure 4.2b shows the data that was acquired during such a *PLE linescan* measurement. Each row of the colormap shows the measured count rate in the PSB collection path as a function of the frequency of the excitation laser. The excitation laser is swept over the frequencies in a few seconds, such that consecutive datapoints in a single row are only a few milliseconds apart. Such a scan is repeated for 60 times, over the course of a total of ~10 minutes, where each scan is preceded by a period of repumping. The normalized average over all repetitions is shown and fitted in the lower figure. The results in Figure 4.2b confirms the "slow" nature of most of the spectral diffusion in Figure 4.2a. The individual linescans have a fitted FWHM of (32 ± 3) MHz, which is close to the lifetime-limited linewidth. It should however be noted that Figure 4.2b also highlights the significant spectral instability of the emitter on the slower timescale of consecutive repetitions. This spectral instability manifests itself both as shifts in the resonance frequency, leading to a broadening of the averaged intensity (the plot below the colourmap), but also as periods of bright and dark states. These "dark" periods (repetitions 23-38 and 46-60), where no spectral peak is measured, are attributed to ionization of the emitter before the scan reaches the resonance or unsuccessful repumping. Spectral instability at this rate can mostly be explained by the occupation and relaxation of long-lived charge traps near the emitter [58]. The repump pulse that is applied before each repetition attempts to reset the charge environment to a pseudo-random state, but is not deterministic in origin (see Section 3.4).

For TPQI and entanglement experiments, it is important to guarantee that the charge-induced resonance of the emitter is the same for each repetition of the experiment. To probe the charge-resonance (CR) of the emitter, a "CR-check" is added to the PLE measurement of Figure 4.2a (see Section 3.4). The CR-check guarantees that the resonance frequency of the emitter is within a certain range of frequencies, whose size is dependent on the exact threshold of the CR-condition. By restricting the passing threshold, this range of frequencies can be narrowed down. For entanglement and TPQI experiments, it is crucial to know to what extent this CR-condition can reduce the spectral diffusion of an emitter. To probe this, another PLE measurement of the emitter is done, but now with a conditional CR-check replacing the repump step. Figure 4.2c shows the results of this measurement. The difference between Figures 4.2a and 4.2c clearly shows the influence of conditioning the measurement on the charge state of the emitter. To quantitatively prove this, the peak in Figure 4.2c is fitted to a Lorentzian distribution, which gives a linewidth of $\Gamma = (30.3 \pm 0.2)$ MHz. If this were the lifetime-limited linewidth, it would correspond to a lifetime of $\tau = (5.25 \pm 0.03)$ ns. This lifetime is slightly lower than the ones reported in literature [50, 54] and also than the ones observed in experiments later in this work. This means that the linewidth of the CR checked PLE is most-likely still somewhat broader than the lifetime-limited linewidth, but not far from it.

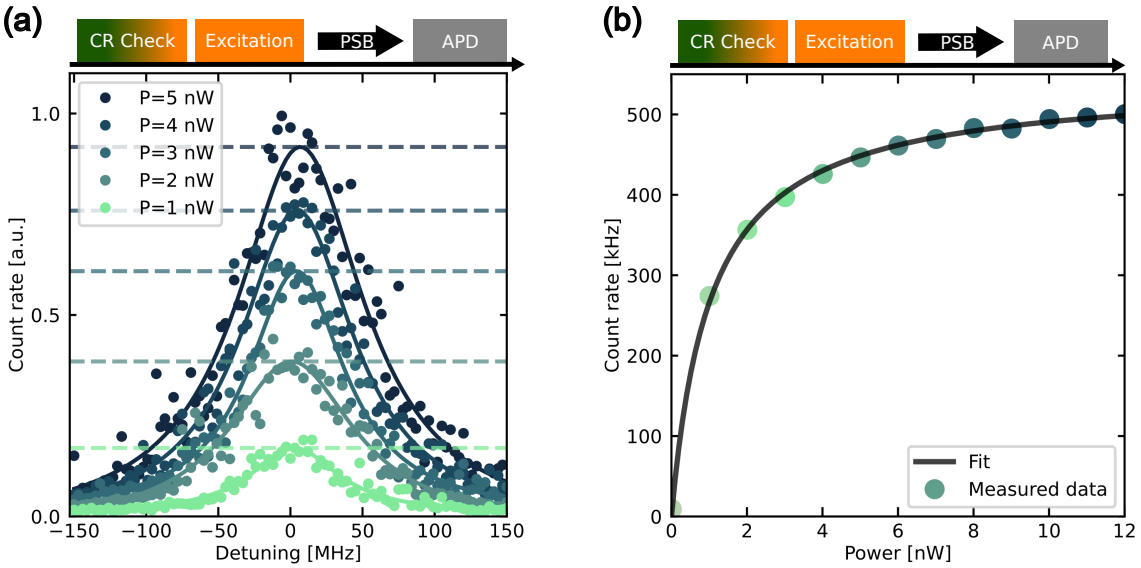

Figure 4.3: Saturation of spontaneous decay in the optical transition of a tin-vacancy center. (a) An ensemble of CR-checked PLE measurements on the same tin-vacancy center, where the power of the resonant excitation is varied between 1 and 5 nW. The measurements are each fitted to Lorentzian distributions and show a clear relation between the excitation power and the peak height. (b) A saturation curve, which is measured in the same way as (a), but now only for the 0 detuning case. The datapoints are fitted with Equation 2.17, which reveals a saturation power of (2.07 ± 0.05) nW. The count rate at saturation power can be used to estimate a collection efficiency of (2.2 ± 0.2) %.

4.3. Driving and collection efficiency

In order to predict the performance of the setup for more advanced experiments, it is crucial to have accurate estimates of the optical efficiency of the setup, both in terms of excitation of the optical transitions and collection of the emitted photons. One way of estimating this is by measuring the saturation of the two-level system of a single emitter. Such a measurement would also establish a reference for the amount of optical power that is needed to drive the transition. The working principle to measure this saturation is demonstrated in Figure 4.3a. Each measurement in Figure 4.3a is a CR-checked PLE (such as Figure 4.2c) with a different excitation power. Clearly, the height of the peak count rate depends on the inputted power. However, as elaborated in Section 2.1.3, the relation between the height of the response and inputted power is not linear. Rather, the response turns out to saturate after a certain characteristic input power: the *saturation power*. The saturation power can be found by recording the height of the count rate in the PSB collection path at a range of excitation powers, such as in Figure 4.3b. By fitting the data to Equation 2.17, a saturation power of (2.07 ± 0.05) nW is found. The exact value of this parameter is highly dependent on many parameters such as: the alignment of the excitation into the fiber going into the cryostat, the fiber-waveguide coupling, excitation polarization, emitter-waveguide coupling, etc. Since the value of the saturation power encapsulates all these setup-dependent parameters, the excitation power in units of the saturation power becomes a very good parameter to compare results from different setup configurations or to compare results from different emitters within the same setup. It should be noted that the value of the saturation power depends on the alignment of the polarization of the excitation to the dipole moment of the emitter. In this work, the value of the saturation power is always reported at a polarization that is aligned to the dipole moment of the emitter (see Appendix A.2).

The saturation measurement can additionally be used to estimate the collection efficiency of the PSB collection path. From Equation 2.17, one can see that the average population of the excited state at saturation power is exactly $\frac{1}{3}$. The collected photons originate from spontaneous decay events, which happen at an average rate that is equal to the reciprocal of the excited state lifetime τ. Combined with the Debye-Weller (DW) and Quantum Efficiency (QE), the predicted rate of decay events in the PSB can be written as

$$\gamma_{\text{spont}}^{\text{PSB}} = \frac{1}{3} \cdot QE \cdot (1 - DW) \cdot \frac{1}{\tau}. \tag{4.1}$$

With an estimated Quantum Efficiency of 0.8 [51], Debye-Weller factor of 0.57 [53] and lifetime of (7.0 ± 0.5) ns (as substantiated in Section 6.1), this predicted emission rate can be found to be $\gamma_{\text{spont}}^{\text{PSB}} = (16 \pm 1)$ MHz. From Figure 4.3b, the actual measured saturation count rate is found to be (361 ± 3) kHz. From this, the percentage of PSB photons that is detected by the PSB detector is estimated to be: (2.2 ± 0.2) %. This value will be referred to in the rest of this thesis as the *collection efficiency*. It should however be noted that this number is subject to a set of known losses throughout the system. The main contribution in unknown losses come from the emitter-waveguide coupling, fiber-waveguide coupling and free-space optical alignment. Compensating for all other known losses in the setup (see Appendix A.1) reveals that these three unknown factors combine to a total photon collection of ~4%.

4.4. The optical manifold at non-zero magnetic field

The tin-vacancy center only becomes useful as a quantum node in a Quantum Network if it has a computational basis of qubit states. For the tin-vacancy center, the most natural choice of such states are the two spin states of the lower branch of the ground state. These states can become non-degenerate under the influence of an external magnetic field, due to Zeeman splitting of the two spin eigenstates (see Section 2.1.2). This Zeeman splitting occurs for both the ground states as well as the excited states. The splitting magnitude of the orthogonal spin states in both the ground- and excited state is highly dependent on both the magnitude and direction of the external magnetic field, as well as the strain (see Section 2.1.3). Since the splitting is asymmetric with respect to the ground- and excited state, the single optical transition gets split into four resonances. Two of these transitions (somewhat) preserve the spin direction and are therefore more easily cycled through optical excitation.

Figure 4.4a shows the detection of the two spin-preserving transitions for an ensemble of magnetic field orientations. Each row in the figure is an average of 10 PLE linescan experiments at a certain magnetic field angle. The two figures are taken at a different azimuthal angle $\phi \in \{0°, 45°\}$ of the magnetic field, while the polar angle θ is swept within each figure. The magnitude of the magnetic field is kept at 100 mT for all orientations. In the lab frame, the azimuthal angle ϕ is zero when the magnetic field is perpendicular to the waveguides, while the polar θ angle is defined as 0° for a magnetic field that is pointing upwards in the lab frame. It should be noted that the detection of both optical transitions in Figure 4.4a is only possible due to the fact that this emitter possesses a relatively high cyclicity of the spin-conserving transitions. The measurement is done at a base temperature of around 400 mK, meaning that the T_1 spin-relaxation time of the emitter is estimated at several tens of seconds to minutes [102]. Therefore, the population of the two non-degenerate ground states is only transferred by the non-zero probability of a relaxation event through the spin-flipping transition (i.e. spinpumping). The data in Figure 4.4a is taken by scanning the laser over each frequency and measuring the emitter's response to it over the course of several milliseconds. If the probability of spinpumping was high, there would only be counts for the first few cycles of the optical transition, before trapping the emitter in the opposite spin state. Given the sufficient SNR of this measurement, it can therefore already be predicted that this emitter has a high cyclicity of the spin-preserving transitions.

The shape of the splitting profile of this emitter gives insights into two important characteristics, both of which are easier observed in Figure 4.4b. This figure shows the size of the splitting between the two transitions at each row of Figure 4.4a. This splitting size is found by fitting each linescan to a double Voigt profile and calculating the peak distances. The first important characteristic that can be derived from this measurement is the orientation of the dipole moment of this emitter in the lab frame. The waveguides in the diamond sample are cut along the crystallographic <110> direction, which means that there are 4 tin-vacancy configuration with different orientations (ϕ, θ) in the diamond unit cell: $(\pm 90°, 54.7°)$ and $(0°, \pm 125.3°)$. The maximum splitting at $\phi = 0°$, $\theta = 125.3°$ visually reveals that this emitter has the $(0°, 125.3°)$ orientation. This observation is quantitatively confirmed by a fit of the Hamiltonian. Knowing the orientation of the dipole moment of the emitter in the lab frame is crucial for aligning the magnetic field to the emitter, which will become important for microwave driving in Chapter 5. Next to the orientation of the dipole moment, the fit of the Hamiltonian to the splitting at each magnetic field angle also enables an estimation of the strain magnitude. Visually, a significant amount of strain manifests itself in these experiments as a peak in splitting at a perpendicular magnetic field (see Section 2.1.4). From the fit of the Hamiltonian, the ground-state strain parameter was estimated to be $\Upsilon_g/2\pi = 60(10)$ GHz.

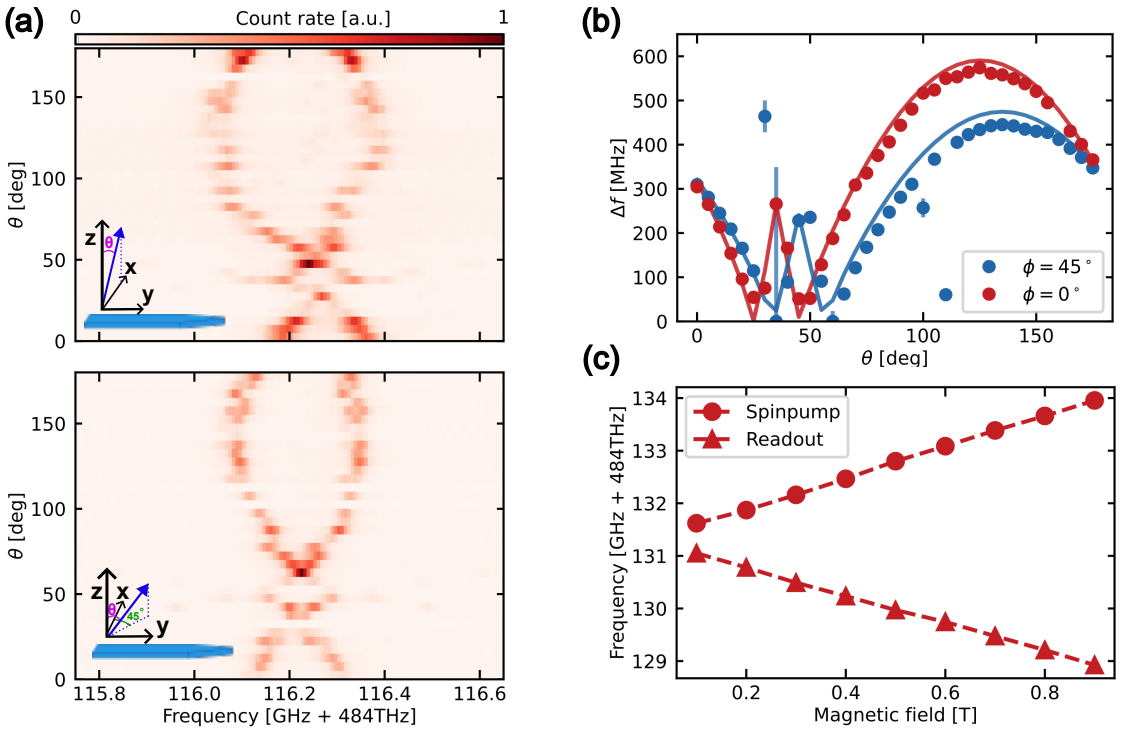

Figure 4.4: The optical manifold of a tin-vacancy center at non-zero external magnetic fields. (a) A set of PLE linescans at different magnetic field orientations. The two figures are taken at two different azimuthal angles $\phi \in \{0°, 45°\}$, as indicated by the schematic graphics. The polar angle θ is swept on the y-axis of each of the figures and the strength of the magnetic field is kept constant at 100 mT. (b) A different representation of the data in (a), where only the frequency difference between the two peaks in each row of (a) is plotted against the polar angle θ. This is done for both the $\phi = 0°$ (red) and the $\phi = 45°$ (blue) case. The solid lines are fits of the data to the unperturbed tin-vacancy Hamiltonian, as presented in Section 2.1.2. This fit reveals a ground-state strain magnitude of $\Upsilon_g/2\pi = 60(10)$ GHz. (c) The dependency of the spin-conserving transition frequencies on the strength of the magnetic field, when it is aligned with the symmetry axis of the tin-vacancy center. Both the spinpump (triangles) and readout (circles) transitions are plotted for 9 different magnetic field strengths, leading to a linear dependence with a slope of $(5.58 \pm 0.07)\,\frac{\text{GHz}}{\text{T}}$. The figure is taken with a different emitter than (a) and (b), which explains the shift of the central frequency of the transitions compared to (a) and (b).

Since the splitting of the optical transitions is caused by the Zeeman effect, it is trivial to derive that the magnitude of the splitting between the two spin-preserving transitions should increase linearly with the magnetic field strength. To demonstrate this, Figure 4.4c shows the measurements of the optical transitions of a different emitter (compared to 4.4b and 4.4c) for magnetic field strengths between 100 and 900 mT. The theoretical prediction of a linear relation matches the measured data very well. A splitting ratio of $(5.59 \pm 0.03)\,\frac{\text{GHz}}{\text{T}}$ is found, which matches previously reported values in literature [52, 56]. The fact that this measurement shows such low fluctuations of the resonances when increasing the magnetic field demonstrates that the magnetic field strength can effectively be leveraged as a tuning mechanism for overlapping the optical transitions of two emitters (as further explored in Section 7.1).

5

Microwave driving of tin-vacancy centers in different strain regimes

This chapter will focus on characterizing the spin dynamics of the tin-vacancy center. Firstly, the readout and initialization dynamics will be explored, which are essential capabilities for any experiments involving coherent spin control. Then, the microwave driveability of two tin-vacancy centers will be explored, highlighting the crucial role of strain for the microwave control over the qubit states. Finally, the decoherence of these emitters will be studied, leading to an estimate of the characteristic timescale for decoherence. The results from this chapter reveal the ability to coherently manipulate the electron spin state of a low-strain tin-vacancy center. This ability is an essential ingredient for future use-cases of these types of defects in applications such as the double-click entanglement protocol.

5.1. Initialization and readout dynamics

Essential ingredients for experiments involving spin dynamics are the abilities to both deterministically initialize the spin state into a pure state and to readout any spin state with a high fidelity, preferably in a single-shot fashion. This section will focus on the experimental work that has been done to achieve this. Figure 5.1a shows the relevant level structure of the tin-vacancy center, when subject to an external magnetic field. The $|1\rangle$ and $|2\rangle$ states form the computational basis (i.e. "spin-up" and "spin-down"). The transitions between the computational basis and the excited states are used for readout and initialization. Both of these capabilities are done by cycling the respective spin-conserving transitions. At an aligned magnetic field, the Hamiltonian of the tin-vacancy center has a finite cyclicity, whose exact value depends on the exact strain configuration (see Section 2.1.3). This finite cyclicity translates into a non-zero probability of decaying through a spin-flipping transition after excitation of a spin-conserving transition (indicated by the pink arrows in Figure 5.1a). For initialization, this means that cycling the $|2\rangle - |B\rangle$ transition for sufficiently long times guarantees that the population of the $|2\rangle$ state goes to zero. This principle is referred to as "spinpumping". For readout however, it means that there is only a finite number of cycles of the transition that can be done before the spin state is altered and all quantum information is lost. Measuring the characteristics of this behavior is extremely important for understanding the constraints in later experiments in terms of readout and initialization times and powers. Figure 5.1b shows the time-dependent intensity in the PSB collection path during both initialization and readout. Clearly, the population transfer during both these periods show exponential behavior. The shape of this exponential behavior can be used to estimate the the probability of spin-flipping decay events. To extract the rate of these decay events, one can note that the exponential probability distribution of staying in the spin-conserving readout transition can be written as

$$P_{|1\rangle}(t) = \frac{1}{\eta\tau_{\text{cycle}}} e^{-\frac{t}{\tau_{\text{cycle}}\eta}} = \Gamma e^{-\Gamma t}, \tag{5.1}$$

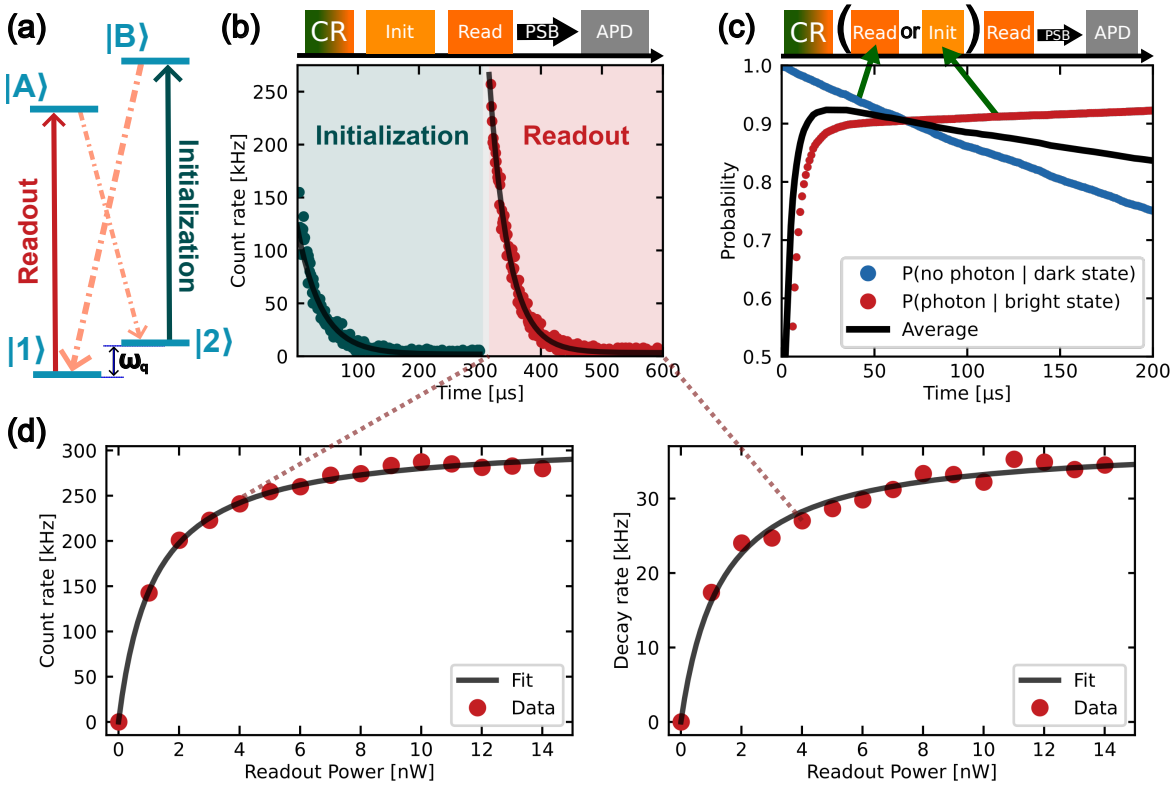

Figure 5.1: Initialization and readout dynamics of a tin-vacancy center at an aligned magnetic field of 100 mT. (a) A schematic of the electronic eigenstates in the Zeeman-split tin-vacancy Hamiltonian. For visualization purposes, only the lower branches of the ground and excited state are shown. The two spin-preserving transitions are used for readout and initialization. (b) Measurement of the population transfer during initialization and readout. During the first 300 µs, the initialization transition is driven with 4 nW resonant power. After this, the readout transition is driven with this same power for the next 300 µs. Both parts of the graph show exponential population transfer, caused by the finite cyclicity. (c) Calibration curve for the Single-Shot Readout (SSRO) duration. The red points show the probability of measuring a photon when the spin is prepared in the bright $|1\rangle$ state for different durations of a 2 nW readout pulse. The blue points show the probability of measuring no photons when the spin is prepared in the dark $|2\rangle$ state, again for different durations of this same readout pulse. These probabilities are summarized through their averages in black. At a readout time of 30 µs, the average fidelity is maximized at $F = 0.924 \pm 0.002$. (d) A saturation measurement at magnetic field, which is done by repeating the measurement from (b) for 15 different powers of the readout block between 0 and 15 nW. The exponential decay during the readout pulse is then fitted to $I = A \cdot e^{-\Gamma t}$. The left figure shows the fitted values of the count rate amplitude A and the right figure shows the fitted values of the decay rate Γ. The trend of these values is again fitted to Equation 2.17 to find saturation powers of $P^{\mathrm{A}}_{sat} = (2.3 \pm 0.1)$ nW and $P^{\Gamma}_{sat} = (2.7 \pm 0.3)$ nW, which agree within their respective uncertainties.

where τ_{cycle} is the expectation value for the amount of time that a spontaneous decay event takes and η is the cyclicity. The decay rate Γ is defined here as $\Gamma \equiv \frac{1}{\eta \tau_{\mathrm{cycle}}}$, which means that the cyclicity η is the expectation value for the number of spin-conserving transitions that occur before a spin-flipping transition. Fitting the decay of the readout signal in Figure 5.1b gives access to the value of Γ. Since τ_{cycle} depends on the average excited state population, the value of η can only be calculated in an experiment where the average excited state population is known. From the theoretical model in Section 2.1.3, it is shown that this average excited state population is exactly $\frac{1}{3}$ at the saturation power. Combining this knowledge with the lifetime of the emitter gives an exact measure for τ_{cycle}. A measurement of Γ at saturation power can thereby directly be used to estimate the cyclicity η.

To find the saturation power of this emitter at an aligned magnetic field of 100 mT (and an aligned polarization), the experiment in Figure 5.1b is repeated for 15 different optical powers of the readout block between 0 and 15 nW. This leads to 15 different exponential decays of the intensity in the PSB collection path during the readout pulse. Each of these peaks is fitted to an exponential ($I = A \cdot e^{-\Gamma t}$). The fitted values of the amplitude (A) and decay rate (Γ) are shown for each power in Figure 5.1d. As predicted by Equation 5.1, both the

amplitude and decay rate of these fits depend linearly on Γ, which follows the saturation curve equation as described in Equation 2.17. The measurements indeed clearly reflect this behavior, as can be seen by the black fit line, which is calculated with Equation 2.17. These two fits give two different values of the saturation power: $P^A_{sat} = (2.3 \pm 0.1)$ nW from the amplitudes and $P^\Gamma_{sat} = (2.7 \pm 0.3)$ nW from the decay rates, which do agree with one another within their respective uncertainties.

Taking the average of these measures as the true saturation power gives a fitted decay rate at saturation power of (24.6 ± 0.5) kHz. Given the average excited state population of $\frac{1}{3}$ at saturation power, the expected cycle time can be calculated through the lifetime as

$$\tau_{\text{cycle}} = 3\,\tau_{\text{lifetime}}. \tag{5.2}$$

Similarly to Section 4.3, a lifetime of (7.0 ± 0.5) ns is used to find an optical cycle time of $\tau_{\text{cycle}} = (21 \pm 2)$ ns. This ultimately leads to an estimated cyclicity of $\eta = \frac{1}{\Gamma \tau_{\text{cycle}}} = (1.9 \pm 0.1) \cdot 10^3$. The magnitude of the cyclicity is especially important for the single-shot readout fidelity. The ratio between the cyclicity and collection efficiency give a very rough estimate for the mean-photon number that can be measured during a single resonant readout pulse, which has a direct influence on the feasibility of single-shot readout. A high cyclicity is thus preferred for higher fidelity readout, but does come at the cost of a longer initialization duration due to the slower spinpumping dynamics. The cyclicity of this emitter gives optimistic initial indications for the feasibility of Single-Shot Readout measurements.

Optimizing the trade-off between readout and initialization is extremely important for reaching optimized fidelities. The effect of longer initialization times is mostly noticed in the rate of experiments. Therefore, the initialization time can simply be chosen to be sufficiently long to have a nearly full population transfer in early-stage experiments. For the readout duration this luxury does not exist, as the influence of dark counts reduces the probability of correct state assignment at long readout times. The trade-off between readout duration and fidelity is shown in Figure 5.1c. The red points in this figure show the probability of measuring a photon in the PSB collection path when the spin state is initialized in the bright $|1\rangle$ state for a range of different readout times. The slope of this curve decreases over time due to the exponential characteristic of the spin-flipping probability from the finite cyclicity. Moreover, at some point the curve saturates to a probability smaller than 1. This is because of the fact that the probability of measuring the "first" photon becomes extremely small after a few cyclicities (since measuring the first photon is conditioned on not having measured a photon in all previous bins, while the spin has also not flipped). The exact probability distribution of these events is a combination of a geometric distribution from the finite spin-flip probability, a binomial distribution of the detection efficiency and Poissonian distribution describing noise counts [123]

The blue datapoints in Figure 5.1c signify the probabilities of not measuring a photon if the spin state is initialized in the dark $|2\rangle$ state for different readout durations. The linear slope of the points is related to the dark count rate, originating mostly from reflected readout laser photons in the collection path. From the measured slope in Figure 5.1c, a dark count rate of (1.231 ± 0.005) kHz is estimated, which agrees with noise floors at this power in measurements such as Figures 5.1b and 4.2a.

Finally, the black points in Figure 5.1c are the calculated averages of the red and blue points. These capture the relation between the average probability of successful state assignment and the readout pulse duration. This success probability defines as the fidelity of the SSRO state measurement. Figure 5.1c shows that this quantity is optimized at a readout duration of 30 µs (indicated by the black line), where the fidelity is found to be $F_{SSRO} = (92.4 \pm 0.2)\,\%$, which is the highest reported SSRO fidelity for any tin-vacancy center in literature [37, 121, 124, 125]. The increased fidelity of SSRO is mainly attributed to an increased collection efficiency compared to experiments conducted in bulk diamond. The fidelity can still be improved by a reduction in dark count rates, believed to mainly be caused by either laser leakage into the PSB collection path or fluorescence of the PSB collection fiber going into the detector.

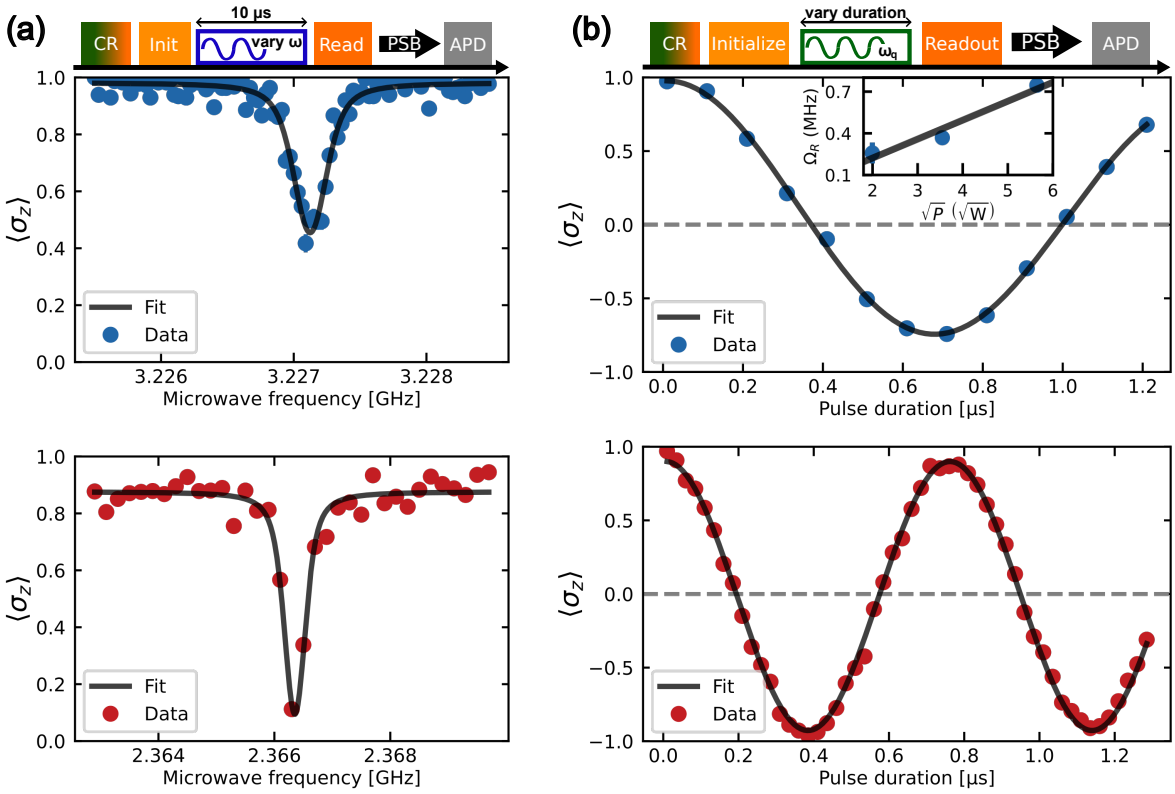

Figure 5.2: A comparison of the microwave driving efficiency of the tin-vacancy electron spin at low and high strain regimes. (a) Optically Detected Magnetic Resonance (ODMR) measurements for two emitters. The top graph corresponds to the emitter with low strain and the bottom graph to the emitter with high strain. The value of $\langle \sigma_z \rangle$ is extracted from a Bayesian Unfolding algorithm, which finds the most-likely bright state population given the SSRO outcomes of the many repetitions of the experiment [41]. This same algorithm also produces the (barely visible) errorbars on the datapoints. The contrast of the ODMR dip for the low (high) strain emitter is 0.264 ± 0.007 (0.39 ± 0.02) with a FWHM of $\Gamma = (300 \pm 10)$ kHz ($\Gamma = (440 \pm 40)$ kHz). The center of the low (high) strain peak is at a qubit frequency of $\omega_q = 2\pi \cdot (3.227\,123 \pm 0.000\,003)$ GHz ($\omega_q = 2\pi \cdot (2.366\,35 \pm 0.000\,01)$ GHz). The difference in the two qubit frequencies is mainly explained by a 45° misalignment of the magnetic field for the high-strain emitter. (b) Measurement of Rabi oscillations of the population when the spin is driven resonantly, again for a low strain (top) and high strain (bottom) emitter. Fitting the data with an exponentially decaying cosine squared model reveals a Rabi frequency of the low (high) strain emitter of $\Omega_R = 2\pi \cdot (0.74 \pm 0.02)$ MHz ($\Omega_R = 2\pi \cdot (1.324 \pm 0.004)$ MHz). The inset in the top graph shows the dependency of the Rabi frequency of the low strain emitter on the square root of the power of the MW source, which is fitted with the theoretically predicted linear relation.

5.2. Coherent control of the tin-vacancy center electron spin

The knowledge about the initialization and readout dynamics of the tin-vacancy center electron spin from the previous section allows us to measure the dynamics of coherent spin manipulation. This section will focus on developing and characterizing this ability for two distinct emitters: One in a low-strain regime and one in a higher strain regime. The level of strain for these emitters is estimated from a combination of magnetic field sweeps (such as Figure 4.4a) and cyclicity measurements at different magnetic field angles (such as in Figure 5.1b). The exact strain parameters are not known for these two tin-vacancy centers, but from these estimates it can be concluded that one has a much *higher* level of strain than the other, leading to the classification of these emitters as "low-strain" and "high-strain".

As discussed in Section 2.1.4, the electron spin state can be manipulated through oscillating magnetic fields. Effectively, driving can only be done when the oscillation frequency of the magnetic field is closely on resonance with the energy splitting between the two spin states. This splitting is extremely sensitive to parameters such as strain, magnetic field orientation and dipole orientation. Therefore, the first requirement for achieving spin manipulation is to find the exact resonance frequency of the qubit transition. The measurements that were conducting to this end can be found for the two differently strained emitters in Figure 5.2a. Here, the

emitter is initialized in the bright $|1\rangle$ state after passing a CR-check. Then, an oscillating current is supplied through the bondwire, effectively creating an oscillating magnetic field with a non-zero perpendicular component at the location of the emitter. After 10 µs, the current is turned off and a SSRO measurement of the electron spin is done. This procedure is repeated for a range of microwave (MW) frequencies of the oscillating current. Population transfer from the bright $|1\rangle$ state to the dark $|2\rangle$ state is only possible if the MW frequency is close to the qubit frequency. For this reason, a dip in the bright state population reveals an Optical Detection of the Magnetic Resonance (ODMR). Figure 5.2a shows the results for both emitters. The ODMR measurements of both strain regimes feature the characteristic ODMR dip, signifying the spectral position of their respective qubit transitions. The fact that the ODMR contrast of the high strain emitter is much better than that of the low strain emitter is a first indication of the difference in microwave driveability of these emitters. Moreover, the big difference in the qubit frequencies can mainly be explained by the fact that the magnetic field is 45° misaligned for the high-strain emitter, while being aligned for the low-strain emitter (see Section 2.1.4).

The knowledge about the absolute value of the frequency of the qubit transition allows us to coherently manipulate the spin state of the electron by applying a microwave pulse on resonance with it. The population transfer then depends on the power of the pulse and its duration. At a constant pulse power, the spin state oscillates between the two eigenstates with the Rabi frequency. A measurement of these Rabi oscillations can be found in Figure 5.2b, again for both strain regimes. Both emitters show Rabi oscillations, but with different features. Firstly, the Rabi frequency of the high strain emitter ($\Omega_R/2\pi = (1.324 \pm 0.004)$ MHz) is much higher than the low strain Rabi frequency ($\Omega_R/2\pi = (0.74 \pm 0.02)$ MHz). This difference in Rabi frequencies is a direct result of the influence of strain on the microwave driveability as presented in Section 2.1.4 . The Rabi frequency directly determines the duration that is necessary for the π- and $\frac{\pi}{2}$-pulses, which are crucial for the double click entanglement protocol (see Section 2.3.1). Next to the speed of these gates, an even more crucial parameter is their fidelity. From the fits in Figure 5.2b, the π-pulse fidelities are estimated to be $F_\pi = 0.980 \pm 0.002$ for the high-strain emitter and $F_\pi = 0.871 \pm 0.006$ for the low-strain emitter. This fidelity will directly impact the fidelity of the entangled Bell state after a successful realization of the double click protocol. The infidelities in the gates mostly originate from T_2 decoherence. The magnitude of this decoherence will quantitatively be characterized in the next section. Qualitatively, this decoherence can mostly be attributed to coupling of the ensemble of ^{13}C spin-1/2 systems surrounding the tin-vacancy spin system. The random orientations of these nearby spins cause decoherence, which means that faster driving is required to minimize the effect of this noise source [37]. One solution is presented in the inset of the low strain graph in Figure 5.2b. This inset shows the increase of the Rabi rate proportional to the square root of the driving power. By improving the driving power, faster oscillations can be realized that would thereby suffer less from the decoherence caused by the nuclear spin bath. Unfortunately though, increasing the driving power also increases the amount of dissipated heat in the bondwire, which can increase phonon-induced decoherence channels.

5.3. Characterization of decoherence times

The previous section explored the speed and fidelity of spin manipulation on a low- and high-strained emitter through Rabi oscillations. It is essential for the double-click protocol to have high-fidelity control over the state of the electron spin, but this is not enough. Next to the ability to create superposition spin states, it is also crucial that the superposition does not decohere within the time it takes to create and measure the entanglement. To test the decoherence time of the emitters, a Hahn-Echo sequence is used. This sequence is composed of 3 gates, whose durations are calibrated from the Rabi measurements of Figure 5.2b. The sequence starts by initializing the spin in the bright $|1\rangle$ state, after which an $R_x(\pi/2)$ gate creates an equal superposition of the $|1\rangle$ and $|2\rangle$ states. This superposition is freely evolved for some time $t/2$, after which a refocusing $R_x(\pi)$ pulse is applied. The spin state is then freely evolved again for a time $t/2$, after which the state is projected to the $|1\rangle$ state with an $R_x(-\pi/2)$ gate. Figure 5.3 shows the relation between the total evolution time t and the expectation value of the spin state in the z-direction $\langle\sigma_z\rangle$ for both the low- and high-strain emitters.

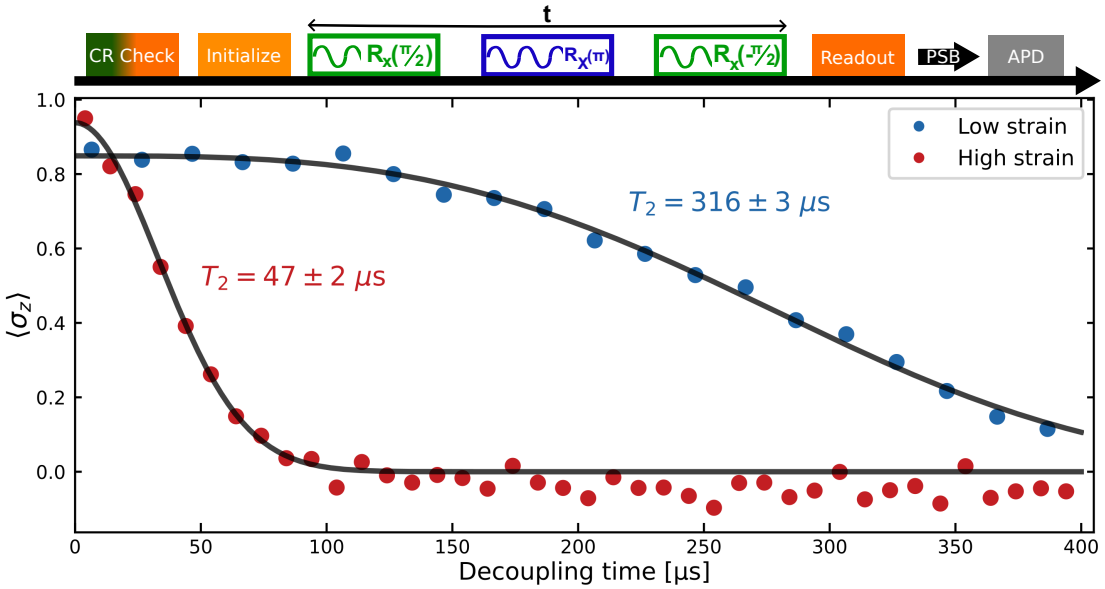

Figure 5.3: Hahn-Echo measurement of the decoherence of a low- and high-strain tin-vacancy center. The horizontal axis is defined as the total free evolution time. The MW gate times were calibrated with the results from Figure 5.2b. The data is fitted to a superexponential with exponents of $\alpha = 3.1 \pm 0.1$ and $\alpha = 2.0 \pm 0.1$ for the low- and high-strain emitters respectively. The fit for the low strain emitter reveals a decoherence time of $T_2 = (315 \pm 3)\,\mu s$, while the high strain emitter shows a decoherence time of $T_2 = (47 \pm 2)\,\mu s$. The high strain emitter data was taken with 10 times less MW driving power.

The data in Figure 5.3 is fitted to a super-exponential with powers $\alpha = 3.1 \pm 0.1$ and $\alpha = 2.0 \pm 0.1$ for the low- and high strain emitter respectively. The fitted decay constants directly reveals the T_2 decoherence time, which is found to be $T_2 = (47 \pm 2)\,\mu s$ for the high strain emitter and $T_2 = (316 \pm 3)\,\mu s$ for the low strain emitter. The striking difference in the decoherence time could be related to the strain magnitude. One explanation of the difference could be a strain-induced increase of the overlap of the electronic wavefunction with a vibronic mode in the diamond lattice, which can cause an increased coupling to phonon-induced loss channels. It should however be emphasized that many parameters besides strain can have an influence on the decoherence time of the electron spin. Parameters such as the position in the waveguide, distance to the bondwire, local charge environment and local heat distributions also play a crucial role in the decoherence time. And most significantly, the density of the spin bath around the emitter is crucial for the decoherence time. The presence of relatively close ^{13}C nuclear spin-1/2 systems with randomly precessing spin orientations causes decoherence of the tin-vacancy spin state. Moreover, noise from close electron spins in the valence band of the diamond can have a similar effect. The significance of decoherence from the spin bath can experimentally be isolated through more in-depth experiments [37], which have not been done in this work. Crucially, the total entanglement protocol (including tomography) is expected to take ~(5-10) µs after the creation of the superposition [30], meaning that only the high strain decoherence time is somewhat limiting for the overall entanglement fidelity. It should however be noted that the decoherence time of tin-vacancy centers can in principle be extended by decoupling sequences [49, 52, 56], which are possible due to the relatively high gate fidelities of this emitter. Lastly, Figure 5.3 shows a low fidelity even at zero decoupling time for the low strain emitter. This fidelity loss can be explained by the gate infidelities from Figure 5.2b, which come in as linear factors in the the infidelity of the spin-coherence without free evolution. The decoherence time of this emitter is much longer than the expected entanglement generation sequence time, meaning that decoupling sequences are not needed in order to preserve the spin state coherence. Such sequences would also decrease state fidelities because of the relatively low gate fidelities on this emitter.

In conclusion, this section has shown coherent spin manipulation of both a low- and high-strain emitter, focusing on the difference in their microwave driving efficiency. The decoherence times of these emitters were measured with a Hahn-Echo sequence, which showed a relatively low decoherence time for the high-strain emitter. This decoherence time can in principle be extended with dynamical decoupling sequences. The low-strain emitter has a sufficiently high decoherence time, but does suffer from relatively high gate infidelities.

6

Measurements of single photons from the optical transitions of a tin-vacancy center

The characterization of the optical transitions in Chapter 4 demonstrates control over the optical manifold on a timescale of tens of microseconds. For the tin-vacancy center to function as a quantum node, the optical transitions must be coherently controlled on the single-photon level, which means that optical control on the timescale of the excited state lifetime has to be achieved. This chapter will focus on the measurements that demonstrate pulsed control of the orbital state of the tin-vacancy center. These pulsed experiments will serve as measures for two important parameters: The excited state lifetime and the collection efficiency of photons emitted in the Zero-Phonon Line (ZPL) of the C-transition (see Section 2.1.3). The former is crucial for knowing the transform-limited linewidth of the optical transition and for optimizing the pulse length in terms of double excitations. The latter is an important parameter for the entanglement success probability and thereby the rate. After this, the single photon nature of the incoming photons is proven by correlations in detection events on the output arms of a Hanbury-Brown-Twiss interferometer in the ZPL collection path. The unlikeliness of simultaneous detections on both detectors after excitation of a single emitter is crucial for heralded entanglement schemes such as the double-click protocol.

6.1. Coherent driving of the optical transition

In order to coherently control the orbital state of the electron spin, it is crucial to use optical pulses that are significantly shorter in time than the excited state lifetime [120]. This is most-notably due to the fact that longer optical pulses will introduce higher contributions of double-excitations, which in turn lead to infidelity for heralded entanglement schemes. On the other hand however, narrower optical pulses in the time domain will have a bigger spread in the frequency domain[1]. For the double-click entanglement scheme, it is important that the pulse is sufficiently narrow in frequency to not excite both spin-conserving transitions simultaneously. To work around this trade-off, an optical pulse of 1.5 ns is used here. Section 3.5 presents the experimental procedure for creating such short optical pulses in the setup. Next to the control over the pulse duration, the setup configuration gives access to the pulse amplitude through the voltage of the Acousto-Optic Modulator (AOM). The suppression factor between the EOM on- and off-voltage is estimated at 1522 from Figure 3.4. Combining this value with a calibration of the AOM voltages gives a direct way of translating the supplied AOM voltage to an estimate of the pulse power. Figure 6.1a shows a measurement of the counts per shot in the PSB and ZPL measurement windows for a range of these estimated pulse powers. The figure clearly shows the optical Rabi population transfer, as expected for a coherently driven two-level system. The measured data fits very well to the theoretical model, which predicts an optical π-pulse power of $P_\pi = (103 \pm 2)$ nW.

[1] For example: A 0.5 ns Gaussian pulse corresponds to a Gaussian in the frequency domain with a FWHM of 880 MHz. Such a pulse would still have ~ 80 % of its peak power at the frequency of the other spin-conserving transition (for a 100 mT aligned B-field). In contrast, a 1.5 ns pulse only has a 293 MHz FWHM, which translates to a ~ 12 % overlap with the other spin-conserving transition at 100 mT.

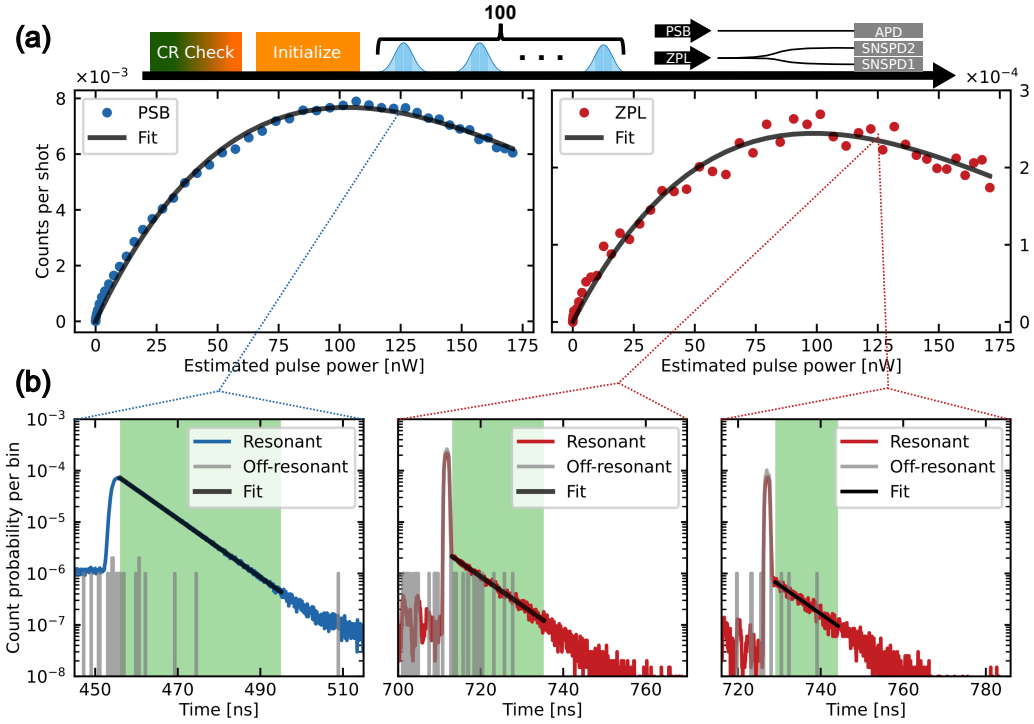

Figure 6.1: Coherent control of the optical C-transition of a tin-vacancy center. (a) A calibration of the pulse power that is required to achieve a π rotation of the state on the Bloch sphere for a 1.5 ns pulse. The two panels belong to the measurement in the PSB (blue) and ZPL (red). The ZPL panel shows the sum of the counts in the measurement window of both SNSPDs. The x-axis is constructed by a combination of the AOM voltage calibration and the estimated EOM suppression factor. (b) The histogram of detection events after exciting the defect with the calibrated π-pulse for three detectors: The PSB APD (left) and the two ZPL SNSPDs (middle and right). The panels show both a resonant and off-resonant (2 GHz detuned) repetition of the experiment. The exponential tail in the measurement window is fitted to an exponential function, revealing a lifetime of (7.7 ± 0.2) ns. The integrated counts for both ZPL detectors are found to be: $(1.96 \pm 0.01) \cdot 10^{-4}$ on SNSPD 1 and $(5.68 \pm 0.05) \cdot 10^{-5}$ on SNSPD 2. It should be noted that these collection efficiencies are further optimized for the final TPQI experiment in Chapter 7.

The measured values in Figure 6.1a are expressed as *counts per shot*. This quantity is obtained by integrating the count probability over all bins within the measurement window, as graphically represented in Figure 6.1b. The figure shows histograms of the photon detection times for the PSB detector and both ZPL detectors. Here, the measurement window is chosen to be as close as possible to the EOM pulse, without containing it on the one side. On the other side, the end of the window is chosen such that the Signal-to-Noise Ratio is at least 10. Figure 6.1b is taken at the calibrated AOM voltage that corresponds to a π-pulse (as determined from Figure 6.1a). The characteristic exponential decay of spontaneously emitted photons is clearly visible in the measurement windows of all three panels.

To further emphasize that the detection events in this histogram are actual single photons emitted by tin-vacancy centers, we repeat the measurement with an off-resonant (2 GHz detuned) excitation laser. The absence of the exponential decay in this experiment is a strong indication that the detection events in the resonant measurement belong to spontaneously emitted photons from the C-transition of a tin-vacancy center. The detection events during off-resonant excitation in the ZPL measurement window are attributed to non-perfect cross-polarization extinction of the laser (see Section 3.6). These "noise counts" have a big impact on the fidelity of the double click protocol (see Section 2.2.3 & 2.3.2), which is why a significant effort is done to minimize these.

Finally, the exponential decay in all three panels can be fitted to obtain the lifetime of this specific emitter. Fitting all three histograms leads to an average lifetime of $\tau = (7.7 \pm 0.2)$ ns. This value is slightly higher than previously reported values of the excited state lifetime of a tin-vacancy center [50, 51]. The increased lifetime

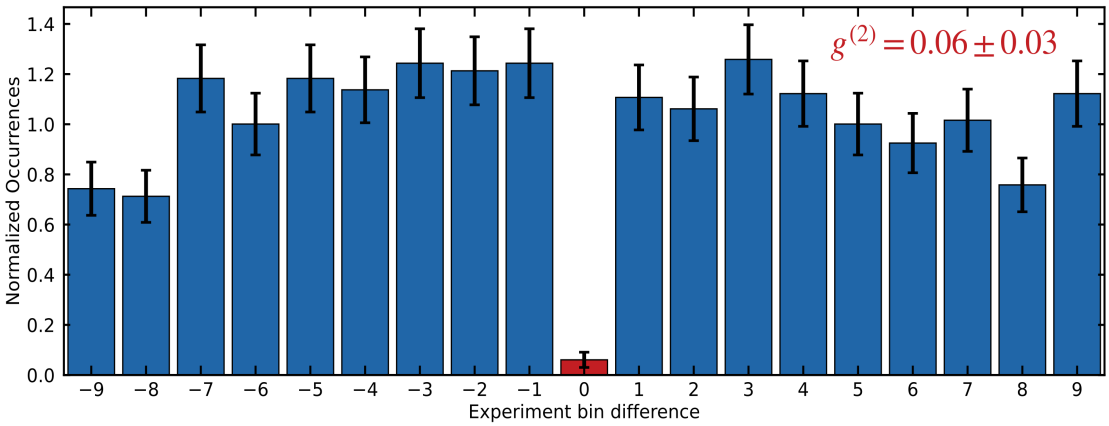

Figure 6.2: Normalized histogram representing a $g^{(2)}$-measurement of a tin-vacancy center in a waveguide at non-zero magnetic field. The horizontal axis of this histogram represents the time difference between different shots of the experiment (i.e. the bin at an "experiment bin difference" of 1 corresponds to detector 1 measuring a photon in shot $i \in \{1,2,\ldots,100\}$ and detector 2 measuring a photon in shot $i+1$). The errorbars on this data represents the Poissonian distribution that underly the coincidences. The number of coincidences in the zero bin (red) reveal a normalized autocorrelation value of $g^{(2)}(0) = 0.06 \pm 0.03$, which is sufficiently low to prove the single photon nature of the source.

here is largely attributed to the fact that these tin-vacancy centers reside in waveguides and not in bulk diamond. The photonic density of states in the environment of the emitter follows from the dispersion relation and scales with the refractive index as n^3 [126]. Emitters in bulk diamond are mostly surrounded by diamond, which has a higher refractive index ($n \approx 2.4$ [40]) compared to the vacuum ($n = 1$) that dominates the surroundings of emitters in waveguides. The lower local density-of-states for emitters in waveguides lead to lower rates of spontaneous emission for these emitters through Fermi's golden rule [73].

6.2. Time correlations between single photons

The final ingredient in demonstrating optical control over the tin-vacancy center is to prove that the defect is a single photon source. To test this hypothesis, the emitter is excited by optical π-pulses as calibrated in Section 6.1. Crucially, if the defect is an ideal single photon source, then a Hanbury-Brown-Twiss interferometer in the collection path should never measure coincidences on the detectors [127]. By repeating the experiment from Figure 6.1b and measuring the time differences between detection events on both SNSPDs, a histogram of the coincidences in terms of detection time differences can be made. This histogram can be found in Figure 6.2. The horizontal axis in the figure represents the time difference between consecutive shots of the experiment. The zero bin therefore represents the number of instances where both SNSPDs measured a photon in the same shot of the 100-pulse experiment. Visually, one can clearly see the dip in the measured coincidences in this zero bin compared to all other bins. From this measurement, a normalized coincidence probability of $g^{(2)}(0) = 0.06 \pm 0.03$ is found. The normalization is done here with respect to the average non-zero bin height. In literature, the condition of $g^{(2)}(0) < 0.5$ is often presented as "proof" of the measurement of single photons (even though this argument should actually involve some nuances [128]). It should however be noted that this requirement is not sufficient for the goal of proving photon indistinguishability between two sources. For both the double-click entanglement protocol and a TPQI measurement, the probability of measuring coincidences from excitation of a single emitter hurt the visibility and entanglement fidelity. The non-zero $g^{(2)}(0)$ value in this measurements is mostly attributed to laser leakage in the measurement window due to non-perfect cross-polarization extinction. This noise source can be mitigated through a more favorable choice of the measurement and correlation window. This optimization will be done for the emitters that are used in the TPQI experiment in Chapter 7. The low $g^{(2)}(0)$ value here suffices to prove the single-photon behavior of the emitter and gives optimistic estimations for the expected TPQI visibility when compared to measurements on the NV center [129–133] and SiV center [47, 134, 135]. Moreover, the measured value here constitutes the lowest measured value on the SnV center [50, 136, 137].

7

Quantum interference between photons from two tin-vacancy centers

The results from the previous sections have demonstrated fully coherent control over both the optical and microwave transitions of a tin-vacancy center. This control can be leveraged to further verify the potential of building a Quantum Network Node with a tin-vacancy center. A central ingredient in generating entanglement between Quantum Nodes is the Bell-State Measurement (BSM) between the flying photonic qubits that are entangled with the quantum states of the stationary nodes. In such a scheme, the interference of two photons originating from two different nodes at a central beam-splitter is the crucial ingredient. This section will test the efficiency of such Two-Photon Quantum Interference (TPQI) for photons originating from two different tin-vacancy centers, which is an effort that has not yet been achieved in literature.

7.1. Properties and requirements of the individual nodes

To test the interference between photons from two different tin-vacancy centers, it is crucial that these emitters meet certain requirements. Table 7.1 lists all the properties of the two tin-vacancy centers that were used for the experiment, which are conveniently labeled as *Alice* and *Bob*. These two emitters were chosen for this experiment after an extensive search, where a certain set of parameters was tested for a large set of emitters. Firstly, the linewidth of the emitter was regarded as an important measure. If a CR-checked PLE (see Section 4.2) could not bring the linewidth of the optical transition at zero magnetic field close to the expected lifetime-limit, then the emitter was discarded as unusable for a TPQI experiment (as motivated by the theory in Section 2.2.2). The emitters presented in Table 7.1 have linewidths of (22.7 ± 0.4) MHz and (33.8 ± 0.7) MHz, while their lifetimes reveal lifetime-limited linewidths of (21.4 ± 0.2) MHz and (23.2 ± 0.2) MHz. The linewidth of Alice is

Table 7.1: Summary of the most important parameters of the two emitters that are used to for the TPQI experiment. Each property (except for the orientation) is accompanied by an uncertainty, which is either extracted from either a fit or the standard deviation in repeated measurements. The definitions of the angles ϕ and θ are consistent with those in Figure 4.4. The methodologies for finding each of these properties have been demonstrated in Chapters 4-6.

	Alice	Bob
Central frequency (GHz w.r.t. 484 THz)	131.38 ± 0.05	127.21 ± 0.05
Splitting rate $\left(\frac{\text{GHz}}{\text{T}}\right)$	5.59 ± 0.03	5.55 ± 0.01
Dipole orientation	$\phi = 90°, \theta = 54.7°$	$\phi = 90°, \theta = 54.7°$
Saturation power (nW)	4.0 ± 0.5	2.7 ± 0.5
Cyclicity	1618(70)	1456(90)
Optical linewidth (MHz)	22.7 ± 0.4	33.8 ± 0.7
Lifetime (ns)	7.45 ± 0.06	6.87 ± 0.06

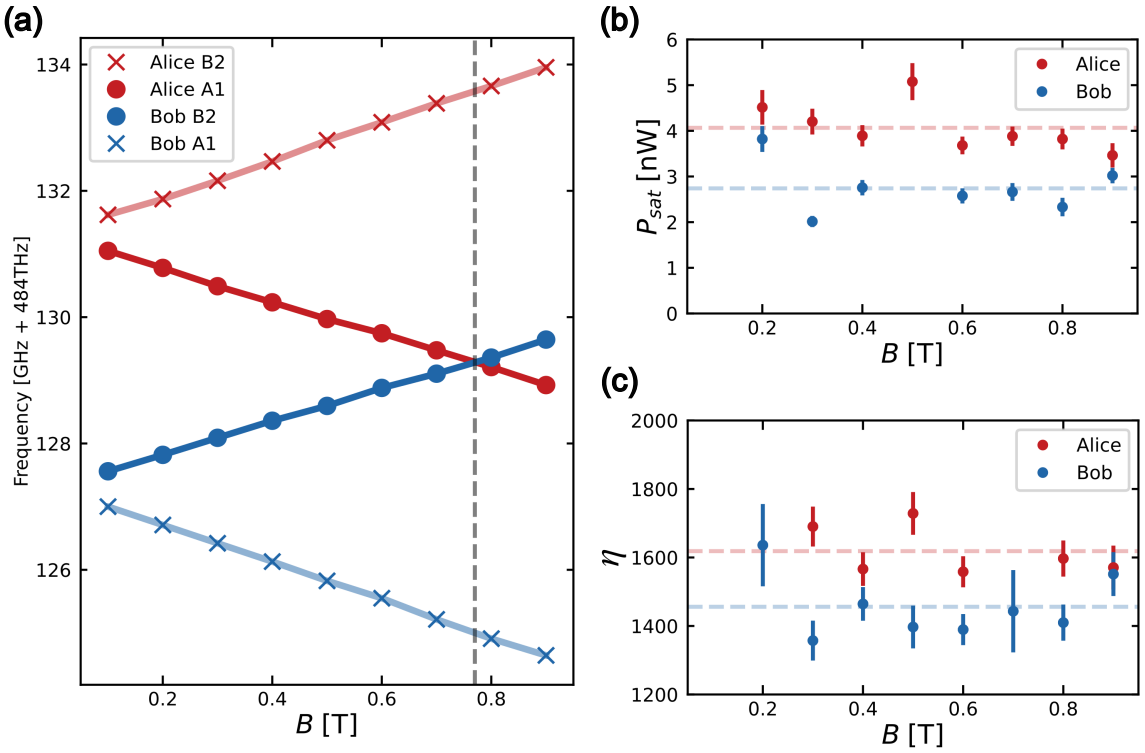

Figure 7.1: Tuning of the optical transitions of two tin-vacancy centers in frequency simultaneously through the strength of an aligned magnetic field. (a) A trace of the transition frequencies of spin-conserving A1 and B2 transitions of the "Alice" and "Bob" defects for a range of magnetic fields. The frequencies are measured by optimizing the PSB collection and varying the excitation frequencies on resonance with the spin-conserving transitions manually. The two emitters have an overlapping transition at a magnetic field of (0.77 ± 0.01) T (as indicated by the gray dashed line). (b) Measurements of the saturation power at each magnetic field strength indicate that the saturation power is unaffected by the magnetic field strength. (c) Measurements of the cyclicity at each magnetic field strength indicate that the cyclicity is also unaffected by the magnetic field strength.

especially close to the lifetime-limit, whereas Bob still has a broadened line. The remaining spectral diffusion will play an essential role in the final indistinguishability of the photons from these two defects. Secondly, one can note that both emitters share the same dipole orientation. While not a strict necessity, this significantly reduces the experimental degree of difficulty for microwave driving the spin transition (which is not necessary for the TPQI experiments, but is essential for the double-click entanglement protocol). Moreover, the fact that we can choose an aligned magnetic field for both emitters also means that both have similar (relatively high) cyclicities and thereby similar initialization times.

Finally, one can note that the two emitters do not have the same central frequency. In the "naive" TPQI protocol that is presented here, it is essential that the frequencies of the photons from both emitters are extremely close. To achieve this, the transitions can be slightly tuned with the magnetic field. Figure 7.1a presents the trace of the two spin-conserving transitions for Alice and Bob under a varying magnetic field strength. The figure clearly shows how the A1 transition of Alice and the B2 transition of Bob can linearly be tuned towards one another with the magnetic field strength. From this measurement, a magnetic field strength of 0.77 ± 0.01 T is found to overlap these two transitions. Figures 7.1b and 7.1c show the measurements of the saturation power and cyclicity at each magnetic field step of Figure 7.1a. There is some fluctuation in the data, which is mostly attributed to the fit qualities of these datapoints. Generally however, the data does not show a clear trend between the magnetic field strength and the cyclicity or saturation power. This experimental confirmation of a fact that is known from theory is useful to verify the feasibility of this magnetic field tuning scheme for entanglement experiments. The splitting rates of both emitters are also expressed in Table 7.1. These splitting rates are comparable previously reported values at aligned magnetic fields in literature [56]. The magnitude of the splitting rate enables a tuning range for each transition of $\Delta f = \pm 2.8$ GHz of the transitions within the constraint of the maximum realizable magnetic field strength of 1T with the current setup.

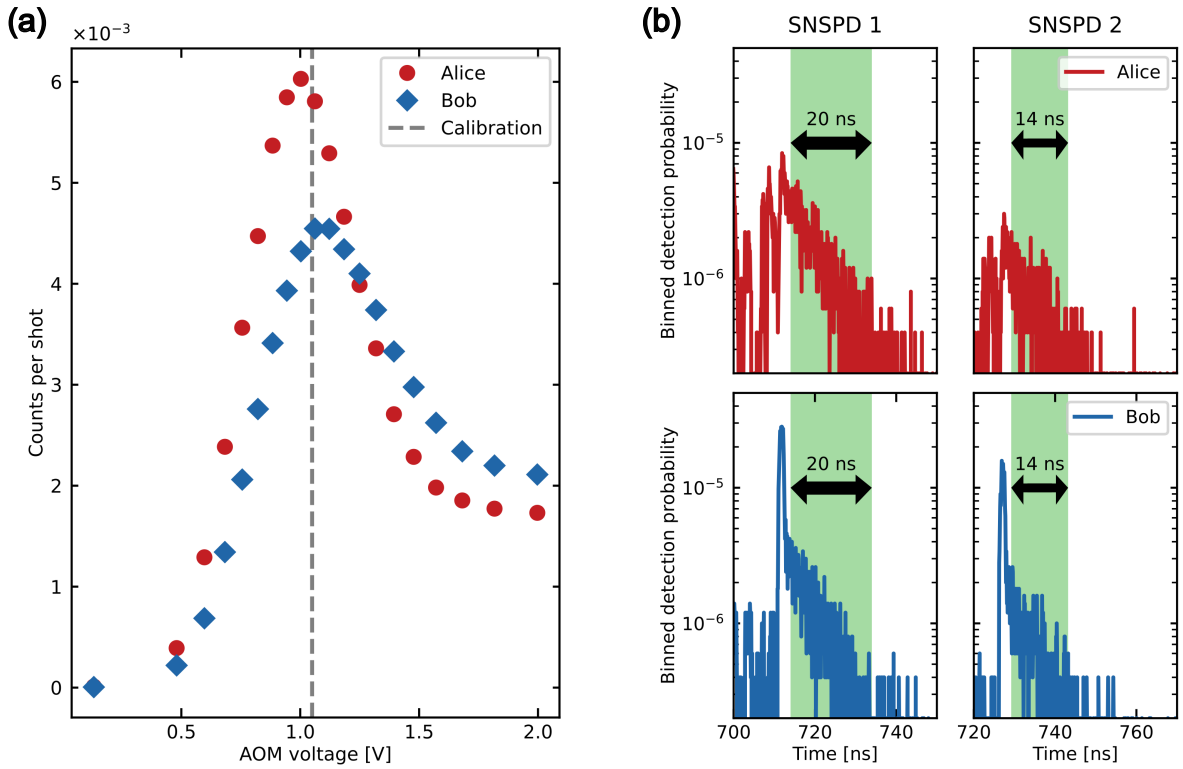

Figure 7.2: Simultaneous coherent optical pulses on two different tin-vacancy centers with a single pulse source. (a) The calibration of the optical pulse power with the AOM opening voltage of the single pulse source for both Alice (red dots) and Bob (blue squares). The datapoints reflect the integrated counts in the PSB collection window of the both emitters respectively. The gray dashed line indicates the chosen optimal working point, which is used in further experiments. (b) A histogram of the detection events in the ZPL paths of both subsetups (top and bottom panels) measured on both SNSPDs (left and right panels). The data is obtained by supplying the calibrated pulse from (a) to one of the two subsetups, while physically blocking the optical path of the other subsetup. The green areas indicate the chosen measurement window sizes of 20 ns on SNSPD 1 and 14 ns on SNSPD 2.

Given the fact that both subsetups share a single optical pulse source, this single pulse must be optimized to be as close as possible to a full π-pulse for both emitters simultaneously. Figure 7.2a shows the integrated counts in the PSB measurement window for different AOM opening voltages of the shared pulse source. Due to careful configuration of the optical paths in the setup, the peak counts of both subsetups are found at almost the same AOM opening voltage, even though both subsetups have different losses in the optical paths and different saturation powers. Figure 7.2a also shows the different PSB collection efficiencies for the two subsetups, which can be explained by slightly different loss channels in the optical paths. For the final experiments, an AOM opening voltage of 1.05 V (indicated by the dashed gray line) was used.

Figure 7.2b shows the histograms of the detection events on both ZPL detectors when the calibrated pi pulse is sent to only one of the two subsetups (Alice in red and Bob in blue). From these measurements, the balance of the emitters can be measured through the counts per shot in the measurement window. Here, these measures for each of the panels in Figure 7.2b is found to be:

1. From Alice to SNSPD 1 (top left): $p_{A\to 1} = (3.4 \pm 0.1) \cdot 10^{-4}$
2. From Alice to SNSPD 2 (top right): $p_{A\to 2} = (1.08 \pm 0.05) \cdot 10^{-4}$
3. From Bob to SNSPD 1 (bottom left): $p_{B\to 1} = (2.4 \pm 0.1) \cdot 10^{-4}$
4. From Bob to SNSPD 2 (top left): $p_{B\to 2} = (1.08 \pm 0.05) \cdot 10^{-4}$

The detection probabilities on SNSPD 2 are always lower than those reported for SNSPD 1 because of a known excess loss in the optical link between fibers after the central beam splitter on that output port. It should also be noted that these values are still low compared to previously reported values in confocal NV experiments [6, 30, 138]. The collection efficiency of ZPL photons is an active area of research. Potential improvements can be made for the fiber-waveguide interface, which is much less efficient in the current lensed coupling method compared to potential adiabatic contact coupling methods (See section 3.3). Moreover, due to the external magnetic field, the cyclicities of both emitters are non-zero (see Figure 7.1c). The experiments in this section are taken with 100 optical pi pulses per initialization, which translates to a decrease of a factor ~0.93 of the expected number of emitted ZPL photons from spin-flipping decay events.

7.2. Experimental demonstration of photon interference

With a proper understanding of the characteristics of both tin-vacancy centers and an accurate way of exciting their optical transitions, the photon interference experiment can be reliably executed. To eventually extract the indistinguishability from the measured contrast, it is crucial to know the $g^{(2)}(0)$ value of both of the single emitters at each point in time during the experiment (since this is required to correct for their noise contributions; see Section 2.2.3). To accomplish this, we perform the Two-Photon Quantum Interference (TPQI) experiment (which involves excitation of both emitters simultaneously) interleaved with single emitter experiments (for which only one of the nodes is excited). More precisely, $5 \cdot 10^7$ repetitions (i.e. optical π-pulses) of the TPQI experiment are followed by $5 \cdot 10^7$ repetitions of the single emitter experiment on Alice's side and then followed by $5 \cdot 10^7$ repetitions on Bob's side. These blocks of experiments are interleaved with calibrations of the EOM bias voltage and cross-polarization. The total dataset consists of 23 repetitions of these blocks of $1.5 \cdot 10^8$ repetitions, for which the data acquisition took around 17 hours.

Figure 7.3 shows the measured coincidences in all combined blocks, histogrammed by the time differences between them. Again, a dip in the zero bin is observed, potentially indicating interference between the photons emitted by Alice and Bob. To quantify the interference, two characteristics can be used: the visibility and indistinguishability. As presented in Section 2.2.3, the visibility is the non-corrected contrast of the zero time difference bin, as compared to the case where the two photons would be fully distinguishable. Using Equation 2.38, a visibility of $V = 0.55 \pm 0.05$ is found for this measurement data. It should be noted that in principle any visibility that is significantly higher than 0 is a sign of photon interference, meaning that this measurement constitutes the first realization of Two-Photon Quantum Interference between photons originating from two distinct tin-vacancy centers.

As noted in Section 2.2.3, the visibility is not a perfect measure for the erasure of which-path information at the beam splitter, since it also contains single emitter noise components in the form of detector clicks that do not originate from a tin-vacancy center. To extract information about the efficiency of the erasure of which-path information for entanglement purposes, the measured visibility can be corrected for these known noise sources to obtain the indistinguishability. From the blocks of single emitter measurements on Alice and Bob, the information about single emitter noise sources can be extracted (see Section 2.2.3). From these measurements, a single emitter $g_A^{(2)}(0) = 0$ is found on Alice's side, whereas a value of $g_B^{(2)}(0) = 0.07 \pm 0.05$ is found on Bob's side. Correcting for the contribution of these noise sources in the zero bin reveals an indistinguishability of $\eta = 0.68 \pm 0.07$.

Given the fact that distinguishability of the photons directly impacts the fidelity in the double-click protocol, it is essential to know what causes the remaining distinguishability. The setup has a locked polarization into the beam splitter with a measured polarization extinction ratio of (28.1 ± 0.9) dB. Therefore, a mismatch in the polarization of the two photons is not expected to be the main cause of distinguishability. From Table 7.1, we can derive that the linewidth of both emitters is still higher than their individual lifetime-limits, especially on Bob's side. This means that there is still a degree of spectral diffusion on both sides, which essentially creates a random offset between the resonance frequencies of both defects.

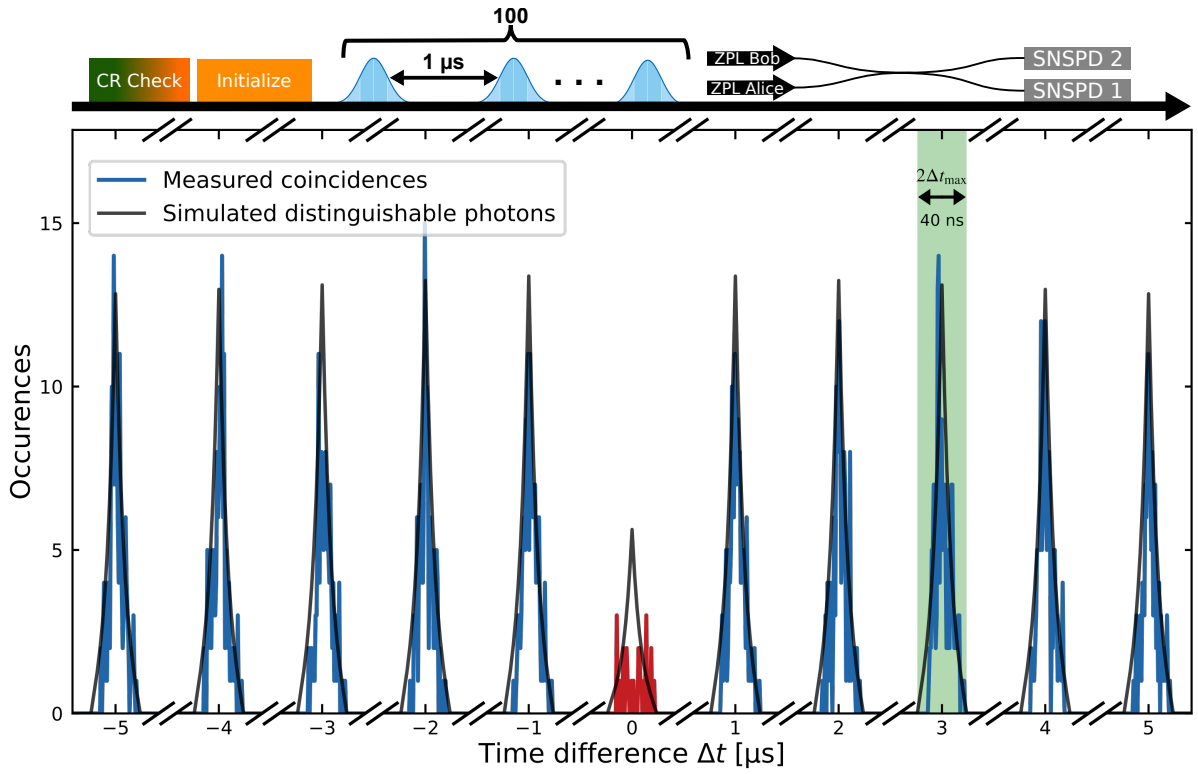

Figure 7.3: Histogram of the time differences between simultaneous detection events at the SNSPDs at the two output arms of the central beam splitter combining ZPL collection paths of Alice and Bob. The blue lines show the occurrences of measured coincidences with a certain time difference, while the black lines show the theoretically predicted coincidences for fully distinguishable photons. The absence of counts in the zero bin (red) compared to the expected number of events for distinguishable photons shows the indistinguishability of these photons, which can be quantified with a visibility of $V = 0.55 \pm 0.05$ and an indistinguishability of $\eta = 0.68 \pm 0.07$. The time-window choice as presented in Figure 7.2b leads to a maximum correlation distance of $\Delta t_{\max} = 20\,\text{ns}$ (as indicated in the green shaded area). The x-axis is broken in order to remove regions without any events, which are caused by the 1 µs delay between each of the 100 π-pulses in each experiment.

7.3. Mitigating the effects of spectral diffusion

The measured visibility of $V = 0.55 \pm 0.05$ in the experiment from the previous section would translate through Equation 2.60 to a maximum obtainable entanglement fidelity of $F_{\max} = 0.77 \pm 0.03$. Given that there are many more expected sources of entanglement infidelity (MW pulse fidelities, optical pulse overlap with different transition, optical double excitation probabilities, etc.), a ceiling of $F_{\max} = 0.77 \pm 0.03$ is quite low. To this end, it is important to analyze the origin of the remaining distinguishability between the photons. More specifically, the knowledge from Section 2.2.2 poses a possible loss channel for photonic indistinguishability: Spectral Diffusion.

Probing the influence of spectral diffusion on the data of Figure 7.3 can be done by leveraging the consequences of the temporal shape of the coincidence events as derived in Appendix B.2 (and illustrated in Figure 2.7b). This relation predicts a dip in the coincidence probability for events within a temporal width that is inversely proportional to the width of the Gaussian spectral diffusion profile (σ). Because of this, the effect of spectral diffusion can be mitigated by temporal filters that only take coincident detection events into account with some maximum allowed time difference ($\Delta t_{\max}$) between them. Figure 7.4a shows the relation between this maximum correlation distance and the measured visibility for the same measured data as presented in Figure 7.3. The figure shows a clear trend of higher visibilities for more stringent temporal filters. The temporal filter with $\Delta t_{\max} = 2.5\,\text{ns}$ leads to a visibility of $V = 0.87 \pm 0.08$, which in turn would translate to a maximum obtainable entanglement fidelity of $F_{max} = 0.94 \pm 0.04$. It should however be noted that strong temporal filtering does pose more stringent conditions on measured data, meaning that the total amount of valid data is

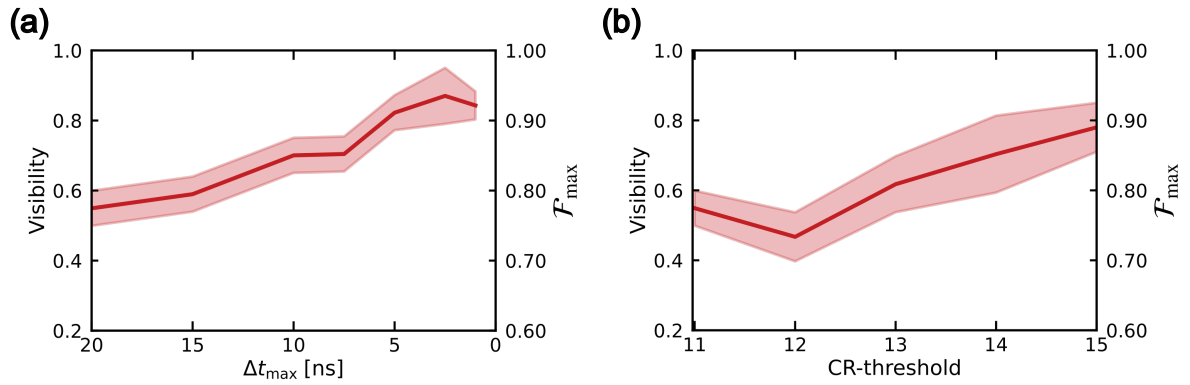

Figure 7.4: Mitigation of spectral diffusion for improvement of the TPQI visibility. (a) The measured TPQI visibility for different values of the maximal correlation distance that is considered. The vertical axis is both plotted in terms of visibility and maximum achievable fidelity (as calculated from Equation 2.60). The area around the data represents the 1σ confidence interval (see Appendix B.3). (b) The measured TPQI visibility and maximum achievable entanglement fidelity for different threshold values of the CR-check that preceeds each block of 100 pulses. The CR-threshold is assumed to be related to the amount of spectral diffusion.

sharply reduced (only 20 % of the coincidences remain at $\Delta t_{\max} = 2.5\,\text{ns}$). For this reason, the errorbars on the data in Figure 7.4a increase sharply after $\Delta t_{\max} = 5\,\text{ns}$. Such a decrease in rate of generating valid data poses a challenge for real-world applications. In summary, Figure 7.4 clearly reveals that spectral diffusion is the main cause of photonic distinguishability in the experiment, but simply posing more stringent conditions on the data is not practical for eventual entanglement generation schemes. This begs the question whether a different spectral diffusion mitigation technique could be leveraged in the experiment.

As presented in Section 3.4, one such technique is the Charge-Resonance check. Even though the exact relation between the CR-threshold and level of spectral diffusion is illusive, an increase of this threshold should always have a mitigating effect on the level of spectral diffusion. Moreover, increasing this threshold only marginally increases the time that the CR-check step takes, but does not influence the amount of available data after the execution of the experiment. In the dataset of Figure 7.3, a CR-check step was already included with a CR-threshold of 11 counts (during a 50 µs probe pulse). Since the measured detections during the probe pulse of the CR-check are recorded, a higher threshold can be set in post-processing by only taking into account measured data of experiments that follow a CR-check with a certain number of counts. Figure 7.4b explores the relation between the measured visibility and this CR-threshold. Apart from the unexplained dip at a threshold of 12, the data shows a clear increase in visibility with more stringent thresholds. It should be noted that all datapoints in Figure 7.4b are taken at $\tau_{max} = 20\,\text{ns}$ in order to have enough data for meaningful analysis. At a CR-threshold of 15, a visibility of $V = 0.78 \pm 0.09$ is measured, which corresponds to a maximum entanglement fidelity of $F_{max} = 0.89 \pm 0.05$.

In summary, the results of this section suffice as proof that mitigation of spectral diffusion should be the main focus for improving the measured visibility. The influence of varying the maximum correlation distance and CR-threshold were analyzed here separately as initial attempts at such mitigation techniques. The results from this analysis show that both techniques have favorable effects on the measured visibility. Most likely, a combination of both techniques optimizes the measured visibility, but more experimental data is required to prove this. Finally, the two tin-vacancy centers that were described in Section 7.1 were chosen without an extensive analysis of their spectral diffusion magnitudes. Preselecting on tin-vacancy centers with less inherent spectral diffusion might relax the required post-selection of data, thereby making the effective generation of TPQI data more efficient. Moreover, the measured visibilities in this section are always also limited by the finite probabilities of dark count detections in the measurement windows. Mitigation of the noise sources of these noisy detections (laser leakage, detector dark counts, etc.) should also be investigated as a possible avenue for improving the visibility of the Two-Photon Quantum Interference.

8 Conclusion & Outlook

8.1. Conclusion

The main goal of the work in this thesis was to (i) demonstrate the combination of required experimental capabilities for remote entanglement generation of two tin-vacancy centers in a single setup and (ii) demonstrate indistinguishability of photons generated by two distinct tin-vacancy centers. From an analysis of the envisioned "double-click" entanglement generation protocol, the following experimental requirements are derived to be essential control capabilities:

1. Coherent control over an optical transitions of both tin-vacancy centers on a single-photon level, including the capability of applying coherent optical π-pulses that lead to emission and detection of single photons.

2. Initialization and readout capabilities leveraging the cyclic nature of the optical transitions at non-zero magnetic fields.

3. Coherent control of the spin state of the tin-vacancy center, including preserved coherence of this state during the time it takes to generate entanglement.

4. The reliable and stable emission of transform-limited indistinguishable photons from two different tin-vacancies.

To experimentally demonstrate these capabilities in an entanglement-compatible fashion, a setup is required that has the ability to simultaneously control two tin-vacancy centers within a single cryostat. The setup is required to have control over all degrees of freedom of the two tin-vacancy centers independently. The proposed setup in this work (as presented in Chapter 3) fulfills these requirements in all but two control knobs: the static magnetic field and optical π-pulse are shared resources for the two tin-vacancy centers. The shared magnetic field is a deliberate design choice and poses only small experimental restrictions (which largely outweigh the experimental overhead of operating two different cryogenic systems). On the other hand, the addition of independent optical π-pulses on both subsystems is one of the main suggested improvements for the near-future.

The reliability of the setup was first demonstrated through a characterization of the optical transitions of the tin-vacancy centers in waveguides (Chapter 4). These characterizations showed the ability of the setup to measure near-lifetime-limited linewidths of single emitters in a spectrally crowded waveguide, while collecting ~(1-2)% of their emitted photons. The characterization also showed the response of the optical transitions of these emitters to an external magnetic field, which was in agreement with the predictions from the theoretically derived system Hamiltonian and could be used as an initial characterization of the strain regime of these emitters. The results at non-zero magnetic fields also gave initial indications of the available tuning range of the transition frequencies with the magnitude of the external magnetic field.

The first capability that was demonstrated in this work is the ability to coherently control the spin-state of tin-vacancy centers in different strain regimes (Chapter 5). A prerequisite for this capability is the ability to initialize and readout the state of the spin. Both of these capabilities are realized by cycling a spin-conserving transition. Initialization could be done in $\sim 200\,\mu s$ due to the measured cyclicity of $(1.9 \pm 0.1) \cdot 10^3$ of the spin-conserving transition. Readout of the spin state is technically more challenging and was demonstrated here in a single-shot fashion with an average fidelity of $(92.4 \pm 0.2)\,\%$, which marks the highest-fidelity experimental realization of single-shot readout with tin-vacancy centers in literature [37, 121, 124, 125]. The initialization and single-shot readout capabilities were subsequently leveraged in experiments involving coherent control over the tin-vacancy center's electronic spin-1/2 system. The electron spin dynamics are highly dependent on the level of strain in the lattice. The experimental results showed control over the spin state for a low- and medium-strain regime, with a clear observation of more efficient microwave driving for the medium-strain regime as measured by a π-pulse fidelity of $F_\pi = 0.980 \pm 0.002$ for the medium-strain versus $F_\pi = 0.871 \pm 0.006$ for the low-strained emitter. The pulse fidelity in the low-strain regime is limiting for entanglement schemes and is therefore a relevant area for future investigations. Moreover, the decoherence time of $(47 \pm 2)\,\mu s$ for the medium-strain emitter is found to be relatively low. This decoherence time is however not a fundamental limit of the setup, as demonstrated by the $(316 \pm 3)\,\mu s$ decoherence time of the low-strain emitter, which is in turn relatively high compared to other reported values in literature [49, 52, 56].

After demonstrating coherent spin control capabilities, the optical control of the tin-vacancy center at the single-photon level is explored in Chapter 6. To demonstrate this experimental capability, an optical π-pulse was calibrated with ensembles of measurements of single-photons from the both the Zero-Phonon Line (ZPL) and Phonon Sideband (PSB) transitions. The single-photon nature of the recorded detection events upon resonant excitation was demonstrated by a measurement of coincidences between detectors at the output ports of a Hanbury-Brown-Twiss interferometer. These detection events showed a normalized autocorrelation of $g^{(2)}(0) = 0.06 \pm 0.03$, which is sufficiently low to prove the single-photon nature of the detection events.

The relatively low $g^{(2)}(0)$ value is a crucial requirement for experiments of the correlations between photons originating from two distinct emitters (Chapter 7). During these experiments, the setup is utilized to its full extent to demonstrate control over two tin-vacancy centers independently. The setup is calibrated to have two emitters with spectrally overlapping transitions, which are then simultaneously excited by optical π-pulses. This causes both tin-vacancy centers to emit single-photons towards a central beam splitter connecting the two ZPL collection paths. The indistinguishability of the photons that are created by the two subsystems is verified by an absence of coincident detection events at two single-photon detectors on the output ports of the beam splitter. An analysis of the measured correlation between detection events reveals a visibility of $V = 0.55 \pm 0.05$, which can be corrected for the known $g^{(2)}(0)$ values of the single emitters to find an indistinguishability of $\eta = 0.68 \pm 0.07$. This measurement constitutes the first measured interference between photons generated by two distinct tin-vacancy centers. The remaining distinguishability is attributed to spectral diffusion, the effect of which was shown to be reducible through either time-filtering or more stringent thresholds on the required charge-resonance, which need to be met before attempting the experiment. With this additional filtering, a maximum visibility of $V = 0.87 \pm 0.08$ was shown to be experimentally achievable.

Summarizing, these results demonstrate the required control elements for entanglement generation through the "double-click" protocol. The measured indistinguishability without additional filtering puts a limit on the maximum achievable entanglement fidelity of $F_{\text{max}} = 0.77 \pm 0.03$. If additional temporal filtering is considered, then this maximum fidelity increases to $F_{\text{max}} = 0.94 \pm 0.04$. Combining the measured time durations of the individual elements of the double-click protocol, an entanglement generation rate of roughly 5-10 mHz is predicted if experiments are done in the current configuration. Both the rate and fidelity of the predicted entanglement generation are not novelties in the field of color centers, but already outperform the first entanglement experiments with NV centers [30]. Combined with the known areas of potential improvement in the current setup, this forecasts a bright future for research on the tin-vacancy center.

8.2. Outlook

This work shows exciting prospects for future research on the tin-vacancy platform. In the near-future, the results do not show any physical restrictions that would prevent entanglement generation with the current setup configuration. The main focus in the near-future should therefore be to achieve this demonstration with the "double-click" protocol. After initial demonstrations of tin-vacancy entanglement, the focus of innovation can be in a few general directions.

Firstly, it should be noted that there is still room for improvement in the current setup. The fiber-waveguide coupling, microwave driving efficiency and initialization times are the most obvious candidates for improvement. Fiber-waveguide coupling can be improved by a thorough investigation of fiber-gluing schemes [117], which might enable stabilized adiabatic coupling between the fiber and waveguide [113]. In the near-future, the microwave driving efficiency can be improved by only considering emitters with a relatively high level of strain. In the long-term future however, the field of hybrid integration can be explored to design chips with microwave delivery lines much closer to the defects [52, 56, 60]. Finally, the initialization time poses the most significant limit on the entanglement generation rate. Decreasing the initialization time by investigating Measurement-Based Initialization schemes [37, 139, 140], optical Raman driving processes [121] or optically addressing spin-flipping transitions should be a high-priority.

A second area of research that can still be explored revolves around additional capabilities in the setup. Firstly, the addition of independent optical π-pulses for both nodes in the setup should be actively pursued in the imminent-future. The addition of a second pulse path will benefit the amount of available power in the optical π-pulses, which creates more flexibility in the cross-polarization scheme. A second source of optical π-pulses will also enable direct measurements of the visibility by unlocking the capability of generating distinguishable photons (something that is not easily doable in the current configuration). Moreover, a large part of the time on this work was spent on finding two tin-vacancy centers in different waveguides that could be tuned to have overlapping transitions with a 1T magnetic field. This "luck-based" approach is definitely not scalable and should be seen as an initial stepping stone. Improvements in this regard can be made by enabling on-chip resonance tuning through deterministically controllable strain [60, 141] or by shifting the wavelength of collected photons to telecom wavelengths with Quantum Frequency Conversion [42, 47].

The field of research on the tin-vacancy center enters a highly exciting stage, in which the more developed fundamental understanding of the system dynamics can be leveraged for demonstrations with practical utility. A highly-promising research direction for the tin-vacancy center concerns hybrid integration of the color center with foundry-scale photonics [142] and CMOS electronics [60]. The creation of a device with on-chip excitation, photon routing, filtering and detection can pave the way for exciting applications outside of the controlled environments in experimental setups. A second exciting research direction is the improvement of photon emission efficiencies of tin-vacancy centers through their integration in cavities [53]. The enhancement of detection efficiencies from this approach can allow much faster entanglement generation rates, which pave the way for many quantum network applications. Finally, the integration of tin-vacancy based quantum nodes with existing optical infrastructure should be considered as an opportunity for the creation of an early-stage testbed for a metropolitan-scale Quantum Network. The realization of such a network can prove extremely useful for research on applications, while providing many insights into important areas of research for other platforms.

References

[1] J. Ding, "Discussion on the Development Trend of Computer Science and Technology," in *ResearchGate*, Sout Korea: SPG Open Access Journals, Jan. 2016. DOI: 10.2991/emcs-16.2016.309. (visited on 11/24/2024).

[2] P. A. Packan, "Pushing the Limits," *Science*, vol. 285, no. 5436, pp. 2079–2081, Sep. 1999. DOI: 10.1126/science.285.5436.2079. (visited on 11/24/2024).

[3] I. L. Markov, "Limits on fundamental limits to computation," *Nature*, vol. 512, no. 7513, pp. 147–154, Aug. 2014, ISSN: 1476-4687. DOI: 10.1038/nature13570. (visited on 11/24/2024).

[4] Z. Lehman, "Global Computing Capacity: An Empirical Frame Work for 2023," 2023. DOI: 10.36227/techrxiv.24188670.v1. (visited on 11/24/2024).

[5] D. J. Griffiths and D. F. Schroeter, *Introduction to Quantum Mechanics*, 3rd ed. Cambridge University Press, 2017, ISBN: 978-1-108-10314-5.

[6] B. Hensen *et al.*, "Loophole-free Bell inequality violation using electron spins separated by 1.3 kilometres," *Nature*, vol. 526, no. 7575, pp. 682–686, Oct. 2015, ISSN: 1476-4687. DOI: 10.1038/nature15759. (visited on 11/22/2024).

[7] A. Hassan and A. Ibrahim, "The Coming Quantum Computing Evolution in the Pharmaceutical Industry and Drug R&D," *ResearchBerg Review of Science and Technology*, vol. 3, no. 11, pp. 1–16, Nov. 2023. (visited on 11/28/2024).

[8] M. Zinner, F. Dahlhausen, P. Boehme, J. Ehlers, L. Bieske, and L. Fehring, "Toward the institutionalization of quantum computing in pharmaceutical research," *Drug Discovery Today*, vol. 27, no. 2, pp. 378–383, Feb. 2022, ISSN: 1359-6446. DOI: 10.1016/j.drudis.2021.10.006. (visited on 11/28/2024).

[9] B. Bauer, S. Bravyi, M. Motta, and G. K.-L. Chan, "Quantum Algorithms for Quantum Chemistry and Quantum Materials Science," *Chemical Reviews*, vol. 120, no. 22, pp. 12 685–12 717, Nov. 2020, ISSN: 0009-2665. DOI: 10.1021/acs.chemrev.9b00829. (visited on 11/28/2024).

[10] A. Abbas *et al.*, "Challenges and opportunities in quantum optimization," *Nature Reviews Physics*, vol. 6, no. 12, pp. 718–735, Dec. 2024, ISSN: 2522-5820. DOI: 10.1038/s42254-024-00770-9. (visited on 11/28/2024).

[11] S. Wehner, D. Elkouss, and R. Hanson, "Quantum internet: A vision for the road ahead," *Science*, vol. 362, eaam9288, Oct. 2018. DOI: 10.1126/science.aam9288.

[12] N. Gisin and R. Thew, "Quantum communication," *Nature Photonics*, vol. 1, no. 3, pp. 165–171, Mar. 2007, ISSN: 1749-4893. DOI: 10.1038/nphoton.2007.22. (visited on 11/28/2024).

[13] D. Barral *et al.*, *Review of Distributed Quantum Computing. From single QPU to High Performance Quantum Computing*, Apr. 2024. DOI: 10.48550/arXiv.2404.01265. arXiv: 2404.01265. (visited on 11/28/2024).

[14] R. Bedington, J. M. Arrazola, and A. Ling, "Progress in satellite quantum key distribution," *npj Quantum Information*, vol. 3, no. 1, pp. 1–13, Aug. 2017, ISSN: 2056-6387. DOI: 10.1038/s41534-017-0031-5. (visited on 11/28/2024).

[15] *Quantum Internet Alliance | Building a Global Quantum Internet Made in Europe*, https://quantuminternetalliance.org/. (visited on 11/28/2024).

[16] D. E. Chang, V. Vuletić, and M. D. Lukin, "Quantum nonlinear optics — photon by photon," *Nature Photonics*, vol. 8, no. 9, pp. 685–694, Sep. 2014, ISSN: 1749-4893. DOI: 10.1038/nphoton.2014.192. (visited on 11/24/2024).

[17] J. Marcus, "Internet hardware and software," in *Professional Program Proceedings. ELECTRO '96*, Apr. 1996, pp. 215–221. DOI: 10.1109/ELECTR.1996.501230. (visited on 11/24/2024).

[18] C. D. Bruzewicz, J. Chiaverini, R. McConnell, and J. M. Sage, "Trapped-ion quantum computing: Progress and challenges," *Applied Physics Reviews*, vol. 6, no. 2, p. 021 314, May 2019, ISSN: 1931-9401. DOI: 10.1063/1.5088164. (visited on 11/28/2024).

[19] J. Zhang *et al.*, "Observation of a many-body dynamical phase transition with a 53-qubit quantum simulator," *Nature*, vol. 551, no. 7682, pp. 601–604, Nov. 2017, ISSN: 1476-4687. DOI: 10.1038/nature24654. (visited on 11/28/2024).

[20] S. A. Moses *et al.*, "A Race-Track Trapped-Ion Quantum Processor," *Physical Review X*, vol. 13, no. 4, p. 041 052, Dec. 2023. DOI: 10.1103/PhysRevX.13.041052. (visited on 11/28/2024).

[21] C. Monroe and J. Kim, "Scaling the Ion Trap Quantum Processor," *Science*, vol. 339, no. 6124, pp. 1164–1169, Mar. 2013. DOI: 10.1126/science.1231298. (visited on 11/28/2024).

[22] V. Krutyanskiy *et al.*, "Entanglement of Trapped-Ion Qubits Separated by 230 Meters," *Physical Review Letters*, vol. 130, no. 5, p. 050 803, Feb. 2023. DOI: 10.1103/PhysRevLett.130.050803. (visited on 06/17/2024).

[23] L. J. Stephenson *et al.*, "High-Rate, High-Fidelity Entanglement of Qubits Across an Elementary Quantum Network," *Physical Review Letters*, vol. 124, no. 11, p. 110 501, Mar. 2020. DOI: 10.1103/PhysRevLett.124.110501. (visited on 12/02/2024).

[24] T. van Leent *et al.*, "Entangling single atoms over 33 km telecom fibre," *Nature*, vol. 607, no. 7917, pp. 69–73, Jul. 2022, ISSN: 1476-4687. DOI: 10.1038/s41586-022-04764-4. (visited on 12/02/2024).

[25] "IBM Unveils 400 Qubit-Plus Quantum Processor and Next-Generation IBM Quantum System Two," *IBM Newsroom*, (visited on 11/28/2024).

[26] Y. Yu *et al.*, "Telecom-band quantum dot technologies for long-distance quantum networks," *Nature Nanotechnology*, vol. 18, no. 12, pp. 1389–1400, Dec. 2023, ISSN: 1748-3395. DOI: 10.1038/s41565-023-01528-7. (visited on 11/28/2024).

[27] A. Delteil, Z. Sun, W.-b. Gao, E. Togan, S. Faelt, and A. Imamoğlu, "Generation of heralded entanglement between distant hole spins," *Nature Physics*, vol. 12, no. 3, pp. 218–223, Mar. 2016, ISSN: 1745-2481. DOI: 10.1038/nphys3605. (visited on 12/02/2024).

[28] R. Stockill *et al.*, "Phase-Tuned Entangled State Generation between Distant Spin Qubits," *Physical Review Letters*, vol. 119, no. 1, p. 010 503, Jul. 2017. DOI: 10.1103/PhysRevLett.119.010503. (visited on 12/02/2024).

[29] A. Laneve *et al.*, *Quantum teleportation with dissimilar quantum dots over a hybrid quantum network*, Nov. 2024. DOI: 10.48550/arXiv.2411.12387. arXiv: 2411.12387. (visited on 11/28/2024).

[30] H. Bernien *et al.*, "Heralded entanglement between solid-state qubits separated by three metres," *Nature*, vol. 497, no. 7447, pp. 86–90, May 2013, ISSN: 1476-4687. DOI: 10.1038/nature12016. (visited on 03/05/2024).

[31] M. Pompili *et al.*, "Realization of a multinode quantum network of remote solid-state qubits," *Science*, vol. 372, no. 6539, pp. 259–264, Apr. 2021. DOI: 10.1126/science.abg1919. (visited on 03/12/2024).

[32] F. Afzal *et al.*, *Distributed Quantum Computing in Silicon*, Jun. 2024. arXiv: 2406.01704 [quant-ph]. (visited on 06/17/2024).

[33] C. M. Knaut *et al.*, *Entanglement of Nanophotonic Quantum Memory Nodes in a Telecommunication Network*, Oct. 2023. arXiv: 2310.01316 [quant-ph]. (visited on 03/05/2024).

[34] A. Ruskuc, C.-J. Wu, E. Green, S. L. N. Hermans, J. Choi, and A. Faraon, *Scalable Multipartite Entanglement of Remote Rare-earth Ion Qubits*, Feb. 2024. DOI: 10.48550/arXiv.2402.16224. arXiv: 2402.16224. (visited on 12/01/2024).

[35] C. E. Bradley *et al.*, "A Ten-Qubit Solid-State Spin Register with Quantum Memory up to One Minute," *Physical Review X*, vol. 9, no. 3, p. 031 045, Sep. 2019, ISSN: 2160-3308. DOI: 10.1103/PhysRevX.9.031045. (visited on 03/06/2024).

[36] G. L. van de Stolpe *et al.*, "Mapping a 50-spin-qubit network through correlated sensing," *Nature Communications*, vol. 15, no. 1, p. 2006, Mar. 2024, ISSN: 2041-1723. DOI: 10.1038/s41467-024-46075-4. (visited on 11/21/2024).

[37] H. K. C. Beukers *et al.*, *Control of solid-state nuclear spin qubits using an electron spin-1/2*, Sep. 2024. DOI: 10.48550/arXiv.2409.08977. arXiv: 2409.08977. (visited on 10/10/2024).

[38] A. Bourassa *et al.*, "Entanglement and control of single nuclear spins in isotopically engineered silicon carbide," *Nature Materials*, vol. 19, no. 12, pp. 1319–1325, Dec. 2020, ISSN: 1476-4660. DOI: 10.1038/s41563-020-00802-6. (visited on 12/01/2024).

[39] J. Wang *et al.*, "Coherence times of precise depth controlled NV centers in diamond," *Nanoscale*, vol. 8, no. 10, pp. 5780–5785, 2016. DOI: 10.1039/C5NR08690F. (visited on 11/28/2024).

[40] A. M. Zaitsev, *Optical Properties of Diamond*. Berlin, Heidelberg: Springer, 2001, ISBN: 978-3-662-04548-0. DOI: 10.1007/978-3-662-04548-0. (visited on 11/19/2024).

[41] M. Pompili, "Multi-Node Quantum Networks with Diamond Qubits," Ph.D. dissertation, Delft University of Technology, 2021. DOI: 10.4233/UUID:B125EC2D-E2AF-4708-BCCC-0A2357A533B1. (visited on 11/14/2024).

[42] A. J. Stolk *et al.*, "Metropolitan-scale heralded entanglement of solid-state qubits," *Science Advances*, vol. 10, no. 44, eadp6442, Oct. 2024. DOI: 10.1126/sciadv.adp6442. (visited on 11/21/2024).

[43] M. Iuliano *et al.*, "Qubit teleportation between a memory-compatible photonic time-bin qubit and a solid-state quantum network node," *npj Quantum Information*, vol. 10, no. 1, pp. 1–7, Nov. 2024, ISSN: 2056-6387. DOI: 10.1038/s41534-024-00910-0. (visited on 11/21/2024).

[44] C. Bradac, W. Gao, J. Forneris, M. E. Trusheim, and I. Aharonovich, "Quantum nanophotonics with group IV defects in diamond," *Nature Communications*, vol. 10, no. 1, p. 5625, Dec. 2019, ISSN: 2041-1723. DOI: 10.1038/s41467-019-13332-w. (visited on 11/28/2024).

[45] A. Sipahigil *et al.*, "Indistinguishable Photons from Separated Silicon-Vacancy Centers in Diamond," *Physical Review Letters*, vol. 113, no. 11, p. 113 602, Sep. 2014. DOI: 10.1103/PhysRevLett.113.113602. (visited on 11/22/2024).

[46] C. Hepp, "Electronic structure of the silicon vacancy color center in diamond," doctoralThesis, 2014. DOI: 10.22028/D291-23020. (visited on 11/15/2024).

[47] E. Bersin *et al.*, "Telecom Networking with a Diamond Quantum Memory," *PRX Quantum*, vol. 5, no. 1, p. 010 303, Jan. 2024. DOI: 10.1103/PRXQuantum.5.010303. (visited on 11/22/2024).

[48] P.-J. Stas *et al.*, "Robust multi-qubit quantum network node with integrated error detection," *Science*, vol. 378, no. 6619, pp. 557–560, Nov. 2022. DOI: 10.1126/science.add9771. (visited on 11/28/2024).

[49] E. I. Rosenthal *et al.*, "Microwave Spin Control of a Tin-Vacancy Qubit in Diamond," *Physical Review X*, vol. 13, no. 3, p. 031 022, Aug. 2023, ISSN: 2160-3308. DOI: 10.1103/PhysRevX.13.031022. (visited on 03/04/2024).

[50] M. E. Trusheim *et al.*, "Transform-Limited Photons From a Coherent Tin-Vacancy Spin in Diamond," *Physical Review Letters*, vol. 124, no. 2, p. 023 602, Jan. 2020. DOI: 10.1103/PhysRevLett.124.023602. (visited on 03/07/2024).

[51] T. Iwasaki *et al.*, "Tin-Vacancy Quantum Emitters in Diamond," *Physical Review Letters*, vol. 119, no. 25, p. 253 601, Dec. 2017. DOI: 10.1103/PhysRevLett.119.253601. (visited on 06/11/2024).

[52] I. Karapatzakis *et al.*, *Microwave Control of the Tin-Vacancy Spin Qubit in Diamond with a Superconducting Waveguide*, Mar. 2024. arXiv: 2403.00521 [quant-ph]. (visited on 03/07/2024).

[53] Y. Herrmann *et al.*, "Coherent Coupling of a Diamond Tin-Vacancy Center to a Tunable Open Microcavity," *Physical Review X*, vol. 14, no. 4, p. 041 013, Oct. 2024. DOI: 10.1103/PhysRevX.14.041013. (visited on 11/21/2024).

[54] M. Pasini *et al.*, *Nonlinear Quantum Photonics with a Tin-Vacancy Center Coupled to a One-Dimensional Diamond Waveguide*, Nov. 2023. DOI: 10.48550/arXiv.2311.12927. arXiv: 2311.12927 [quant-ph]. (visited on 03/08/2024).

[55] R. A. Parker *et al.*, "A diamond nanophotonic interface with an optically accessible deterministic electronuclear spin register," *Nature Photonics*, vol. 18, no. 2, pp. 156–161, Feb. 2024, ISSN: 1749-4893. DOI: 10.1038/s41566-023-01332-8. (visited on 11/20/2024).

[56] X. Guo *et al.*, "Microwave-Based Quantum Control and Coherence Protection of Tin-Vacancy Spin Qubits in a Strain-Tuned Diamond-Membrane Heterostructure," *Physical Review X*, vol. 13, no. 4, p. 041 037, Nov. 2023. DOI: 10.1103/PhysRevX.13.041037. (visited on 03/08/2024).

[57] J. M. Brevoord *et al.*, *Heralded initialization of charge state and optical transition frequency of diamond tin-vacancy centers*, Nov. 2023. arXiv: 2311.11962 [quant-ph]. (visited on 05/02/2024).

[58] G. Pieplow *et al.*, *Quantum Electrometer for Time-Resolved Material Science at the Atomic Lattice Scale*, Jan. 2024. DOI: 10.48550/arXiv.2401.14290. arXiv: 2401.14290 [cond-mat, physics:physics, physics:quant-ph]. (visited on 05/23/2024).

[59] J.-L. Liu *et al.*, "Creation of memory–memory entanglement in a metropolitan quantum network," *Nature*, vol. 629, no. 8012, pp. 579–585, May 2024, ISSN: 1476-4687. DOI: 10.1038/s41586-024-07308-0. (visited on 12/03/2024).

[60] L. Li *et al.*, "Heterogeneous integration of spin–photon interfaces with a CMOS platform," *Nature*, pp. 1–7, May 2024, ISSN: 1476-4687. DOI: 10.1038/s41586-024-07371-7. (visited on 06/04/2024).

[61] A. E. Rugar *et al.*, "Narrow-Linewidth Tin-Vacancy Centers in a Diamond Waveguide," *ACS Photonics*, vol. 7, no. 9, pp. 2356–2361, Sep. 2020. DOI: 10.1021/acsphotonics.0c00833. (visited on 11/22/2024).

[62] J. Görlitz *et al.*, "Coherence of a charge stabilised tin-vacancy spin in diamond," *npj Quantum Information*, vol. 8, no. 1, pp. 1–9, Apr. 2022, ISSN: 2056-6387. DOI: 10.1038/s41534-022-00552-0. (visited on 11/14/2024).

[63] L. Cheng, S. Zhu, X. Ouyang, and W. Zheng, "Bandgap evolution of diamond," *Diamond and Related Materials*, vol. 132, p. 109 638, Feb. 2023, ISSN: 0925-9635. DOI: 10.1016/j.diamond.2022.109638. (visited on 11/19/2024).

[64] J. R. de Laeter *et al.*, "Atomic weights of the elements. Review 2000 (IUPAC Technical Report)," *Pure and Applied Chemistry*, vol. 75, no. 6, pp. 683–800, Jan. 2003, ISSN: 1365-3075. DOI: 10.1351/pac200375060683. (visited on 11/28/2024).

[65] T. Hom, W. Kiszenik, and B. Post, "Accurate lattice constants from multiple reflection measurements. II. Lattice constants of germanium silicon, and diamond," *Journal of Applied Crystallography*, vol. 8, no. 4, pp. 457–458, 1975, ISSN: 1600-5767. DOI: 10.1107/S0021889875010965. (visited on 11/28/2024).

[66] P. Hohenberg and W. Kohn, "Inhomogeneous Electron Gas," *Physical Review*, vol. 136, no. 3B, B864–B871, Nov. 1964. DOI: 10.1103/PhysRev.136.B864. (visited on 12/03/2024).

[67] G. Thiering and A. Gali, "*Ab Initio* Magneto-Optical Spectrum of Group-IV Vacancy Color Centers in Diamond," *Physical Review X*, vol. 8, no. 2, p. 021 063, Jun. 2018, ISSN: 2160-3308. DOI: 10.1103/PhysRevX.8.021063. (visited on 11/14/2024).

[68] Jinest, *Diamond and Multi element structures*, https://blog.naver.com/jinest/70134698798, Blog, Mar. 2012. (visited on 12/03/2024).

[69] G. Pieplow, M. Belhassen, and T. Schröder, *Efficient Microwave Spin Control of Negatively Charged Group-IV Color Centers in Diamond*, Mar. 2024. arXiv: 2312.02637 [quant-ph]. (visited on 03/07/2024).

[70] H. A. Jahn, E. Teller, and F. G. Donnan, "Stability of polyatomic molecules in degenerate electronic states - I—Orbital degeneracy," *Proceedings of the Royal Society of London. Series A - Mathematical and Physical Sciences*, vol. 161, no. 905, pp. 220–235, Jan. 1997. DOI: 10.1098/rspa.1937.0142. (visited on 11/14/2024).

[71] *CODATA Value: Electron gyromagnetic ratio*, https://physics.nist.gov/cgi-bin/cuu/Value?gammae, 2022. (visited on 12/02/2024).

[72] K. D. Jahnke *et al.*, "Electron–phonon processes of the silicon-vacancy centre in diamond," *New Journal of Physics*, vol. 17, no. 4, p. 043 011, Apr. 2015, ISSN: 1367-2630. DOI: 10.1088/1367-2630/17/4/043011. (visited on 11/14/2024).

[73] E. Fermi, *Nuclear Physics*. University of Chicago Press, 1950, vol. 2, ISBN: 978-0-226-24365-8.

[74] Y. Jin, M. Govoni, and G. Galli, "Vibrationally resolved optical excitations of the nitrogen-vacancy center in diamond," *npj Computational Materials*, vol. 8, no. 1, pp. 1–9, Nov. 2022, ISSN: 2057-3960. DOI: 10.1038/s41524-022-00928-y. (visited on 11/28/2024).

[75] J. Görlitz *et al.*, "Spectroscopic investigations of negatively charged tin-vacancy centres in diamond," *New Journal of Physics*, vol. 22, no. 1, p. 013 048, Jan. 2020, ISSN: 1367-2630. DOI: 10.1088/1367-2630/ab6631. (visited on 06/04/2024).

[76] A. E. Rugar *et al.*, "Quantum Photonic Interface for Tin-Vacancy Centers in Diamond," *Physical Review X*, vol. 11, no. 3, p. 031 021, Jul. 2021. DOI: 10.1103/PhysRevX.11.031021. (visited on 06/04/2024).

[77] C. Santori, P. E. Barclay, K.-M. C. Fu, R. G. Beausoleil, S. Spillane, and M. Fisch, "Nanophotonics for quantum optics using nitrogen-vacancy centers in diamond," *Nanotechnology*, vol. 21, no. 27, p. 274 008, Jun. 2010, ISSN: 0957-4484. DOI: 10.1088/0957-4484/21/27/274008. (visited on 11/29/2024).

[78] J. N. Becker and C. Becher, "Coherence Properties and Quantum Control of Silicon Vacancy Color Centers in Diamond," *physica status solidi (a)*, vol. 214, no. 11, p. 1 700 586, 2017, ISSN: 1862-6319. DOI: 10.1002/pssa.201700586. (visited on 06/16/2024).

[79] R. Høy Jensen *et al.*, "Cavity-Enhanced Photon Emission from a Single Germanium-Vacancy Center in a Diamond Membrane," *Physical Review Applied*, vol. 13, no. 6, p. 064 016, Jun. 2020. DOI: 10.1103/PhysRevApplied.13.064016. (visited on 11/28/2024).

[80] R. Loudon and R. Loudon, *The Quantum Theory of Light*, Third Edition, Third Edition. Oxford, New York: Oxford University Press, Sep. 2000, ISBN: 978-0-19-850176-3.

[81] A. Einstein, "Zur Quantentheorie der Strahlung," *Quantentheorie: Einführung und Originaltexte*, pp. 121–128, 1917. DOI: 10.1515/9783112596609-016. (visited on 11/15/2024).

[82] D. P. DiVincenzo, *Topics in Quantum Computers*, Dec. 1996. DOI: 10.48550/arXiv.cond-mat/9612126. arXiv: cond-mat/9612126. (visited on 11/29/2024).

[83] A. Reiserer, "Colloquium: Cavity-enhanced quantum network nodes," *Reviews of Modern Physics*, vol. 94, no. 4, p. 041 003, Dec. 2022. DOI: 10.1103/RevModPhys.94.041003. (visited on 11/29/2024).

[84] H. K. C. Beukers, M. Pasini, H. Choi, D. Englund, R. Hanson, and J. Borregaard, *Tutorial: Remote entanglement protocols for stationary qubits with photonic interfaces*, Oct. 2023. arXiv: 2310.19878 [quant-ph]. (visited on 03/05/2024).

[85] B. Kambs and C. Becher, "Limitations on the indistinguishability of photons from remote solid state sources," *New Journal of Physics*, vol. 20, no. 11, p. 115 003, Nov. 2018, ISSN: 1367-2630. DOI: 10.1088/1367-2630/aaea99. (visited on 11/29/2024).

[86] T. Legero, T. Wilk, A. Kuhn, and G. Rempe, "Time-resolved two-photon quantum interference," *Applied Physics B*, vol. 77, no. 8, pp. 797–802, Dec. 2003, ISSN: 1432-0649. DOI: 10.1007/s00340-003-1337-x. (visited on 03/13/2024).

[87] F. W. Sun and C. W. Wong, "Indistinguishability of independent single photons," *Physical Review A*, vol. 79, no. 1, p. 013 824, Jan. 2009. DOI: 10.1103/PhysRevA.79.013824. (visited on 10/09/2024).

[88] C. K. Hong, Z. Y. Ou, and L. Mandel, "Measurement of subpicosecond time intervals between two photons by interference," *Physical Review Letters*, vol. 59, no. 18, pp. 2044–2046, Nov. 1987. DOI: 10.1103/PhysRevLett.59.2044. (visited on 11/29/2024).

[89] S. D. Barrett and P. Kok, "Efficient high-fidelity quantum computation using matter qubits and linear optics," *Physical Review A*, vol. 71, no. 6, p. 060 310, Jun. 2005. DOI: 10.1103/PhysRevA.71.060310. (visited on 11/14/2024).

[90] *Cobolt 06-01 Series*. (visited on 06/14/2024).

[91] *TA-SHG pro*, https://www.toptica.com/products/tunable-diode-lasers/frequency-converted-lasers/ta-shg-pro, Datasheet. (visited on 11/29/2024).

[92] *AOM fibre coupled S-M200-0.4C2E-3-F2S for 633nm*. (visited on 11/29/2024).

[93] Jenoptik, *Integrated-optical modulators*, https://www.jenoptik.com/products/optoelectronic-systems/light-modulation/integrated-optical-modulators-fiber-coupled, Dec. 2019. (visited on 06/14/2024).

[94] *Thorlabs - S630-HP Single Mode Optical Fiber, 630 - 860 nm, Ø125 M m Cladding*, https://www.thorlabs.com. (visited on 11/29/2024).

[95] *Thorlabs - BSF10-A Ø1*, https://www.thorlabs.com. (visited on 11/29/2024).

[96] *FF625-SDi01-25x36*, https://www.idex-hs.com/store/product-detail/ff625_sdi01_25x36/fl-006917?cat_id=semrock_optical_filters&node=individual_optical_filters. (visited on 06/14/2024).

[97] *TLP01-628-25x36*, https://www.idex-hs.com/store/product-detail/tlp01_628_25x36/fl-009786?cat_id=semrock_optical_filters&node=individual_optical_filters. (visited on 06/14/2024).

[98] *Single Photon Counting Module COUNT-Series*, https://www.lasercomponents.com/fileadmin/user_upload/home/Datasheets/lc-photon-counter/count-series.pdf. (visited on 11/23/2024).

[99] *Solid Etalon | Fabry Perot Etalons | LightMachinery*, https://lightmachinery.com/optics/custom-optics/etalons/, Datasheet. (visited on 11/29/2024).

[100] *Evanescent Optics INC*. https://evanescentoptics.com/products/?id=16. (visited on 11/29/2024).

[101] *Photon spot | detectors*, https://www.photonspot.com/detectors. (visited on 11/29/2024).

[102] M. Pasini, *Nanophotonics with Diamond Color Centers: Quantum Optics and Entanglement Protocols*, Mar. 2024. (visited on 03/04/2024).

[103] *LDHe Measurement System*, Jan. 2024. (visited on 06/14/2024).

[104] *MAxes (TM) - Multi-Axis Vector Magnet*, https://www.americanmagnetics.com/maxes.php. (visited on 11/29/2024).

[105] *R&S®SGS100A SGMA RF source*. (visited on 11/29/2024).

[106] *Amplifier Research 40S1G4 Microwave Amplifier, 0.7 - 4.2 GHz, 40 W*. (visited on 11/29/2024).

[107] *Connectorized SMA, High Power, Linear Amplifier, 700 MHz to 6000 MHz, 50Ohm | ZHL-50W-63+ | Mini-Circuits*, https://www.minicircuits.com/WebStore/dashboard.html?model=ZHL-50W-63%2B&srsltid=AfmBOoqZ9rGZ4d21bGpyExF40N_mkQQd3-yO9Q7-JHYrvDqUsNWvg2cy. (visited on 11/29/2024).

[108] *ANPx101/ULT/RES+/HV - Linear x-Nanopositioner*. (visited on 11/29/2024).

[109] *ANPz102/ULT/RES+/HV - linear z-nanopositioner*. (visited on 11/29/2024).

[110] J. M. GmbH, *ADwin - the fastest real-time solutions under Windows*, https://www.adwin.de/. (visited on 06/14/2024).

[111] *HDAWG 750 MHz Arbitrary Waveform Generator | Zurich Instruments*, https://www.zhinst.com/en/products/hdawg-arbitrary-waveform-generator, Dec. 2019. (visited on 06/14/2024).

[112] *MultiHarp 150 High-Throughput Multichannel Event Timer & TCSPC Unit*. (visited on 11/29/2024).

[113] T. G. Tiecke *et al.*, "Efficient fiber-optical interface for nanophotonic devices," *Optica*, vol. 2, no. 2, pp. 70–75, Feb. 2015, ISSN: 2334-2536. DOI: 10.1364/OPTICA.2.000070. (visited on 11/20/2024).

[114] M. J. Burek, "Fiber-Coupled Diamond Quantum Nanophotonic Interface," *Physical Review Applied*, vol. 8, no. 2, 2017. DOI: 10.1103/PhysRevApplied.8.024026.

[115] H. Melkonyan, K. Sloyan, K. Twayana, P. Moreira, and M. S. Dahlem, "Efficient Fiber-to-Waveguide Edge Coupling Using an Optical Fiber Axicon Lens Fabricated by Focused Ion Beam," *IEEE Photonics Journal*, vol. 9, no. 4, pp. 1–9, Aug. 2017, ISSN: 1943-0655. DOI: 10.1109/JPHOT.2017.2710189. (visited on 12/02/2024).

[116] F. Schiappelli *et al.*, "Efficient fiber-to-waveguide coupling by a lens on the end of the optical fiber fabricated by focused ion beam milling," *Microelectronic Engineering*, Micro and Nano Engineering 2003, vol. 73–74, pp. 397–404, Jun. 2004, ISSN: 0167-9317. DOI: 10.1016/j.mee.2004.02.077. (visited on 12/02/2024).

[117] J.-F. Bourhis, "Fiber-to-waveguide connection," in *Glass Integrated Optics and Optical Fiber Devices: A Critical Review*, vol. 10275, SPIE, Jul. 1994, pp. 298–329. DOI: 10.1117/12.179761. (visited on 12/02/2024).

[118] J. Stark, "Beobachtungen über den Effekt des elektrischen Feldes auf Spektrallinien. I. Quereffekt," *Annalen der physik*, no. 43, pp. 965–983, Jan. 1914. DOI: 10.1002/andp.19143480702. (visited on 11/29/2024).

[119] G. L. van de Stolpe *et al.*, *Check-probe spectroscopy of lifetime-limited emitters in bulk-grown silicon carbide*, Sep. 2024. DOI: 10.48550/arXiv.2409.13018. arXiv: 2409.13018. (visited on 11/29/2024).

[120] S. L. N. Hermans *et al.*, "Entangling remote qubits using the single-photon protocol: An in-depth theoretical and experimental study," *New Journal of Physics*, vol. 25, no. 1, p. 013 011, Jan. 2023, ISSN: 1367-2630. DOI: 10.1088/1367-2630/acb004. (visited on 03/08/2024).

[121] R. A. Parker *et al.*, *A diamond nanophotonic interface with an optically accessible deterministic electronuclear spin register*, May 2023. DOI: 10.48550/arXiv.2305.18923. arXiv: 2305.18923 [cond-mat, physics:quant-ph]. (visited on 03/08/2024).

[122] L. Orphal-Kobin, C. G. Torun, J. M. Bopp, G. Pieplow, and T. Schröder, *Coherent microwave, optical, and mechanical quantum control of spin qubits in diamond*, Dec. 2023. DOI: 10.48550/arXiv.2312.06431. arXiv: 2312.06431 [quant-ph]. (visited on 12/29/2023).

[123] L. Robledo, L. Childress, H. Bernien, B. Hensen, P. F. A. Alkemade, and R. Hanson, "High-fidelity projective read-out of a solid-state spin quantum register," *Nature*, vol. 477, no. 7366, pp. 574–578, Sep. 2011, ISSN: 1476-4687. DOI: 10.1038/nature10401. (visited on 12/02/2024).

[124] J. Arjona Martínez, "A nanophotonic platform for the tin-vacancy centre," Jun. 2024. DOI: 10.17863/CAM.109597. (visited on 07/22/2024).

[125] E. I. Rosenthal *et al.*, *Single-Shot Readout and Weak Measurement of a Tin-Vacancy Qubit in Diamond*, Mar. 2024. DOI: 10.48550/arXiv.2403.13110. arXiv: 2403.13110 [quant-ph]. (visited on 04/02/2024).

[126] L. Novotny and B. Hecht, *Principles of Nano-Optics*, 2nd ed. Cambridge: Cambridge University Press, 2012, ISBN: 978-1-107-00546-4. DOI: 10.1017/CBO9780511794193. (visited on 11/24/2024).

[127] R. H. Brown and R. Twiss, "LXXIV. A new type of interferometer for use in radio astronomy," *The London, Edinburgh, and Dublin Philosophical Magazine and Journal of Science*, vol. 45, no. 366, pp. 663–682, Jul. 1954, ISSN: 1941-5982. DOI: 10.1080/14786440708520475. (visited on 11/24/2024).

[128] R. E. Fishman, R. N. Patel, D. A. Hopper, T.-Y. Huang, and L. C. Bassett, "Photon-Emission-Correlation Spectroscopy as an Analytical Tool for Solid-State Quantum Defects," *PRX Quantum*, vol. 4, no. 1, p. 010 202, Mar. 2023. DOI: 10.1103/PRXQuantum.4.010202. (visited on 11/29/2024).

[129] A. Beveratos, R. Brouri, T. Gacoin, A. Villing, J.-P. Poizat, and P. Grangier, "Single Photon Quantum Cryptography," *Physical Review Letters*, vol. 89, Nov. 2002. DOI: 10.1103/PhysRevLett.89.187901. (visited on 11/24/2024).

[130] A. Beveratos, R. Brouri, T. Gacoin, J.-P. Poizat, and P. Grangier, *Nonclassical radiation from diamond nanocrystals*, Oct. 2001. DOI: 10.48550/arXiv.quant-ph/0104028. arXiv: quant-ph/0104028. (visited on 11/24/2024).

[131] W. Schmunk *et al.*, "Photon number statistics of NV centre emission," *Metrologia*, vol. 49, no. 2, S156, Mar. 2012, ISSN: 0026-1394. DOI: 10.1088/0026-1394/49/2/S156. (visited on 11/24/2024).

[132] M. Berthel, O. Mollet, G. Dantelle, T. Gacoin, S. Huant, and A. Drezet, "Photophysics of single nitrogen-vacancy centers in diamond nanocrystals," *Physical Review B*, vol. 91, no. 3, p. 035 308, Jan. 2015. DOI: 10.1103/PhysRevB.91.035308. (visited on 11/24/2024).

[133] R. N. Patel *et al.*, "Efficient photon coupling from a diamond nitrogen vacancy center by integration with silica fiber," *Light: Science & Applications*, vol. 5, no. 2, e16032–e16032, Feb. 2016, ISSN: 2047-7538. DOI: 10.1038/lsa.2016.32. (visited on 11/24/2024).

[134] R. Waltrich, M. Klotz, V. N. Agafonov, and A. Kubanek, "Two-photon interference from silicon-vacancy centers in remote nanodiamonds," *Nanophotonics*, vol. 12, no. 18, pp. 3663–3669, Sep. 2023, ISSN: 2192-8614. DOI: 10.1515/nanoph-2023-0379. (visited on 11/24/2024).

[135] M. Schäfer, B. Kambs, D. Herrmann, T. Bauer, and C. Becher, "Two-Stage, Low Noise Quantum Frequency Conversion of Single Photons from Silicon-Vacancy Centers in Diamond to the Telecom C-Band," *Advanced Quantum Technologies*, vol. n/a, no. n/a, p. 2 300 228, Sep. 2023, ISSN: 2511-9044. DOI: 10.1002/qute.202300228. (visited on 11/24/2024).

[136] K. Kuruma *et al.*, "Coupling of a single tin-vacancy center to a photonic crystal cavity in diamond," *Applied Physics Letters*, vol. 118, no. 23, p. 230 601, Jun. 2021, ISSN: 0003-6951. DOI: 10.1063/5.0051675. (visited on 11/24/2024).

[137] J. Arjona Martínez *et al.*, "Photonic Indistinguishability of the Tin-Vacancy Center in Nanostructured Diamond," *Physical Review Letters*, vol. 129, no. 17, p. 173 603, Oct. 2022, ISSN: 0031-9007, 1079-7114. DOI: 10.1103/PhysRevLett.129.173603. (visited on 03/08/2024).

[138] A. Dréau, A. Tchebotareva, A. E. Mahdaoui, C. Bonato, and R. Hanson, "Quantum Frequency Conversion of Single Photons from a Nitrogen-Vacancy Center in Diamond to Telecommunication Wavelengths," *Physical Review Applied*, vol. 9, no. 6, p. 064 031, Jun. 2018. DOI: 10.1103/PhysRevApplied.9.064031. (visited on 11/29/2024).

[139] Y. Doi *et al.*, "Deterministic Electrical Charge-State Initialization of Single Nitrogen-Vacancy Center in Diamond," *Physical Review X*, vol. 4, no. 1, p. 011 057, Mar. 2014. DOI: 10.1103/PhysRevX.4.011057. (visited on 12/02/2024).

[140] A. Aarab, R. Azouit, V. Reiher, and Y. Bérubé-Lauzière, "State initialization of a hot spin qubit in a double quantum dot by measurement-based quantum feedback control," *Physical Review B*, vol. 106, no. 23, p. 235 309, Dec. 2022. DOI: 10.1103/PhysRevB.106.235309. (visited on 12/02/2024).

[141] L. Wienhoven, "On-Chip Frequency Tuning of Individual Tin-Vacancy Centres in Diamond," MSc Thesis, Delft University of Technology, Delft, Apr. 2024. (visited on 12/02/2024).

[142] H. Larocque *et al.*, "Tunable quantum emitters on large-scale foundry silicon photonics," *Nature Communications*, vol. 15, no. 1, p. 5781, Jul. 2024, ISSN: 2041-1723. DOI: 10.1038/s41467-024-50208-0. (visited on 07/29/2024).

[143] *WPH05M-633 Ø1/2*, https://www.thorlabs.com. (visited on 11/29/2024).

[144] *WPQ05M-633 Ø1/2*, https://www.thorlabs.com. (visited on 11/29/2024).

[145] *FELH0550 Ø25.0 mm Longpass Filter, Cut-On Wavelength: 550 nm*, https://www.thorlabs.com. (visited on 11/29/2024).

[146] *FG050LGA Multimode Fiber, 0.22 NA, Low OH, Ø50 M m Core, 400 - 2400 nm*, https://www.thorlabs.com. (visited on 11/29/2024).

[147] *Thorlabs - K10CR1 Motorized Rotation Mount for Ø1*, https://www.thorlabs.com. (visited on 11/29/2024).

[148] R. C. Jones, "A New Calculus for the Treatment of Optical SystemsI. Description and Discussion of the Calculus," *JOSA*, vol. 31, no. 7, pp. 488–493, Jul. 1941. DOI: 10.1364/JOSA.31.000488. (visited on 11/29/2024).

[149] A. Stolk *et al.*, "Telecom-band quantum interference of frequency-converted photons from remote detuned NV centers," *PRX Quantum*, vol. 3, no. 2, p. 020 359, Jun. 2022, ISSN: 2691-3399. DOI: 10.1103/PRXQuantum.3.020359. arXiv: 2202.00036 [quant-ph]. (visited on 07/31/2024).

[150] *Thorlabs - CS165MU/M Zelux® 1.6 MP Monochrome CMOS Camera, M6 Taps*, https://www.thorlabs.com. (visited on 11/29/2024).

A

Optical excitation and collection

A.1. Known loss channels in the optical collection efficiency

In an attempt to isolate the contributions from the fiber-waveguide and emitter-waveguide interfaces, an estimate of the optical losses in the remaining components of the optical path is made here. It should be noted that these are rough estimates, often based on standardized data-sheets of individual components. These suffice to get an order of magnitude calculation of the emitter-fiber coupling efficiency, but should not be seen as exact measures. The known optical losses in the components of the PSB collection path are:

- The S-630HP **single-mode fiber** in the cryostat has a 10 $\frac{\text{dB}}{\text{km}}$ attenuation [94], which translates to a 2.3 % photon loss over the 10 m of fiber within the fridge.
- Each **waveplate** in the optical path reflects about 2 % of the PSB photons [143, 144].
- The **beam sampler** in the PSB path sends ~2 % of the PSB photons in the wrong direction [95].
- The **hard-coated longpass filter** in the PSB path blocks roughly 5 % of the PSB photons [145].
- The **dichroic mirror** has a cut-off wavelength at ~625 nm, which is estimated to transmit roughly 10 % of the PSB photons [96].
- The **tunable longpass filter** in the PSB path blocks roughly 2 % of the PSB photons [97].
- The **multi-mode fiber** that guides the PSB photons from the optical breadboard to the detector has a 10 $\frac{\text{dB}}{\text{km}}$ attenuation, which translates into a 1.15 % photon loss [146].
- The **Avalanche Photon Detector** is estimated to have a 70 % detection efficiency at the relevant wavelengths of the PSB [98].

Correcting for all these values leaves the losses in the free-space alignment of the optical PSB collection path, the emitter-waveguide coupling and the fiber-waveguide coupling. Correcting the obtained collection efficiencies in Section 4.3 for these losses yields an estimated efficiency of 4.1 %. It should again be emphasized that these values are only indicative, as the estimations are very rough.

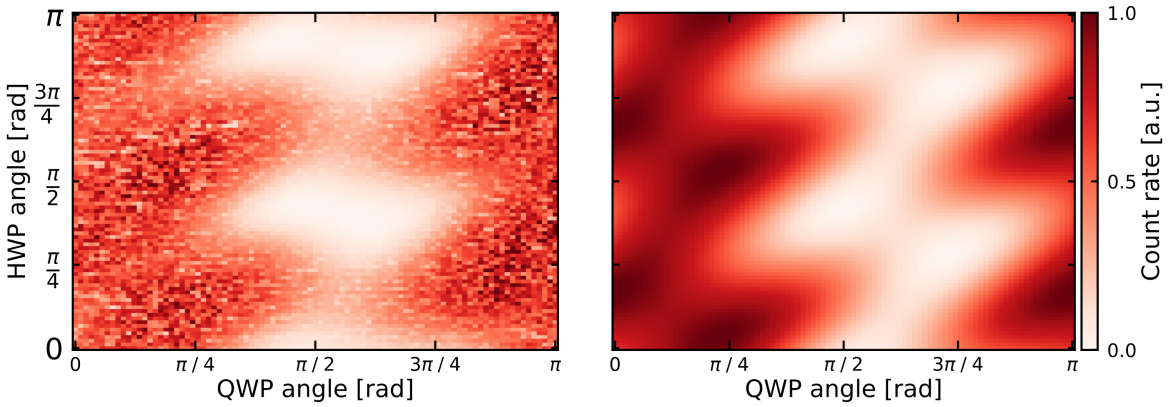

Figure A.1: Measurement of the dipole moment orientation of a tin-vacancy through the polarization of optical excitations. (a) A measurement of the intensity in the PSB collection path during resonant excitation at different waveplate configurations. Each resonant excitation is preceeded by a CR-check, where the threshold value is automatically corrected to be lower for very misaligned polarization angles and higher for very well-aligned angles. (b) Simulations of the predicted intensity of emissions at the same waveplate angles as in (a). The model includes the assumption that the waveguide is a birefringent partial polarizer. The simulated behavior has many resemblances of the measured data, but only serves as a qualitative comparison since it is not a fit.

A.2. Polarization-dependent excitation and filtering

This section will focus on the measurements of polarization angles of excitation pulses with respect to the emitter dipole orientation. The polarization control of the excitation is done through a combination of a half- and quarter-waveplate, located in front of the collimators of the fibers going into the cryostat. These waveplates are mounted inside motorized rotation mounts [147], which are used to controllably measure the effect of excitation at different combination of the waveplate angles. A rotation of these waveplates causes a change in the polarization of the transmitted light, which can be modeled through Jones calculus [148]. Experimentally, the effect can be measured through the collected intensity of emissions in the PSB, as shown in Figure A.1a. The figure shows the relation between the measured count rate during resonant excitation and the angles of the quarter- and half-waveplate.

The modeling of such an experiment can be done with Jones calculus. The excitation light can be modeled as a Jones vector with the following definition:

$$\mathbf{E}_0(z,t) = \mathscr{R}e\left[\begin{pmatrix} E_{0,x}e^{i\phi_x} \\ E_{0,y}e^{i\phi_y} \\ 0 \end{pmatrix} e^{i(\omega t - kz)}\right] \Rightarrow \mathbf{J}_0 = \begin{pmatrix} E_{0,x}e^{i\phi_x} \\ E_{0,y}e^{i\phi_y} \end{pmatrix}. \tag{A.1}$$

Here, ω is the angular frequency of the optical excitation, k is the wavenumber ($k = \frac{\omega}{c}$), z is the spatial position along the optical path and the parameters $\{E_{0,x}, E_{0,y}, \phi_x, \phi_y\}$ describe the polarization of the excitation, as summarized by the Jones vector $\mathbf{J}_0$. The effects of the half- and quarter-waveplate on an incoming Jones vector $\mathbf{J}_0$ can be described through their Jones matrices:

$$\hat{\mathbf{J}}_{HWP} = i\begin{pmatrix} \cos(2\theta) & \sin(2\theta) \\ \sin(2\theta) & -\cos(2\theta) \end{pmatrix} \; ; \; \hat{\mathbf{J}}_{QWP} = \frac{1}{\sqrt{2}}\begin{pmatrix} 1+i\cos(2\theta) & i\sin(2\theta) \\ i\sin(2\theta) & 1-i\cos(2\theta) \end{pmatrix}. \tag{A.2}$$

The angle θ in Equation A.2 reflects the rotated angle from the slow-axis. Finally, the effect of the waveguide on the polarization is modeled as a birefringent partial polarizer:

$$\hat{\mathbf{J}}_{WG} = \begin{pmatrix} \alpha & 0 \\ 0 & \beta e^{i\phi} \end{pmatrix}. \tag{A.3}$$

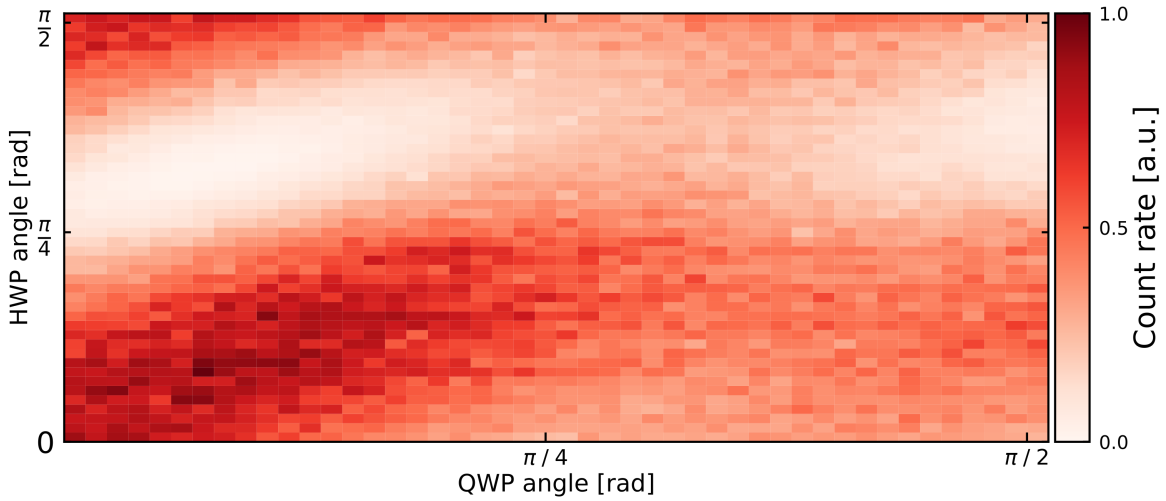

Figure A.2: Measurement of the intensity in the ZPL detection path during continuous off-resonant (2 GHz detuned) excitation, while sweeping the angles of the quarter- and half-waveplate in front of the polarizer in the collection path. The angles that minimize the reflection counts are used as the cross-polarization settings. The measurement shows a 22 dB suppression ratio.

The values of α and β depend on the waveguide design, whereas ϕ depends on the distance the light has to travel in the waveguide before reaching the emitter. Finally, the polarization of the excitation light at the position of the emitter can be calculated by applying the Jones matrices to the incoming Jones vector:

$$\mathbf{J}_{em} = \hat{\mathbf{J}}_{WG}\,\hat{\mathbf{J}}_{HWP}\,\hat{\mathbf{J}}_{QWP}\,\mathbf{J}_0 = \begin{pmatrix} E_{em,x}e^{i\phi_x} \\ E_{em,y}e^{i\phi_y} \end{pmatrix}. \tag{A.4}$$

Finally, the model needs to include a relation between the polarization of the excitation and the efficiency of driving the emitter. As described in Section 2.1.3, the optical transition can be modeled as an interaction between the electric field and the dipole operator of the emitter. In a Cartesian coordinate system with a z-axis aligned to the waveguide axis, the dipole moment can be written as

$$\mathbf{p} = p\begin{pmatrix} \cos(\alpha) \\ \sin(\alpha) \\ 0 \end{pmatrix}, \tag{A.5}$$

where p is the magnitude of the dipole moment and α an angle in the waveguide, which can be determined from the diamond lattice structure to have two allowed values: $\alpha \in \{54.7°, 125.3°\}$. The interaction strength between the excitation and emitter can then be calculated as the inner product between the dipole moment (Equation A.5) and the electric field (Equation A.1) of the Jones vector in Equation A.4. This then leads to an interaction strength of

$$g(t) \sim \left| E_{em,x}\cos(\alpha)\cos\left(\omega t + \phi_x\right) + E_{em,y}\sin(\alpha)\sin\left(\omega t + \phi_y\right)\right|. \tag{A.6}$$

Finally, the expected emission strength from the emitter upon continuous excitation can be calculated as an integral over the full duration of the excitation:

$$S \sim \int_{excitation} g(t)\,dt. \tag{A.7}$$

In the end, this formulation suffices since the simulations are only used for normalized count rates, meaning that any prefactors here can be omitted. The calculation of this normalized emission strength for all half- and quarter-waveplate angles in the measurement is shown in Figure A.1b. It should be emphasized that this figure is a stand-alone simulation and not a fit of the data in Figure A.1a. The simulation shows close resemblance to the measured data and features the same characteristic behavior.

As presented in Section 3.6, it is crucial for pulsed experiments to have a controllable misalignment of the excitation polarization with the dipole moment. In this work, a misalignment of 45° is always used. The waveplate settings to achieve this misalignment are calibrated with measurements such as the one presented in Figure A.1a. Specifically, the aligned angles of the waveplates are extracted from Figure A.1a to be 60° for the half-waveplate and 178° for the quarter-waveplate. From there, the 45° misalignment can be realized by a 22.5° rotation of the half-waveplate to an angle of 37.5°, while keeping the quarter-waveplate at the same angle of 178°

This misalignment is essential for polarization filtering of the resonant laser reflections. The polarization filtering is experimentally realized by another combination of a half- and quarter-waveplate, accompanied by a fixed polarizer (that is aligned to the polarization of one of the modes of the Polarization-Maintaining fiber of the central beam splitter). The angles of the half- and quarter-waveplates are calibrated such that the polarizer extinguishes all laser reflections. The polarizer itself is kept at a fixed angle (aligned with one of the polarization axes of the ZPL collection fiber). A typical calibration measurement of these waveplates can be found in Figure A.2. The figure shows a measurement of the intensity of the laser reflections during continuous off-resonant excitation (~2 GHz detuned) for a range of different waveplate angles. The calibration is used to find the waveplate angles that give the minimum count rate, which in this case would be a half-waveplate at an angle of 14° and a quarter-waveplate at an angle of 12°. Comparing the count rate at this setting to the maximum count rate, an extinction ratio of -22 dB is found.

B

Modeling and error propagation for TPQI experiments

B.1. Time correlations for distinguishable photons

This section will focus on the model that was used to calculate the expected correlation function for fully distinguishable photons (in Figure 7.3). The modeling is based on the theoretical framework presented in Section 2.2.3 combined with derivations from [149]. Firstly, the distinguishable photons are assumed to have a wavefunction that can be written as

$$|\psi\rangle(t) = \frac{e^{i\omega t}e^{-\frac{t}{2\tau}}}{\sqrt{\tau(1-e^{-T/\tau})}}H(t), \tag{B.1}$$

where τ is the decay time of the original spontaneous emission source, T is the length of the detection window (which starts at $t = 0$), ω is the angular frequency of the photon and $H(t)$ is the heaviside function. Next to these photons emitted by tin-vacancy centers through spontaneous emission, there are also dark counts. These are assumed to be uniformly distributed among the time window, such that:

$$|\psi_{DC}\rangle(t) = \frac{H(t) - H(t-T)}{\sqrt{T}}. \tag{B.2}$$

For two distinguishable photons coming from spontaneous emission at a tin-vacancy center, the autocorrelation function can be expressed as an integral of their detection probabilities, as predicted from their wavefunctions [149]:

$$\begin{aligned} g^{(2)}_{SnV-SnV}(\Delta t) =& \frac{1}{2}\int_{-\infty}^{\infty} |\,|\psi\rangle(t)|^2\,|\psi\rangle(t+\Delta t)|^2\,dt = \dots \\ =& \frac{e^{|\Delta t|/\tau} - e^{(2T-|\Delta t|)/\tau}}{4\tau(1-e^{-T/\tau})^2}. \end{aligned} \tag{B.3}$$

This autocorrelation function describes the coincident detection probability for two distinguishable photons emitted by two tin-vacancy centers. Given the fact that the setup has some noise sources, the total measured autocorrelation function is a combination of this autocorrelation function and those of the dark counts (either interfering with themselves or with a photon emitted by a tin-vacancy center). Following a similar approach as for Equation B.3, these autocorrelation contributions can be found as [149]

$$\begin{cases} g^{(2)}_{SnV-DC}(\Delta t) = \dfrac{1 - e^{(T-|\Delta t|)/\tau} + e^{|\Delta t|/\tau} - e^{-T/\tau}}{4\tau T(1-e^{-T/\tau})} \\ g^{(2)}_{DC-DC}(\Delta t) = \dfrac{T-|\Delta t|}{2T^2}. \end{cases} \tag{B.4}$$

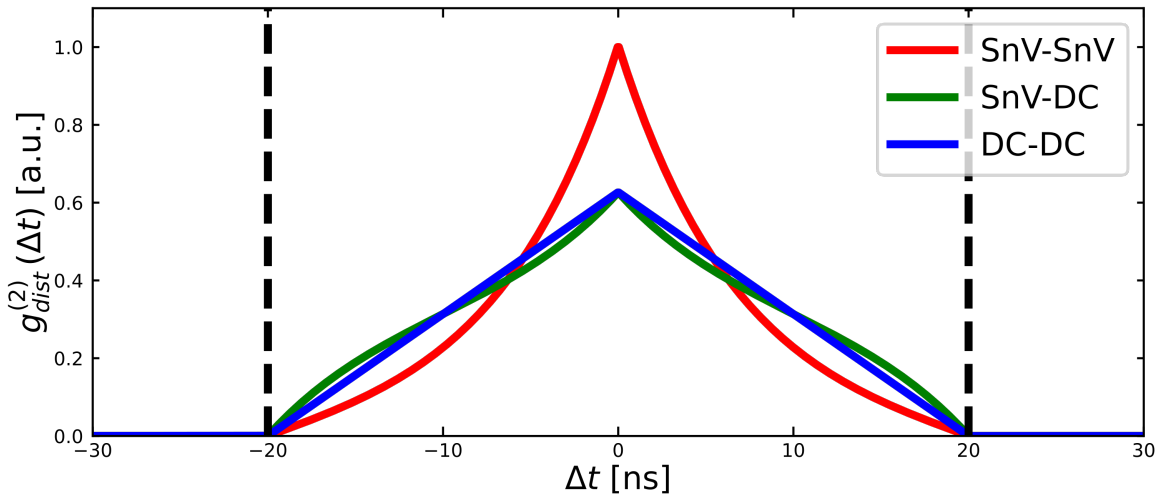

Figure B.1: Plots of the autocorrelation functions between different types of distinguishable photons, as predicted from Equations B.3 & B.4. Each autocorrelation function is normalized for illustration purposes.

The shapes of the three different autocorrelation functions can be found in Figure B.1. The full autocorrelation function (as measured in the non-zero time bins in Figure 7.3) is found as a linear combination of these, with weights determined by the detection probabilities of SnV- and dark counts. This linear combination can be expressed in terms of the probabilities defined in Equation 2.36:

$$\begin{aligned} g^{(2)}_{\text{dist}}(\Delta t) = &(p^{SnV}_{A\to 1} + p^{SnV}_{B\to 1})(p^{SnV}_{A\to 1} + p^{SnV}_{B\to 1})\, g^{(2)}_{SnV-SnV}(\Delta t) \\ &+(p^{SnV}_{A\to 1} + p^{SnV}_{B\to 1})(p^{DC}_{A\to 2} + p^{DC}_{B\to 2})\, g^{(2)}_{SnV-DC}(\Delta t) \\ &+(p^{DC}_{A\to 1} + p^{DC}_{B\to 1})(p^{SnV}_{A\to 2} + p^{SnV}_{B\to 2})\, g^{(2)}_{SnV-DC}(\Delta t) \\ &+(p^{DC}_{A\to 1} + p^{DC}_{B\to 1})(p^{DC}_{A\to 2} + p^{DC}_{B\to 2})\, g^{(2)}_{DC-DC}(\Delta t) \end{aligned} \tag{B.5}$$

Moreover, the autocorrelation functions also require a scaling in each experimental difference bin of Figure 7.3 according to the actual probability of measuring two photons with a certain experimental bin difference in a 100-pulse experiment. For all non-zero bins, this scaling factor s can be written as $s = \frac{100-|bin|}{100}$, where |bin| is used to denote the index of the bin. For the zero bin, this scaling factor is exactly $s = \frac{1}{2}$. These scaled autocorrelation functions are used to model the data in Figure 7.3.

B.2. Time correlations for indistinguishable photons

Given the modeling of distinguishable photons in the previous section, this section will focus on the autocorrelation function of two indistinguishable photons. As presented in Section 2.2.1, this autocorrelation function is always zero for two photons with equal wavefunctions. In order to model the actual experimentally achieved photons, this section will focus on the influences of non-equal lifetimes and spectral diffusion. To this end, we start by defining the photonic wavefunction in the measurement window (analogous to [149]) as

$$|\psi_{1,2}(t)\rangle = \frac{e^{-i\omega_{1,2}t-\frac{t}{2\tau_{1,2}}}}{\sqrt{\tau_{1,2}\left(e^{-T_s/\tau_{1,2}} - e^{-T_e/\tau_{1,2}}\right)}} H(t-T_s)(1-H(t-T_e)). \tag{B.6}$$

The photonic wavefunctions $|\psi_{1,2}(t)\rangle$ depend on the angular frequencies $\omega_{1,2}$, the spontaneous emission decay times $\tau_{1,2}$ and the measurement window $[T_s, T_e]$, which is enforced by the combination of Heaviside functions $H(t)$. This formulation enables the introduction of spectral diffusion by not assuming equal frequencies of the two photons. The evolution of the shape of the coincident autocorrelation function can be calculated

by substituting the wavefunctions in Equation B.6 into Equation 2.30, which leads to

$$P_{coinc}(t,\Delta t) = \frac{1}{4}\frac{e^{-\frac{\Delta t}{\tau_1}} + e^{-\frac{\Delta t}{\tau_2}} - 2e^{-\Delta t\left(\frac{1}{2\tau_1}+\frac{1}{2\tau_2}\right)}\cos((\omega_1-\omega_2)\Delta t)}{\tau_1\tau_2\left(e^{-\frac{T_s}{\tau_1}} - e^{-\frac{T_e}{\tau_1}}\right)\left(e^{-\frac{T_s}{\tau_2}} - e^{-\frac{T_e}{\tau_2}}\right)}\, e^{-t\left(\frac{1}{\tau_1}+\frac{1}{\tau_2}\right)} W(t,\Delta t,T_s,T_e), \tag{B.7}$$

where $W(t,\Delta t,T_s,T_e) \equiv H(t-T_s)(1-H(t-T_e))H(t-(T_s-\Delta t))(1-H(t-(T_e-\Delta t)))$.

Naturally, the measured autocorrelation function for some time difference Δt is an integral of this function over all times t. For the function in Equation B.7, this integral needs to be calculated separately for different values of Δt due to the window, which can be separated into

$$W(t,\Delta t,T_s,T_e) = \begin{cases} 0, & \Delta t < T_s - T_e \qquad\qquad \forall\ t \in (-\infty,\infty) \\ 1, & T_s - T_e < \Delta t < 0 \quad \forall\ t \in [T_s-\Delta t,\ T_e] \\ 1, & 0 < \Delta t < T_e - T_s \quad \forall\ t \in [T_s,\ T_e-\Delta t] \\ 0, & \Delta t > T_e - T_s \qquad\qquad \forall\ t \in (-\infty,\infty). \end{cases} \tag{B.8}$$

With this derived shape of the correlation window, the integral over the coincidence probability in Equation B.7 can be found as

$$g^{(2)}_{\omega_1,\omega_2}(\Delta t) = \frac{e^{-\frac{\Delta t}{\tau_1}} + e^{-\frac{\Delta t}{\tau_2}} - 2e^{-\Delta t\left(\frac{1}{2\tau_1}+\frac{1}{2\tau_2}\right)}\cos((\omega_1-\omega_2)\Delta t)}{4(\tau_1+\tau_2)\left(e^{-\frac{T_s}{\tau_1}} - e^{-\frac{T_e}{\tau_1}}\right)\left(e^{-\frac{T_s}{\tau_2}} - e^{-\frac{T_e}{\tau_2}}\right)} \cdot \begin{cases} 0, & |\Delta t| > T_e - T_s \\ \left(e^{-T_s\left(\frac{1}{\tau_1}+\frac{1}{\tau_2}\right)} - e^{-(T_e-\Delta t)\left(\frac{1}{\tau_1}+\frac{1}{\tau_2}\right)}\right), & 0 < \Delta t < T_e - T_s \\ \left(e^{-(T_s-\Delta t)\left(\frac{1}{\tau_1}+\frac{1}{\tau_2}\right)} - e^{-T_e\left(\frac{1}{\tau_1}+\frac{1}{\tau_2}\right)}\right), & T_s - T_e < \Delta t < 0 \end{cases}. \tag{B.9}$$

The autocorrelation function $g^{(2)}_{\omega_1,\omega_2}(\Delta t)$ in Equation B.9 describes the interference pattern for two photons with frequencies ω_1 and ω_2. From the shape of this function, it becomes clear however that the function only depends on the *difference* of the frequencies ω_1 and ω_2. As a result from spectral diffusion, we can describe ω_1 and ω_2 as normally distributed independent stochastic variables, with variances σ_1 and σ_2. This means that their difference $\Delta\omega \equiv \omega_1 - \omega_2$ is also normally distributed with mean $\mu = 0$ and variance $\sigma = \sqrt{\sigma_1^2 + \sigma_2^2}$. The measured autocorrelation function after many samples of the random frequencies can then be calculated as an integral over the probability distribution of the random variables. This integral is not calculated analytically here, but is rather done numerically with a Monte-Carlo approach. The result of this numerical integration for different spectral diffusion sizes can be found in Figure 2.7.

B.3. Error propagation for TPQI experiments

This Appendix demonstrates the model that was used for error propagation of TPQI measurement results. The description here is based on the model presented in Section 2.2.3. The model assumes that measurement results are obtained from 3 different experiments on the two nodes (named *Alice* and *Bob* for convenience):

1. N repetitions of a TPQI experiment, where both Alice and Bob are simultaneously excited, bringing their photons to a central beam splitter at the same time. The probability of measuring a coincidence in the output ports p_0^T is measured along with the probability of detection events in consecutive experiments on the different detectors p_1^T (where the notation T signifies "TPQI").

2. N repetitions of the same experiment, but now only exciting the Alice node. This measurement gives information on the noise counts from Alice through the measured coincidence probability p_0^A and on the collection efficiency of Alice through the probability of consecutive detection events p_1^A.

3. N repetitions of the same experiment as in (2), but now for Bob's node, leading to a measurement of p_0^B and p_1^B.

These combined measurements give access to 6 measured values, which fully describe the measurement outcome:

$$\vec{x} = (p_0^T,\ p_1^T,\ p_0^A,\ p_1^A,\ p_0^B,\ p_1^B). \tag{B.10}$$

For a theoretical model, the experiments can be fully described by a set of underlying physical parameters, given by:

$$\vec{\theta} = (\eta,\ p_A^{SnV},\ p_A^{DC},\ p_B^{SnV},\ p_B^{DC},\ \alpha_A,\ \alpha_B). \tag{B.11}$$

The definitions of $p_{A,B}^{SnV/DC}$ are identical to those in Section 2.2.3, η is the indistinguishability and α_A (α_B) is the ratio of photons from Alice (Bob) that go into output arm 1 of the beamsplitter. The aim of this section is to find a relation between the probability distribution of the parameters in $\vec{\theta}$ given a single instance of the measured values in $\vec{x}$. To do this, it is first important to establish relations between the parameters in $\vec{x}$ and the underlying physical parameters in $\vec{\theta}$. These relations can be derived as

$$\begin{cases} p_0^A = \alpha_A(1-\alpha_A)p_A^{DC}(2p_A^{SnV} + p_A^{DC}) \\ p_1^A = \alpha_A(1-\alpha_A)(p_A^{SnV} + p_A^{DC})^2 \\ p_0^B = \alpha_B(1-\alpha_B)p_B^{DC}(2p_B^{SnV} + p_B^{DC}) \\ p_1^B = \alpha_B(1-\alpha_B)(p_B^{SnV} + p_B^{DC})^2 \\ p_0^T = (\alpha_A+\alpha_B-2\alpha_A\alpha_B)((1-\eta)p_A^{SnV}p_B^{SnV} + p_A^{SnV}p_B^{DC} + p_A^{DC}p_B^{SnV} + p_A^{DC}p_B^{DC}) + p_0^A + p_0^B \\ p_1^T = (\alpha_A+\alpha_B-2\alpha_A\alpha_B)(p_A^{SnV} + p_A^{DC})(p_B^{SnV} + p_B^{DC}) + p_1^A + p_1^B. \end{cases} \tag{B.12}$$

Concretely, the relations in Equation B.12 allow one to compute the values that should get measured given some combination of the physical parameters of the system. This operation of figuring out the supposed measurements from a set of physical parameters will be denoted as: $\hat{\vec{x}} = f(\vec{\theta})$.

The measured coincidences in each bin (see Figure 7.3) follow from an underlying Poissonian distribution. This means that the combined likelihood of measuring some set of parameters $\vec{x}$ given that the underlying physical parameters are modeled by $\vec{\theta}$ (corresponding to $\hat{\vec{x}} = f(\vec{\theta})$) can be written as:

$$p\left(\vec{x}|\vec{\theta}\right) = \prod_{(p,\hat{p})\in(\vec{x},\hat{\vec{x}})} \mathbf{P}_{N\hat{p}}(Np) \qquad \text{where } \mathbf{P}_k(n) = \frac{k^n e^{-k}}{n!}. \tag{B.13}$$

The expression in Equation B.13 can be summarized as a product of Poissonian distributions, centered around the expected number of detections (consecutive or coincident) and evaluated at the actual measured number of detections. It should however be noted that we are eventually interested in figuring out the probabilty distributions of the parameters in $\vec{\theta}$ conditioned on a measurement of $\vec{x}$. This probability distribution can now be obtained through Bayes' rule:

$$p\left(\vec{\theta}|\vec{x}\right) = \frac{p\left(\vec{x}|\vec{\theta}\right)p(\vec{\theta})}{p(\vec{x})}. \tag{B.14}$$

For the purposes of the error estimations from a single instance of $\vec{x}$, the value of $p(\vec{x})$ can be considered a normalization constant and can thus be omitted for derivation purposes. The value of $p\left(\vec{x}|\vec{\theta}\right)$ can be calculated through Equation B.13 and the prior $p(\vec{\theta})$ can be chosen strategically to reflect the prior knowledge on the possibilities for the elements in $\vec{\theta}$. In this work, the prior for each element in $\vec{\theta}$ is taken to be a uniform distribution between 0 and 1. On the domain from 0 to 1, we can thus compute the likelihood of parameters $\vec{\theta}$ given a measurement of $\vec{x}$ through Equation B.13.

In Section 7.2, this framework is used for error estimation for the indistinguishability η only. To get an estimate of the probability distribution of η, its marginalized likelihood function needs to be computed. The best estimate of the indistinguishability is then given by the maximum of this marginalized probability distribution. For computational reasons, it is often easier to find this value through the log-likelyhood function $L(\vec{\theta},\vec{x})$, which can be computed by substituting Equation B.13 into Equation B.14, combined with the previously stated prior to obtain

$$L(\vec{\theta},\vec{x}) \sim \begin{cases} \sum_{(p,\hat{p})\in(\vec{x},\hat{\vec{x}})} \left[N(p\ln(N\hat{p}-\hat{p}) - \ln((Np)!)\right], \text{ if } 0 \le \theta_i \le 1\ \forall\ \theta_i \in \theta \\ 0, \text{ elsewhere.} \end{cases} \tag{B.15}$$

For error estimation, this loglikelihood function is maximized and marginalized by an integration over a small 5D hyperspherical region around the optimum.

C

Details of the setup

C.1. Imaging Optics

An essential feature of the setup is the confocal imaging capability. This section will describe the setup configuration that is used for the imaging. Imaging the sample inside the cryostat is crucial for the experiments, since the fiber-waveguide coupling procedure is purely based on the ability to visually see the fiber and waveguides. Moreover, imaging also allows certain alignment optimizations for the excitation paths. The setup is also assymetric in terms of the imaging capability, which means that there is only one imaging path, either showing the side of Alice or Bob.

Figure C.1a shows a schematic representation of the imaging path in the setup. Imaging is done through a set of 4 lenses in the cryostat, that combine to make 2 optical 4f-systems. Such 4f-systems are designed to minimize scattering losses and to allow flexibility in the magnification. The imaging is done with a red LED, which illuminates the sample from outside the cryostat through this double 4f-system. The reflections of the sample pass through the same 4f system and are sent towards a camera [150] through a pellicle beam splitter. The camera has a live imaging capability and is often used with exposure times in the order of 1 ms.

To focus the image, the final lens in the 4f system is controlled in the z-direction with a stepper motor (see Figure C.4). Two stepper motors beneath the sample stage allow for control over the x- and y-directions in the image (also visible in Figure C.4). Figure C.1b shows an example of a focused image on a chiplet on Bob's side of the setup. The picture shows three main elements. Firstly, the tapered fiber tip is visible on the right side of the picture. The picture was taken at an instance where the fiber was not coupled to any waveguides, but was instead moved far away from them. Secondly, the image shows a chiplet with 8 suspended waveguides (beams). These waveguides are made out of diamond that contains the tin-vacancy centers. Lastly, the image features a vertical shaded region. This "shadow" comes from the bond wire, which is drawn ~(50-100) μm above the waveguides (and is thereby out of focus in this picture).

Images like Figure C.1b are used to controllably move the fiber into a lensed position where it is coupled to a waveguide. To do this, a resonant laser is turned on, which lights up the tip of the fiber. After this, the fiber is moved to the side of a chiplet, where the diamond is still in it's bulk shape. From there, the z-position of the fiber is moved down, until the tip gets sufficiently close to the surface that van der Waal forces pull it in contact. This can be seen by a dimming of the scattered light at the fiber tip. Since the bulk diamond and the waveguides are at the same height, the fiber is now in the correct z-position. It is then only moved in the x- and y-positions in order to position the tip within a few μm in front of the targeted waveguide. Coupling can be seen by an image of scattering light within the waveguide on the camera. Experimentally, the coupling can be confirmed by a PLE or spectrum (see Section 4.1). Fine-tuning of the coupling is then done by measuring the collection efficiencies from saturation curves of a single emitter in the waveguide (see Section 4.3).

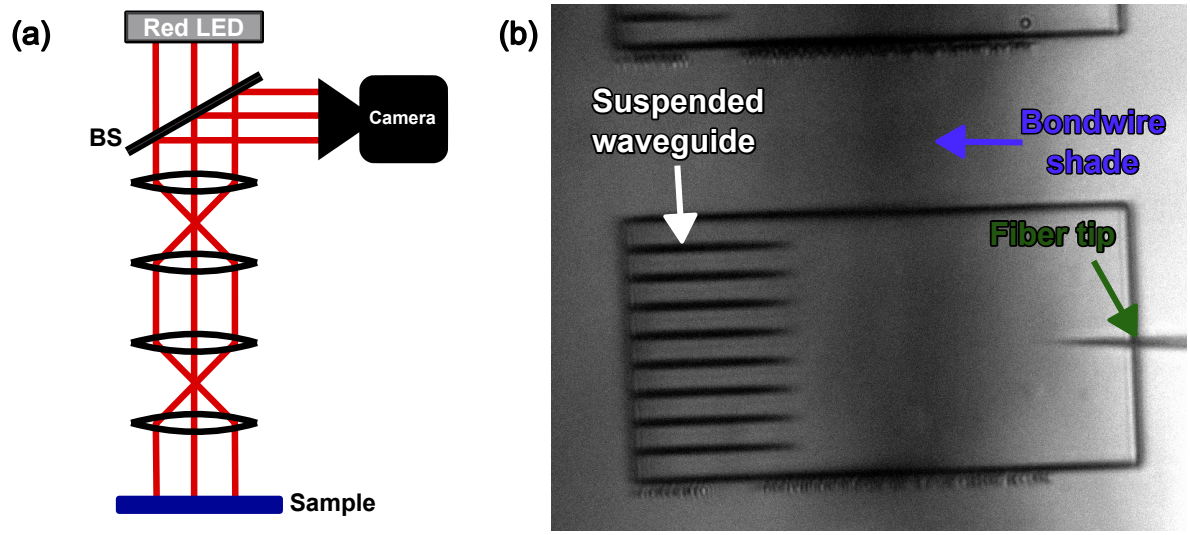

Figure C.1: Optical configuration for sample imaging through a confocal optical path. (a) Schematic of the optical components that are used for the imaging. The double 4f-system contains lenses within the axes of the cryogenic temperature stages. (b) A typical image that is obtained from the reflections of the red LED to the camera. The image is processed to improve contrast in software and updated real-time. The image shows 8 suspended diamond waveguides (left side), the tip of a tapered fiber (right side) and the shadow of the bond wire, which is ~(50-100) µm above the diamond sample.

C.2. Pictures of the setup

This section consists of some images of the setup, which can serve to aid the visualization of certain components in the experimental setup.

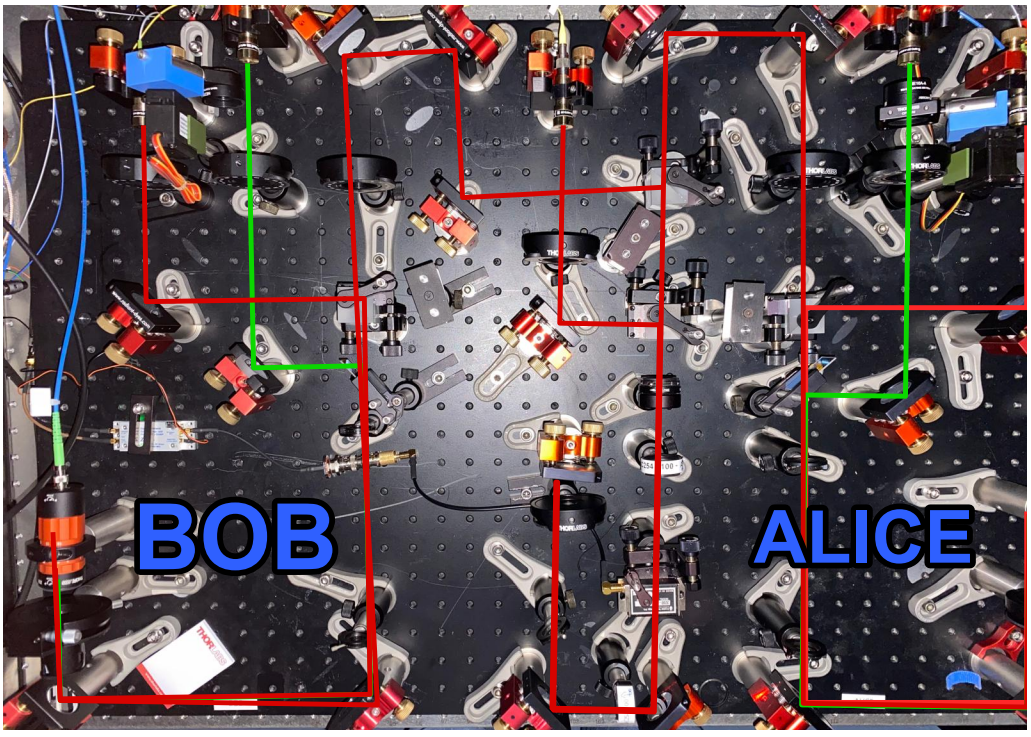

Figure C.2: A picture of the optical table that is used for combining the different paths of the two subsetups, including the way in which the single pulse source is distributed among the two subsetups.

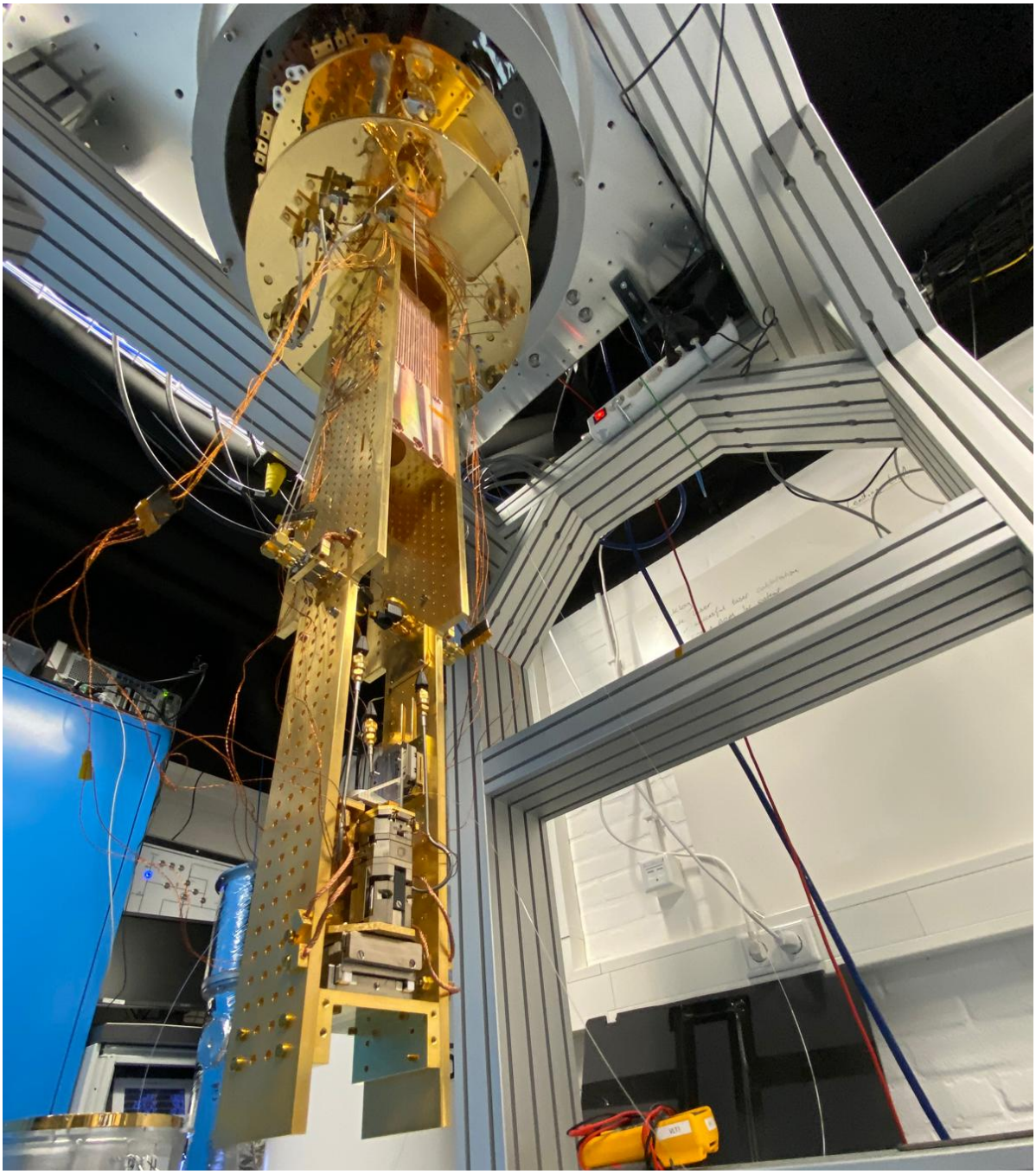

Figure C.3: Image taken from the bottom of the opened cryostat. The image shows (a few of) the cold plates and the long arm that is at the coldest temperature. The bottom of this long arm is where the sample stage is mounted, together with the fiber stacks (out of which only one is visible). The image also shows the frame around the fridge, which is used to stabilize it. Lastly, the wiring for the MW delivery through the bondwire can also be seen.

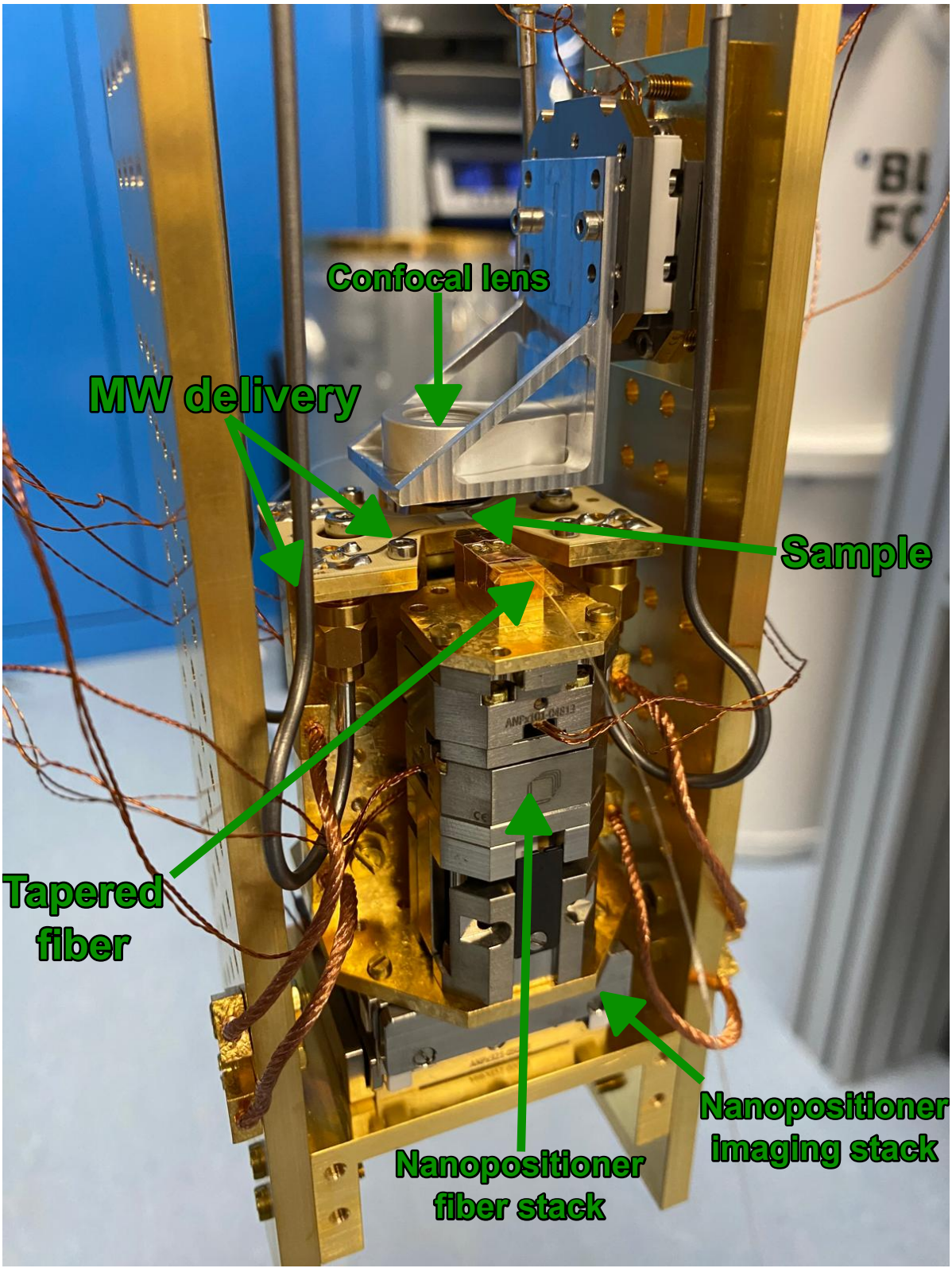

Figure C.4: A close-up image of the mounted sample together with the fiber stack. The image shows the sample on a Printed Circuit Board, above which the final lens of the double 4f-imaging system is suspended. The vertical position of this lens is controlled with the stepper motor the stepper motor on which it is mounted in order to adjust the focus of the image. The 3 stepper motors beneath the fiber mount are responsible for its movement. The image also shows two MW delivery wires, which belong to one of the two bond wires.